ADVISORY COMMITTEE

EDITORIAL BOARD

[1] The Faculty of Civil Engineering, Wrocław University of Technology
Wybrzeże Wyspiańskiego 27, 50-370 Wrocław, Poland
Tel. +48 71 320 41 35, Fax. +48 71 320 41 05, E-mail: jan.kmita@pwr.wroc.pl

[2] The Faculty of Civil Engineering, Wrocław University of Technology
Wybrzeże Wyspiańskiego 27, 50-370 Wrocław, Poland
Tel. +48 71 320 34 04, E-mail: wojciech.glabisz@pwr.wroc.pl

[3] The Faculty of Mechanical Engineering, Wrocław University of Technology
ul. Łukasiewicza 5, 50-371 Wrocław, Poland
Tel. +48 71 320 21 73, Fax. +48 71 320 34 22, E-mail: metalplast@pwr.wroc.pl

POLISH ACADEMY OF SCIENCES – WROCŁAW BRANCH
WROCŁAW UNIVERSITY OF TECHNOLOGY

ARCHIVES OF CIVIL AND MECHANICAL ENGINEERING

Quarterly
Vol. VIII, No. 3

WROCŁAW 2008

EDITOR IN CHIEF

ZBIGNIEW GRONOSTAJSKI

EDITORIAL LAYOUT AND PROOF-READING

WIOLETTA GÓRALCZYK

TYPESETTING

SEBASTIAN ŁAWRUSEWICZ

SECRETARY

WIOLETTA GÓRALCZYK

Publisher: Committee of Civil and Mechanical Engineering
of Polish Academy of Sciences – Wrocław Branch,
Faculty of Civil Engineering and Faculty of Mechanical Engineering
of Wrocław University of Technology

OFICYNA WYDAWNICZA POLITECHNIKI WROCŁAWSKIEJ
Wybrzeże Wyspiańskiego 27, 50-370 Wrocław
http://www.oficyna.pwr.wroc.pl
e-mail: oficwyd@pwr.wroc.pl

ISSN 1644-9665

Drukarnia Oficyny Wydawniczej Politechniki Wrocławskiej. Zam. nr 649/2008.

Contents

Spis treści

ARCHIVES OF CIVIL AND MECHANICAL ENGINEERING

Vol. VIII 2008 No. 3

Modelling of structure changes in TRIP type steel during hot deformation

M. ADAMCZYK, D. KUC, E. HADASIK
Silesian University of Technology, Krasińskiego 8, 40-019 Katowice, Poland

Physical modelling of the changes occurring in the structure of low-alloy C-Mn-Al TRIP-aided steel during hot-rolling were presented in this paper. An influence of deformation and controlled cooling parameters on the microstructure of the tested steel was determined. Metallographic research showed continuous refinement of structure in consecutive stage of deformation. Applied parameters of cooling allowed obtaining multi-phase structure containing ferrite, bainite, and also retained austenite.

Keywords: *TRIP steel, physical modelling, plane strain test*

1. Introduction

A leading trend among vehicle manufacturers is a reduction of the total weight of a car, thereby reducing the emission of exhaust into the natural environment, as well as to enhance passenger safety [1]. Achieving the right material strength-to-density ratio is essential. Therefore, particular attention is paid to, apart from aluminium and magnesium based alloys [2, 3], high-strength steels with multiphase structures, whose production cost is a few times lower [4]. As regards metal sheets applied for car body components, the requirements concerning their mechanical properties reduce to achieving high strength with keeping the required plasticity and press formability [5].

This group of materials includes the modern TRIP steels whose structures, apart from ferritic, bainitic and martensitic phases, contain retained austenite in the amount of 5–20% [4, 6], which undergoes transformation into martensite through cold working. Higher carbon levels are applied for TRIP steels which is due to the necessity to produce a highly enriched austenite with a carbon content above 0.8 mass %. Apart from carbon manganese and silicon play an important role so as to control the transformation behaviour and to stabilize the retained austenite. Silicon does prevent or at least retard carbide precipitation during bainite formation and allows the carbon to diffuse into the retained austenite. [7] As a higher silicon content can be responsible for a poor surface quality of hot rolled steel and a poor coatability of cold rolled steel, a partial or complete substitution of silicon by aluminium has been considered [7, 8]. Aluminium promotes the generation of ferrite and first of all is not soluble in cementite and therefore has to diffuse from the interface of the carbide particle, before the particle can continue to grow. Aluminium addition significantly increases carbon in retained austenite, due to the rise of T_0 temperature where austenite and ferrite have

identical free energies [7]. At a high carbon content, martensite transformation begins in further forming stages or in conditions leading to failure [9]. Therefore, the TRIP steel can have properties required for the car body components designed to absorb high cracking energy [1, 6]. The aim of the paper is to evaluate the structural changes in the low-alloy C-Mn-Al TRIP steel, which occur during hot plastic deformation and to determine optimal conditions of controlled cooling in order to obtain the required fraction of individual phases.

2. Research methodology

The research material used in the study was the C-Mn-Al TRIP steel, cast in laboratory conditions in Vitkovice S.A. Ostrava. Its chemical composition is presented in Table 1.

Table 1. Chemical composition of investigated steel in wgt %

C	Mn	Al	Si	Cr	Ni	Mo	S	P	V	Ti
0.23	1.54	0.80	0.25	0.18	0.09	0.021	0.012	0.015	0.003	0.002

Based on the plate-rolling tests conducted on a rolling line at Institut für Metallformung in Bergakademie Freiberg [10], simulation tests were carried out. They aimed at reconstruction of the phenomena occurring in the steel structure during the hot rolling process. The tests were performed using the Gleeble 3800 system, with applying the hot compression method and using anvils which enable effecting deformations in conditions similar to the plane strain. Using the recorded parameters of the rolling process, two process variants were assumed, differing with the deformation temperatures and the time of intervals between them, according to Table 2 and the diagram in Figure 1.

Table 2. Material deformation parameters during thermomechanical treatment

Deformation	Variant A				Variant B			
	T, °C	$\dot{\varepsilon}$, s^{-1}	ε	t, s	T, °C	$\dot{\varepsilon}$, s^{-1}	ε	t, s
1	1050	25	0.2	–	1070	25	0.2	–
2	1020	35	0.4	12	940	35	0.4	40
3	1000	35	0.3	2	920	35	0.3	2
4	970	65	0.4	1	910	65	0.4	1
5	970	100	0.3	1	910	100	0.3	1

Physical simulation consisted of soaking of the test pieces at a temperature of 1250 °C, their cooling to a deformation temperature corresponding to the pass in the breakdown stand and next, prescribing four successive deformations, which determine the structure and final properties of the material. After the deformation process, controlled cooling of the test pieces was applied with an isothermal soaking at 400 °C, for a bainitic transformation to take place.

By using the dilatometric examination results which take into account the influence of deformation and the variable cooling rates on the temperature of phase transformation, 3 cooling variants were applied, according to Table 3. The first variant consists of continuous cooling of the test pieces after the final deformation until soaking temperature at a rate 15 °C/s. The other variants assume slow cooling of the specimens within the $\gamma \rightarrow \alpha$ transformation range at a rate 8 and 4 °C/s, with subsequent cooling with rate 30 °C/s in order to avoid a pearlitic transformation.

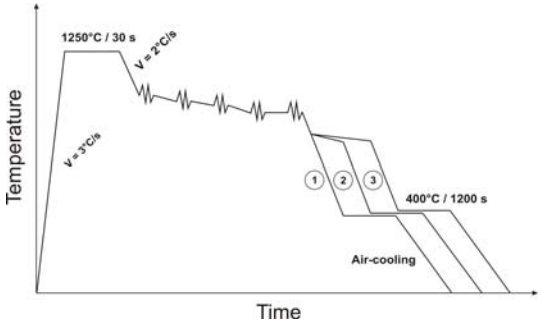

Fig. 1. Simulation diagram and cooling parameters after final deformation for variants A and B

Table 3. Controlled cooling parameters after deformation

Method of cooling	Cooling rate, °C/s	Temperature range, °C	
		Variant A	Variant B
1	15	970 → 400	910 → 400
2	15	970 → 900	910 → 840
	8	900 → 750	840 → 700
	30	750 → 400	700 → 400
3	15	970 → 900	910 → 840
	4	900 → 750	840 → 700
	30	750 → 400	700 → 400

The diversification of cooling parameters enabled an evaluation of the components' fractions in the final structure of the steel. For an evaluation of the retained austenite fraction, an X-ray quantitative analysis was applied. The tests were conducted using a Philips PW 1130 diffractometer by applying a Co lamp, wave length 1.79 Å. Austenite fraction was determined by means of direct comparison of the strongest reflexes, $\alpha(110)$ and $\gamma(111)$.

3. Research results

The test of the pieces' structure before deformation, after soaking for 30 seconds at a temperature of 1250 °C, is presented in Figure 2. The analyzed steel is characterised by an equiaxial coarse-grained structure with the austenite grain size of d_γ = 178 μm (Table 4). After initial deformation carried out with similar parameters for variants A

and B, the material had an inhomogeneous structure. Fine, dynamically recrystalized grains, in a form of little chains, are visible on boundaries of elongated primary grains (Figure 3). The mean grain size at this stage is similar for both variants and amounts to: for variant A: d_γ = 88 μm, and for variant B: d_γ = 90.6 μm.

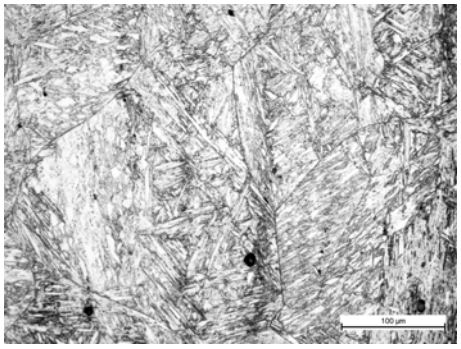

Fig. 2. Structure after soaking for 30 seconds at a temperature of 1250 °C

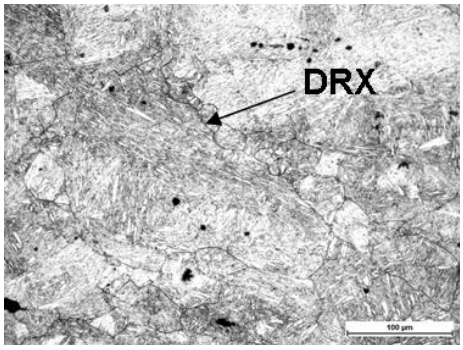

Fig. 3. Structure after initial deformation carried out according to variant A

The temperature of successive deformation and the interval time differed significantly (Table 2), which has a significant influence on the steel structure (Figure 4). After the deformation realized according to variant B, the austenite grain obtained was twice smaller than that in variant A (Table 4). This was a consequence of the application of a lower compression temperature and influence of static recrystalization process in a longer time period between successive deformation, resulted in greater size-reduction of the grain.

Table 4. The austenite grain size and the ferrite fraction after particular stages of deformation

Stage	VARIANT		
	A	B	
	Austenite grain size d_γ [μm]		Ferrite fraction [%]
1250 °C/30s	178		–
Deformation 1	88.0	90.6	–
Deformation 2	31.5	16.8	–
Deformation 3	21.2	–	5.2
Deformation 4	18.9	–	9.8
Deformation 5	15.4	–	16.8

The third deformation for variant A leads to further refinement of the structure (Figure 5a), with the grain size d_γ = 21.2 μm. Fine austenite grains formed as a result of recrystallization are visible in the structure. The successive stages lead to homogenization of the structure (Figure 6); the austenite grain size reduces to d_γ = 18.9 μm. After the last deformation, an equiaxial structure with the mean size of d_γ = 15.4 μm was obtained for this variant.

In the case of variant B, the third deformation was probably conducted already in a two-phase range. On the boundaries of refined austenite grain, the $\gamma \rightarrow \alpha$ transformation's fine products are visible (Figure 5b), whose fraction amounts to 5.2%. A temperature reduction in a successive deformation process leads to an increased ferrite fraction in the structure after quenching (Table 4). The final deformation takes place with a further increase of the α phase fraction (Table 4), present in the form of a network on austenite grain boundaries.

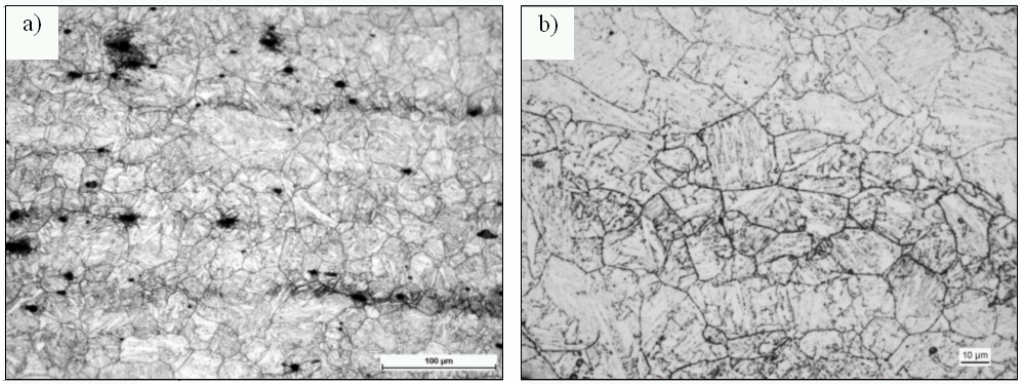

Fig. 4. Example of microstructure after second deformation: a) variant A, b) variant B

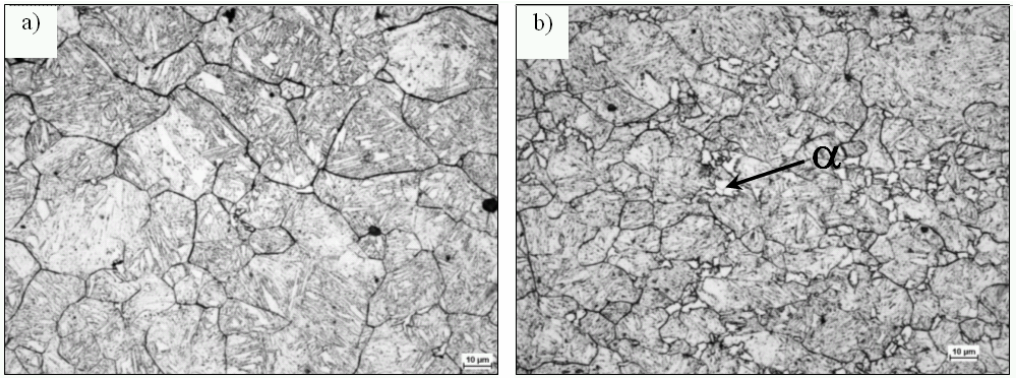

Fig. 5. Example of microstructure after third deformation: a) variant A, b) variant B

After the applied thermomechanical treatment, the material is characterized by a multi-phase structure consisting of ferrite, bainite and retain austenite (Figures 7, 8). By applying the colour etching method, regions with retained austenite have been identified. The retained austenite is located at ferrite-ferrite and ferrite-bainite grain boundaries, as well as between bainite bands (Figure 8). For all of the adopted variants, the mean grain size of retained austenite falls within the range of $d_{\gamma r}$ = 1–2 µm.

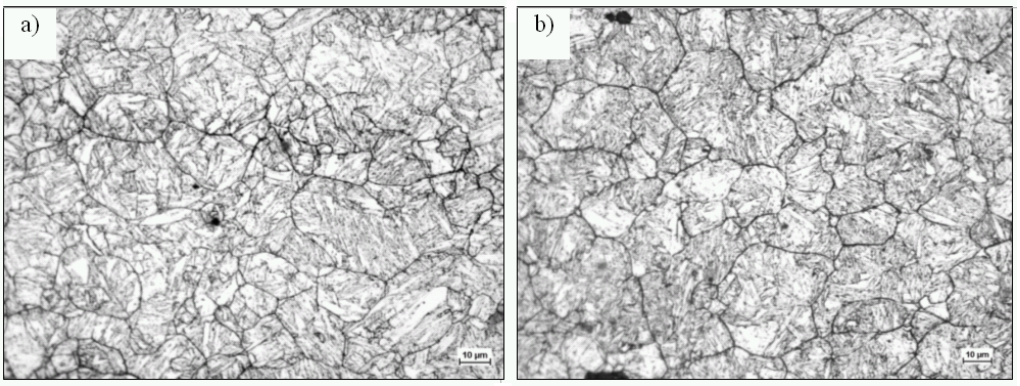

Fig. 6. Example of microstructure after fourth (a) and fifth (b) deformation carried out according to variant A

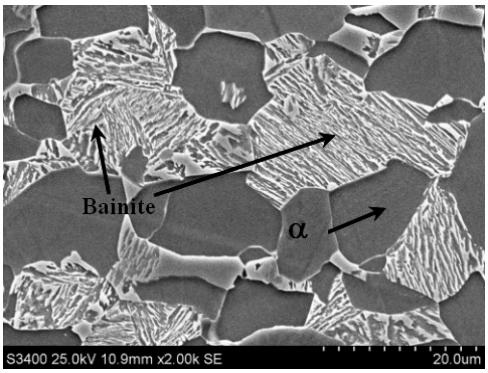

Fig. 7. Example of microstructure after thermomechanical treatment according to B3

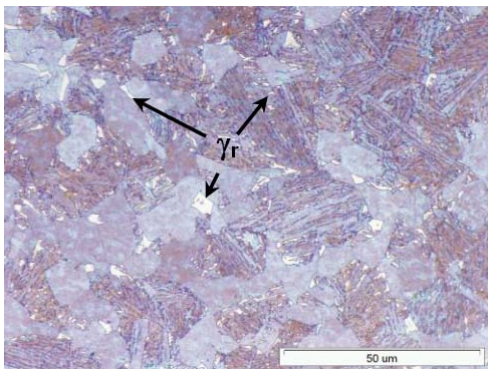

Fig. 8. Example of microstructure after thermomechanical treatment according to B2

The individual simulation variants have a significant influence on the fraction of components present in the steel structure. A deformation process followed by continuous cooling with rate 15 °C/s to a temperature of 400 °C according to variants A1 and B1, leads to obtaining structures with the smallest ferrite fraction. For variant A1, a bainitic structure was obtained, containing ca. 3% of ferrite located on the boundaries of former austenite grain. The application of variant B1, where the final deformation was probably realized in the range of $\gamma + \alpha$ allowed obtaining 25% of that phase in the final structure. The grain size of ferrite is similar and amounts to $d_\alpha = 6.3$ μm for A1 and $d_\gamma = 6.0$ μm for B1.

The other treatment variants, including slower cooling of the steel within the $\gamma \rightarrow \alpha$ transformation, assumed obtaining a larger ferrite fraction in the steel's final structure. A reduction of cooling rate to 8 °C/s within the temperature range of 900–750 °C for variant A2 results in a 16% increase of the α phase fraction. Simultane-

ously, an increase in the ferrite grain size is observed: d_α = 8.2 μm. After application of variant B2, the fraction of this phase in the structure amounts to 35%, with the mean size of the grain d_α = 7.1 μm. The content of retained austenite γ_r, determined by an X-ray analysis, equals 12.2% for variant A2 and 15.2% for B2.

After both variants of thermomechanical treatment, A3 and B3, the material structure is characterized by a banding arrangement of the products of primary austenite transformation (Figure 9a, b). The cooling rate 4 °C/s applied in the allotropic transformation range leads to a further increase of the ferrite fraction in the steel structure as compared to previous variants. The content of phase α makes up 25% of the fraction for variant A3 and 52% for B3, with the mean size of the grain for A3: d_α = 8.5 μm, and for B3: d_α = 8.2 μm.

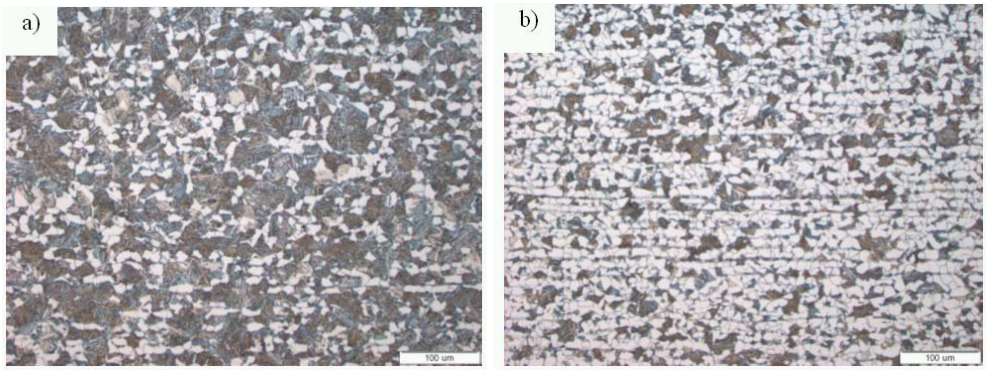

Fig. 9. Example of microstructure after thermomechanical treatment according to: a) A3, b) B3

4. Conclusion

An evaluation of the influence of deformation parameters and controlled cooling on the microstructure of the low-alloy C-Mn-Al TRIP steel has been carried out in the paper. The adopted research variants included finishing deformation of the tested steel in the austenite stability range and in a two-phase range. The analyzed steel after soaking before deformation at 1250 °C has an equiaxial coarse-grained austenitic structure. The assumed parameters of particular deformations and the recrystallization processes allowed obtaining a homogeneous structure with austenite grain size of d_γ = 15.4 μm. The ferrite fraction in the structure after deformation in the $\alpha+\gamma$ range amounts to 17%.

Continuous cooling of the test pieces from the temperature of deformation performed at a rate 15 °C/s before isothermal holding results in obtaining a low content of ferrite. A reduction of cooling rate within the two-phase range has a significant influence on the increase of the fraction of this phase in the final structure. Elongation of the cooling time in this range slightly increases the ferrite grain size. Deformation in

a two-phase range allows obtaining finer grain in α phase, which is probably connected with the location of plastic deformation in soft ferrite, which causes its refining. The stable retained austenite of a mean size within the range $d_{\gamma r}$ = 1–2 μm is located at grain boundaries and in the form of fine regions between bainite bands. The austenite fraction in the final structure of the steel does not exceed ~15 %. As a result of the applied thermomechanical treatment parameters, with subsequent slow cooling rate 4 °C/s in the range $\alpha + \gamma$ a fine-grain structure was obtained with advantageous fractions of the individual phases. The amount of bainite and retained austenite in the obtained structure has a strengthening role, whereas the ferrite fraction should ensure appropriate ductility during further cold forming processes.

References

[1] Cooman B. C., Speer J. G.: *Quench and Partitioning Steel: a New AHSS Concept for Automotive Anti-Intrusion Application*, Steel Research Int. 77, No. 9–10, 2006, pp. 634.
[2] Dobrzański L.A, Tański T., Čížek L.: *Influence of Al addition on microstructure of die casting magnesium alloys*, Journal of Achievements in Materiale and Manufacturing Engineering, 19, 2006, pp. 49–55.
[3] Mehta D.S., Masood S.H., Song W.Q.: *Investigation of wear properties of magnesium and aluminium alloys for automotive applications*, Journal of Materials Processing Technology, No. 155–156, 2004, pp. 1526–1531.
[4] Adamczyk J., Grajcar A.: *Steel sheets of multiphase structure for the automotive industry*, 3rd Scientific Conference On Materials, Mechanical and Manufacturing Engineering. Gliwice-Wisła, 16–19.05.2005.
[5] Turczyn S., Dziedzic M.: *Rolling of car body sheets made from new generation steel*, Hutnik – Wiadomości Hutnicze, No. 4, 2002, pp. 126–131.
[6] Kuziak R.: *Modelling of structure and phase changes proceeding in thermomechanical treatment of steel*, Instytut Metalurgii Żelaza, Gliwice, 2005.
[7] Bleck W., Phiu-on K.: *Effect of microalloying in Multi Phase Steels for Car Body Manufacture*, 14. Sächsische Fachtagung Umformtechnik: Werkstoffe und Komponent für den Fahrzeugbau, Freiberg, 2007, pp. 38–56.
[8] Bellhouse E.M, Mertens A.I.M., McDermid J.R.: *Development of the surface structure of TRIP steels prior to hot-dip galvanizing*, Materials Science and Engineering, A 463, 2007, pp. 147–156.
[9] Grosman F., Kawalla R.: *Modern steels for automotive industry sheets, Przetwórstwo metali – plastyczność a struktura*, Gliwice, 2006.
[10] Kuziak R., Kawalla R., Pietrzyk M., et al.: *Rheological model for simulation of hot rolling of new generation steel strips for automotive applications*, Steel Research Int., 77, 2006, No. 12, pp. 927–933.

Modelowanie zmian struktury stali typu TRIP podczas odkształcenia na gorąco

W pracy dokonano oceny wpływu parametrów odkształcenia oraz kontrolowanego chłodzenia na mikrostrukturę niskostopowej stali C-Mn-Al typu TRIP. Przyjęte parametry poszczególnych odkształceń pozwoliły na uzyskanie jednorodnej struktury o wielkość ziarna austenitu ~15 μm. Obniżenie prędkości chłodzenia w zakresie dwufazowym wpływa istotnie na wzrost udziału tej fazy w strukturze końcowej. Chłodzenie z prędkością 4 °C/s w zakresie $\alpha + \gamma$ pozwoliło na uzyskanie drobnoziarnistej struktury o korzystnym udziale poszczególnych faz. Stabilny austenit szczątkowy o udziale do ~15% zlokalizowany jest na granicach ziarn oraz w postaci drobnych obszarów pomiędzy listwami bainitu. Otrzymana w strukturze ilość bainitu oraz austenitu szczątkowego wpływa umacniająco, natomiast frakcja ferrytu powinna zapewnić odpowiednią ciągliwość podczas dalszego kształtowania na zimno.

ARCHIVES OF CIVIL AND MECHANICAL ENGINEERING

Vol. VIII 2008 No. 3

The influence of thermo-mechanical treatment on the structure and plasticity of FeAl intermetallic phase–base alloy

E. BERNSTOCK-KOPACZYŃSKA, I. BEDNARCZYK, M. JABŁOŃSKA,
G. NIEWIELSKI, D. KUC
Silesian University of Technology, Krasińskiego 8, 40-019 Katowice, Poland

Alloys based on intermetallic phases from the Fe-Al system they belong to a group of high-temperature creep resisting materials of advantageous physicochemical and mechanical properties at an elevated and high temperature. In general, limitation on the capacity for a broad application of intermetals from the Fe-Al system, e.g. as an alternative to expensive alloy steels of specific properties, is their insufficient plasticity, which is a factor inhibiting further their development as constructional materials. Under this study, research has been conducted on the capacity for forming alloys based on intermetallic phases from the Fe-Al system, via thermo-mechanical processing. In the present work, the possibility of forming Fe-Al-intermetallic-phase-based alloys in thermo-mechanical treatment (TMT) has been studied. After casting and annealing, alloy specimens were subjected to axial-symmetric compression in the Gleeble 3800 simulator in the range of 700–1200 °C at 0.01, 0.1, 1.0, 10 s^{-1} strain rates. In order to analyze the processes which take place during deformation, the specimens after deformation were intensely cooled with water. Structural examination was carried out using light and electron microscopy. The impact of hot rolling process parameters on the structure of intermetallic-phase-based FeAl alloys and properties has been determined. The results will constitute the basis for modelling the structural changes in FeAl intermetallic alloy.

Keywords: *FeAl alloys, intermetallic, test compression, thermal plastic deformation, dynamic recrystallization*

1. Introduction

Alloys based on intermetallic phases from the Fe-Al system are emerging as materials for high temperature structural applications. They promise to bridge the gap between the structural ceramics and nickel-based Superalloys operating in high temperature range [1–3]. Fe-Al alloys‘ properties, such as: low density, high melting temperature, high strength and good oxidizing resistance, coupled with good crack resistance, create wide prospects for their industrial applications, for components of machines working at a high temperature and corrosive environment [4–5]. The major problem restricting their universal application is their low plasticity and their brittle cracking susceptibility, which leads to obstacles their development as construction materials. Consequently, the research of intermetallic phase based alloys focuses on their plasticity is required [6–10].

This paper analyses the changes in microstructure of an ordered FeAl alloy with 38% at. content of aluminium with additional of Zr, B and C. Material after casting and annealing was subjected high-temperature deformation in the range of tempera-

tures from 700 °C to 1200 °C. The results will constitute the basis for modelling the structural changes in FeAl intermetallic alloy and development base of the forming technology of the structure and properties of Fe-Al intermetallic via thermo-mechanical processing.

2. Research methodology

2.1. Material

Material for the research consisted of bars cast from an alloy based on FeAl intermetallic phase of a chemical composition shown in Table. The alloy was prepared by casting into graphite moulds. The following contents were used for smelting: ARMCO iron, aluminium 99.98% wt. minimum, amorphous boron and technically pure molybdenum powder compact. Ingots were obtained in the form of cylinders of dimensions: ø 14 mm and 120 mm in length. Subsequently, the material was subjected to homogenizing annealing at the temperature of 1000 °C for 48 h and cooled with furnace.

Table. The chemical composition of the investigated alloy (%at., %wt.)

	Al	Mo	Zr	C	B	Fe
% at.	38.00	0.20	0.05	0.10	0.01	61.64
% wt.	22.82	0.43	0.10	0.03	0.002	76.62

2.2. Plastometric compression test

After the process of thermal treatment, specimens were made from the material, next they were subjected to an axial-symmetric compression test in the Gleeble 3800 simulator with simultaneously freezing the structure after deformation by quick cooling with water. Compression tests were conducted in the range of temperatures from 700 °C to 1200 °C at strain rates: 0.01 s^{-1}, 0.1 s^{-1}, 1.0 s^{-1}, 10 s^{-1}, until the true strain values reached circa $\varepsilon = 1.0$. The compression trials results, such as the sample temperatures T [°C], stresses σ [MPa], forces [N] and strains ε, processed with the calculation sheet, provided the means for determining the flow curves in the stress σ – strain ε system. After an axial-symmetric compression test, an analysis was made of the microstructure on a section parallel to the specimen's axis, with the use of light microscopy.

2.3. Hot rolling

Cast specimens, 20 mm in height and 40 mm in width, were used as an initial material for the hot rolling process. The process was conducted at the Institute of Modelling and Control of Forming Processes in the Czech Republic on the K 350 quarto

rolling mill used for hot rolling of flat products. The process was conducted in the following stages:

- preliminary rolling at a temperature of 1200–1100 °C with the use of ferritic steel spacers separating cold rollers from the rolled material, with a 20% draft in each pass;
- rolling at a temperature of 1100–1000 °C in a ferritic steel shield separating cold rollers from the rolled material, with a 20% draft in each pass;
- finishing rolling was conducted at a temperature of 1000 °C, with applying 25% reverse drafts and interoperation annealing;
- finishing rolling, forming the microstructure at a temperature of 900 °C, with applying 25% reverse drafts and interoperational annealing and cooling in oil after the last pass;
- annealing for 30 minutes at 800 °C.

The calculated average strain rate during rolling amounted to 10 s^{-1}.

3. Result

Microstructure of Fe38Al alloy after casting was presented in Figure 1. In the tested material microstructure, the grains of variable dimensions with characteristic residues of dendritic structure were observed.

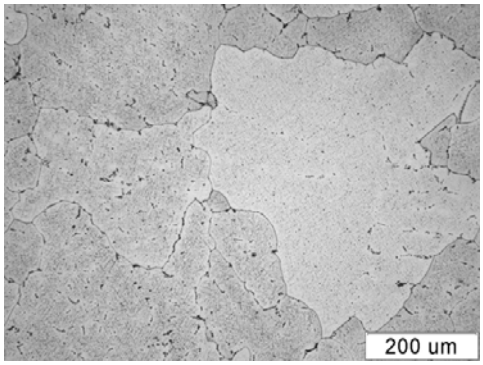

Fig. 1. Microstructure of the Fe38Al alloy after casting

The axi-symmetric hot compression tests made for Fe38Al alloys made it possible to determine the deformability characteristics in the form of flow curves in the stress-strain system (Figures 2, 3). The stress-strain curves represent a broad range of strain consolidation. The flow curves' courses differ, depending on the process temperature. The stress-strain curves represent a broad range of strain consolidation. The flow curves' courses differ, depending on the process temperature. In the temperature range from 1000 °C to 1200 °C, quick material hardening is observed. The alloy reaches the maximum yield stress – σ_p on the flow curve, with a low strain value – ε_p on the flow curve, after which the material hardening and softening processes counterbalance each other.

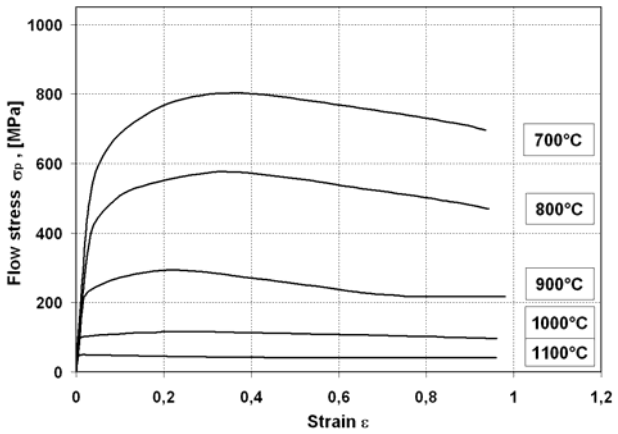

Fig. 2. Stress strain curves for Fe38Al alloy deformed at temperature 700–1100 °C with a rate 0.1 s^{-1}

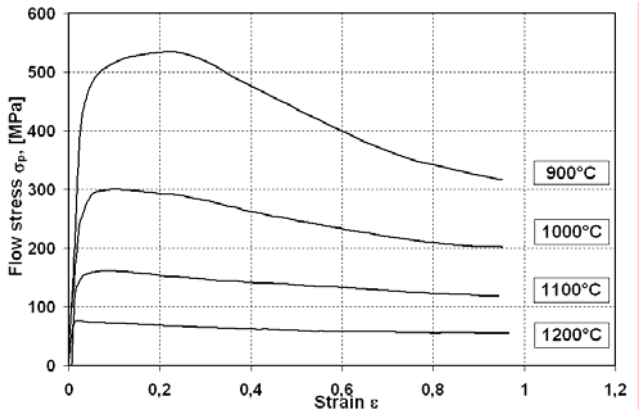

Fig. 3. Stress strain curves for Fe38Al alloy deformed at temperature 900–1200 °C with a rate 10 s^{-1}

After deformation with a rate 0.1 s^{-1}, initiation the dynamic recrystallization process was observed at a temperature of 800 °C. Initial stages of dynamic recrystallization are visible in the microstructure, which is shown by the formation of fine grain chains on primary grain boundaries. At 900 °C, a more advanced processes was observed, which is reflected by almost complete recrystallization of the structure (Figure 4). After deformation at a temperature of 1000 °C, existed the finitial stages of the dynamic recrystallization. Primary boundaries gradually disappear and the recrystallized grain grows. At deformation temperatures of 1100 °C (Figure 5) and 1200 °C, a completely recrystallized structure and the new grain growth become visible.

The same mechanisms of the rebuilding the structure was observed after deformation with a rate 10 s^{-1} but the initial recrystallization process was noticeable at a temperature of 900 °C (Figures 6, 7).

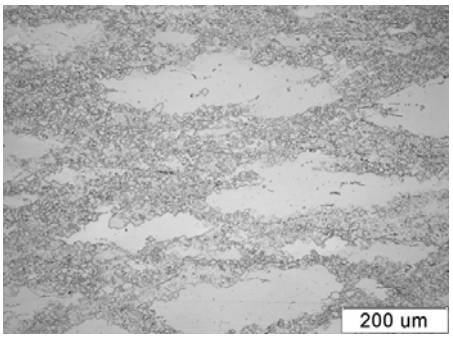

Fig. 4. Microstructure of the Fe38Al alloy after compression at 900 °C with a rate 0.1 s^{-1}

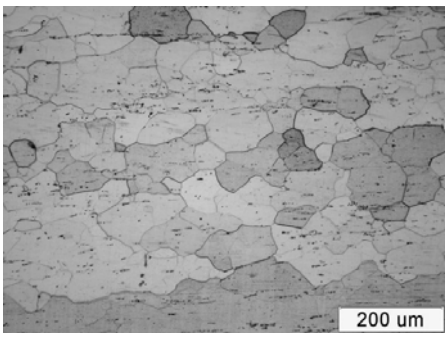

Fig. 5. Microstructure of the Fe38Al alloy after compression at 1100 °C with a rate 0.1 s^{-1}

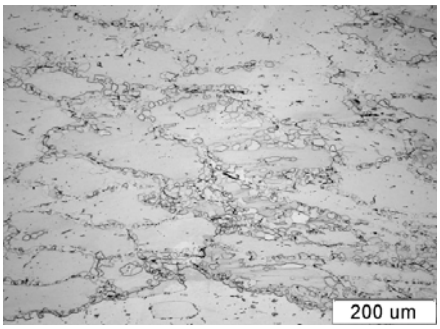

Fig. 6. Microstructure of the Fe38Al alloy after compression at 900 °C with a rate 10 s^{-1}

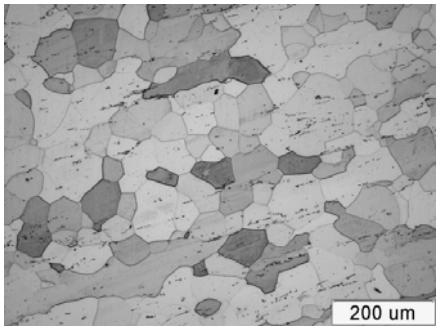

Fig. 7. Microstructure of the Fe38Al alloy after compression at 1100 °C with a rate 10 s^{-1}

Based on the structural studies carried out, the processes taking place in the orderly alloys' structure during high-temperature deformation were detected. The determination of the technological plasticity as well as structural studies enabled selecting the optimal rolling conditions. Rolling on the quarto rolling mill proceeded in several stages. The studied alloy was subjected to the first stage of rolling, during which ferritic steel spacers were used. The application of the spacers was indispensable since first trials demonstrated a grid of cracks on the surface, even in the case of minor deformations (Figure 8).

The spacers separated cold rollers from the alloys' surface. The first stage in a temperature range of 1200–1000 °C, with applying two reverse drafts, enabled reducing the height by 50% (10 mm) 10 s^{-1}. At this stage of rolling, no cracks were identified on the external surface of the sheet. Further deformation was performed using a complete shield made of ferritic steel sheets. The application of a lower process temperature (1100–1000 °C) caused material cracking on its lateral surfaces, while longitudinal surfaces, protected by the shield, were free of any defects. The strips rolled at 1100–1000 °C with a 50% total draft (5 mm sheet) are shown in Figure 9.

Fig. 8. A grid of cracks on the surface of hot rolled alloy at a temperature of 1200–1100 °C at alloy without spacers

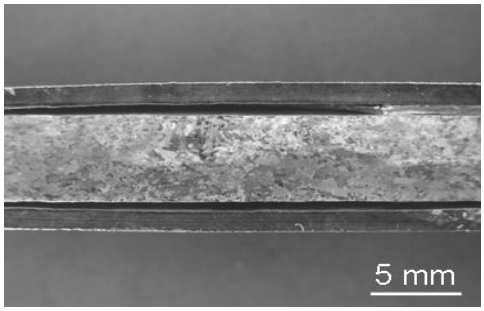

Fig. 9. Cross section of the flat with Fe38Al alloy after rolling with ferritic steel shield at temperature 1100–1000 °C

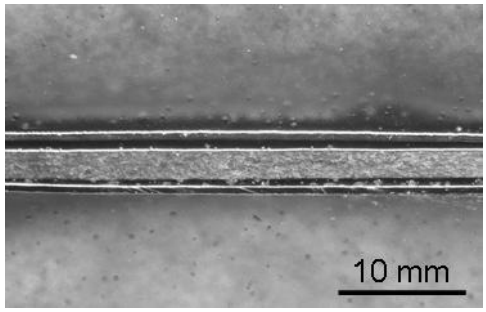

Fig. 10. Cross section of the flat with Fe38Al alloy after rolling with ferritic steel shield at temperature 1100–1000 °C

The effect of this stage of rolling for the studied alloy was microstructural changes in the form of grain size reduction caused by the recrystallization process. Next deformation was performed at a temperature of 1000 °C, with reducing the height to 2.5 mm. A flat bar of the Fe38Al alloy was subjected to further deformation at a temperature of 1000 °C to a thickness of 2 mm. Consequently, a further grain size reduction was obtained. The finishing rolling of the alloy with a 38% Al content, forming the microstructure, was conducted at a temperature of 900 °C using 25% reverse drafts and interoperation annealing. The obtained final sheets (Figure 10), 1 mm in thickness, had no cracks and were characterized by a fine-grain structure.

4. Conclusion

The investigated alloy, Fe-38Al, based on an ordered solid solution, after homogenization annealing has a coarse-grain single-phase structure. A started of recrystallization process takes place at a temperature of 800 °C. In alloy specimens deformed at 900 °C and higher temperatures, after exceeding strain ε_p, the stress be-

comes steady at σ_s. After deformation at 1100 and 1200 °C, the structure is completely recrystallized and the effect new grain growth becomes visible.

The tests have shown that it is possible to form the alloys through thermoplastic processing only where ferritic steel shields of appropriate thickness are applied. Rolling of the alloys without shields led to the occurrence of a grid of cracks. An alloy with a lower aluminium concentration can be plastically formed at a temperature of up to 900 °C, which has been also confirmed in plastometric studies conducted in the form of hot compression tests. Thus, there seems to be a capacity for improvement of the studied alloy's properties by means of thermoplastic treatment. The obtained 1 mm thick sheets can be used as constructional elements working in complex stress fields, at a high temperature and corrosive environments.

References

[1] Stoloff N.S.: *Iron aluminides: present status and future*, Materials Science and Engineering, A 258, 1998, pp. 1–14.
[2] Kuc D., Niewielski G., Jabłońska M., Bednarczyk I.: *Deformability and Recrystallization of Fe-Al intermetallic phase – base alloy*, Journal of Achievements in Materials and Manufacturing Engineering, 17, 2006, pp. 107–110.
[3] Pike L.M.C., Liu. T.: *The effect of vacancies on the environmental yield strength dependence of boron-free and boron-doped Fe-40Al*, Intermetallics, 8, 2000, pp. 1413–1416.
[4] Baligidad R.G., Radhakrishna A.: *Effect of hot rolling and heat treatment on structure and properties of high carbon Fe-Al alloys*, Materiale Science and Engineering, A 308, 2001, pp. 136–142.
[5] Jabłońska M., Rodak K., Niewielski G.: *Analysis of the structure of the intermetallic FeAl40 after hot deformation*, Inżynieria Materiałowa, No. 3, 2004, pp. 145–148.
[6] Niewielski G.,Jabłońska M,: *Characteristics and applications of the intermetallics on the Fe-Al base*, No. 2, 2007, pp. 43–46.
[7] Bystrzycki J, Varin R.A, Bojar. Z : *Recent advances in researches on alloys on the ordered intermetallic phases with alumninium content*, Inżynieria Materiałowa, No. 5, 1996, pp. 137–148.
[8] Szkiniarz W., Hadasik E., Mikuszewski T: *Microstructure and properties formed by hot rolling of FeAl based alloy*, Inżynieria Materiałowa, No. 6, 2004, pp. 844–848.
[9] Yamaguchi H., Ito K.: *High-temperature structural intermetallics*, Acta Materialia, 48, 2000, pp. 307–322.
[10] Jabłońska M., Bernstock E., Jasik A.: *Microstructure and mechanical properties of intermetallics on the base of Fe-Al alloy obtained by casting*, Archives of Materials Science and Engineering, Vol. 28, 2007, pp. 625–628.

Wpływ obróbki cieplno – plastycznej na strukturę i plastyczność stopów na osnowie faz międzymetalicznych

W pracy oceniono możliwość kształtowania struktury i właściwości stopu na osnowie fazy międzymetaliczej z układu Fe-Al na drodze obróbki cieplno-plastycznej. Analizowano wpływ

parametrów odkształcania na strukturę i technologiczną plastyczność stopu Fe-38 % at. Al. Przeprowadzono próbę osiowosymetrycznego ściskania na symulatorze Gleeble 3800, dla zróżnicowanych parametrów odkształcania w zakresie temperatury 700–1200 °C z prędkością odkształcenia $\dot{\varepsilon} = 0.1;\ 10\ s^{-1}$. Na podstawie analizy procesu ściskania próbki walcowano na walcarce kwarto i badano strukturę stopu po kolejnych etapach przetwarzania. Uzyskane wyniki badań będą stanowiły podstawę do opracowania technologii obróbki cieplno-plastycznej intermetalików z układu Fe-Al.

ARCHIVES OF CIVIL AND MECHANICAL ENGINEERING

Vol. VIII 2008 No. 3

Damage in the complex low-cycle fatigue

M. BOBYR, B. YAKHNO
National Technical University of Ukraine "Kiev Polytechnic Institute", Institute of Mechanical Engineering, Peremogi Ave 37, Kiev 03056, Ukraine

E. RUSINSKI, P. HARNATKIEWICZ
Wroclaw University of Technology, Faculty of Mechanical Engineering, Łukasiewicza 7/9, Wroclaw 50-371, Poland

A life prediction approach for a random multiaxial fatigue is proposed in the present paper. D16T aluminium alloy were tested under non-proportional loading (tension-compression, torsion). Cylindrical specimens were tested under different stress controlled trajectories in the plastic range. In additional, numerical method analysis such as finite method – FEM were used in the experiment. The additional damage energy for Al alloy D16T in the middle stabilized (average) cycle during low cycle fatigue for complex non-proportional loading square trajectory was also discussed in relation with fatigue life prediction.

The aim of this paper is to examine the non-proportional low cycle fatigue life of D16T aluminium alloy which shows small additional damage stress, and also develop energetically damage model for complex non-proportional stress state during low-cycle fatigue for construction.

Keywords: *damage, non- proportional low-cycle fatigue, aluminium alloy*

1. Introduction

Engineering components and structures in service are generally subjected to multiaxial fatigue loads. The machine parts are loaded with a combination of different variable forces and moment which often causes a state of multiaxial stress in the fatigue critical areas of the parts. In the most cases a non-proportional cycling multiaxial state of stress occurs. Fatigue life time evaluation of mechanical components under complex multiaxial fatigue condition is of great importance to optimize structural design, and improve inspection and maintenance procedures.

In the design of advance metallic structures plastic deformation is allowed to take place in the region of high stress concentration.

This is done to reduce weight/material and to archive an economical structure – component.

2. Damage in low cycle fatigue

Micro crack initiation, arising and growing take place during elasto-plastic deformation [1–3]. It is popular to accept damage definition as a continual processes com-

bination at submicro-, micro- and macro scale in material structure, which are course of material mechanical property degradation.

The value of damage variable can be written in the next form [1, 2, 7, 8]

$$D = \frac{F - \widetilde{F}}{F} \text{ or } D = 1 - \left(\frac{\widetilde{E}}{E} \right)^k, \tag{1}$$

where:

F – virgin (undamaged) cross-section area,

$\widetilde{F}$ – damaged cross-section area,

E – modulus of elasticity in tension (shear) for virgin (undamaged) material,

$\widetilde{E}$ – modulus of elasticity in tension (shear) for damaged material,

$k = 0.5$ – for materials with big plasticity,

$k = 1$ – for materials with small plasticity.

Damage variable take value in the range $0 \le D \le D_R$, where D_R – is a characteristic of material ($D_R \to 1$). When $D = D_R$ macro crack initiation take place. In reality critical damage variable value $D_R \ne 1$ and it on depends from material plasticity and loading case.

According to J. Fridman theory there are two mechanisms of material destruction: tensile and slice [3]. In each case damage takes place [4, 5] (Figure1).

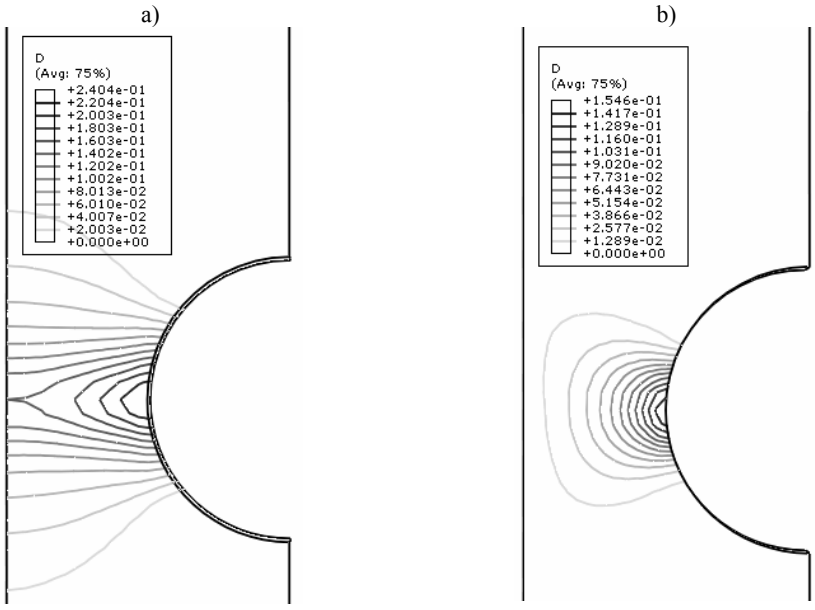

Fig. 1. Distribution of D near stress concentrator for D16T alloy: a – pure tension, b – pure torsion

The tress-strain diagram can be described in three ways: traditional, true and effective (Figure. 2). Definition of effective stress in material $\tilde{\sigma}$ is determined as follows [1, 2, 6]:

$$\tilde{\sigma} = \frac{\sigma^*}{1-D} \tag{2}$$

where:

σ^* – true stress-strain diagram.

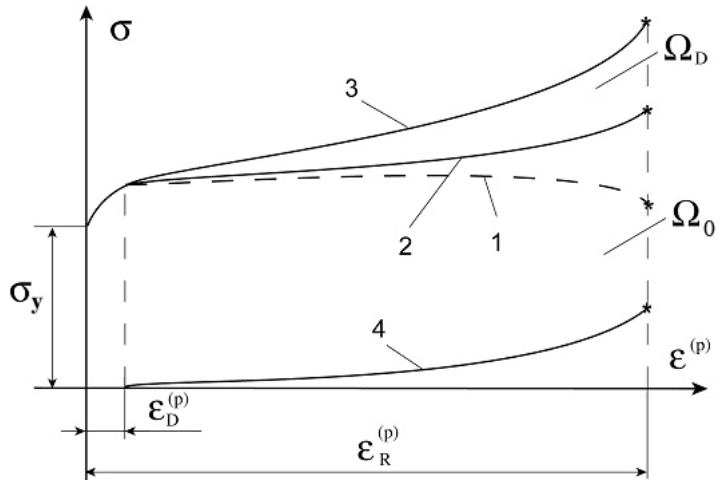

Fig. 2. Stress – strain diagram: σ_y – yield limit stress, 1 – $\sigma = \frac{P}{F_0}$ – usual stress – strain diagram (F_0 – cross-section area in the initial moment of time), 2 – $\sigma^* = \frac{P}{F_i}$ – true stress – strain diagram (F_i – cross-section area in the current moment of time), 3 – $\tilde{\sigma} = \frac{\sigma^*}{1-D}$ – effective stress – strain diagram

The damage take place from some plastic strain $\varepsilon_D^{(p)}$. In first approximation possible to suppose that $\varepsilon_D^{(p)} = 0$, then calculation mistake enlarge safety factor.

In the generalized case thermodynamical potential take the next form [1, 6]:

$$d\Omega = -SdT - \sigma d\varepsilon, \tag{3}$$

where:

Ω – full energy,

T – temperature,
S – entropy.

In isothermal process thermodynamical potential can be written as follows:

$$\Omega = \sigma \cdot \varepsilon \tag{4}$$

In this case full material energy is equal to mechanical energy. Actually it is a square under stress-strain diagram.

Mechanical energy can be shown as a sum of two factors [1, 2, 7, 8]:

$$\Omega = \Omega_0 + \Omega_D\,, \tag{5}$$

where:

$\Omega_0 = \sigma_{true} \cdot \varepsilon^{(p)}$; $\Omega_D = \left(\sigma_{ef} - \sigma_{true}\right) \cdot \varepsilon^{(p)}$; $\varepsilon^{(p)}$ – plastic strain (Figure 2).

Additional damage stress σ_x (curve 4, Figure 2), which is result of micro defects initiation, spreading and arising, in cases of tension and slice can be written in the next form:

$$\sigma_x = \widetilde{\sigma} - \sigma^* = \sigma^*(\varepsilon^{(p)}) \frac{D_\sigma(\varepsilon^{(p)})}{1 - D_\sigma(\varepsilon^{(p)})}, \tag{6}$$

$$\tau_x = \widetilde{\tau} - \tau^* = \tau^*(\gamma^{(p)}) \frac{D_\tau(\gamma^{(p)})}{1 - D_\tau(\gamma^{(p)})}. \tag{7}$$

where:

D_σ – damage variable in the tension (compression) case,
D_τ – damage variable in the case of torsion,
$\varepsilon^{(p)}$, $\gamma^{(p)}$ – plastic deformation in the case of tension and torsion.

This additional damage stresses do job on the track of plastic deformation. This job is equal to additional damage stress energy Ω_D and can be written in the next form (Figure 3a,b):

$$\Omega_D^{(\sigma)} = \int_{\varepsilon_D^{(p)}}^{\varepsilon_R^{(p)}} \sigma^*\left(\varepsilon^{(p)}\right) \cdot \frac{D_\sigma(\varepsilon^{(p)})}{1 - D_\sigma(\varepsilon^{(p)})} d\varepsilon^{(p)}, \tag{8}$$

$$\Omega_D^{(\tau)} = \int_{\gamma_D^{(p)}}^{\gamma_R^{(p)}} \tau^*\left(\gamma^{(p)}\right) \cdot \frac{D_\tau(\gamma^{(p)})}{1 - D_\tau(\gamma^{(p)})} d\gamma^{(p)}. \tag{9}$$

During complex stress-strain state additional damage stress energy can be written as follows [7] (Figure 3c)

$$\Omega_D = \Omega_D^{(\sigma)} + \Omega_D^{(\tau)} \text{ or } \Omega_D = \int_0^{\varepsilon_i^{(p)}} \sigma_{xi} d\varepsilon_i^{(p)}, \tag{10}$$

where $\sigma_{xi} = \sigma_x + \sqrt{3\tau_x}$ and $\varepsilon_i^{(p)} = \varepsilon^{(p)} + \gamma^{(p)}/3$.

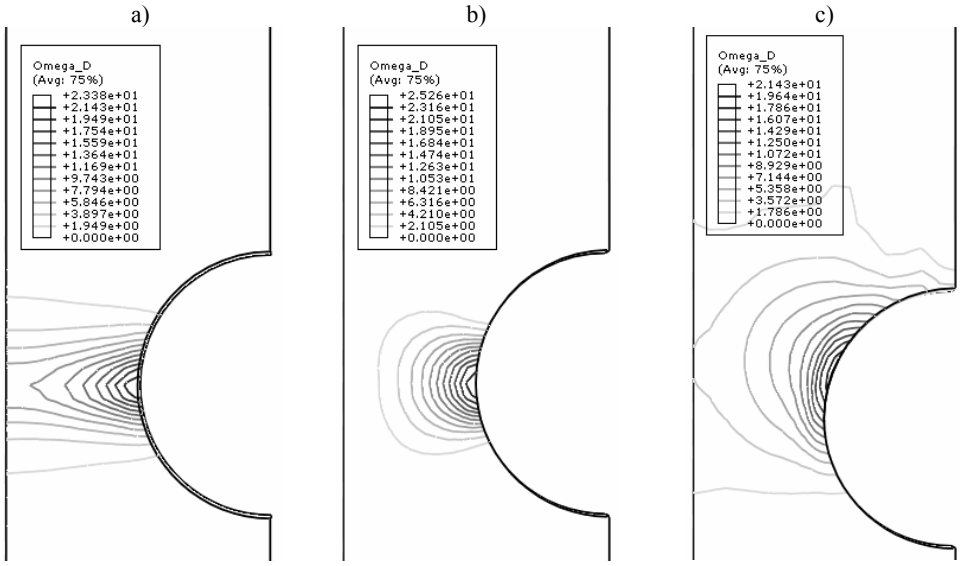

Fig. 3. Distribution of the Ω_D energy near stress concentrator for D16T alloy:
a – pure tension, b – pure torsion, c – complex loading state

In the loading cycle during complex low-cycle fatigue total additional damage stress energy is:

$$\Omega_D^{cycle} = \int_{\delta_\sigma^{(+)}} \sigma_x^{(+)} d\varepsilon + \int_{\delta_\sigma^{(-)}} \sigma_x^{(-)} d\varepsilon + \int_{\delta_\tau^{(+)}} \tau_x d\gamma + \int_{\delta_\tau^{(-)}} \tau_x d\gamma, \tag{11}$$

where:

$\delta_\sigma^{(+)}$ – plastic hysteresis loop width in tension half-cycle,

$\delta_\sigma^{(-)}$ – plastic hysteresis loop width in compression half-cycle,

$\delta_\tau^{(+)}$ and $\delta_\tau^{(-)}$ – plastic hysteresis loop width in the different directions torsion.

After N cycle additional damage stress energy is (Figure 4)

$$\Omega_D{}^{(\Sigma)} = \int_0^N \Omega_D^{\text{cycle}} dN. \tag{12}$$

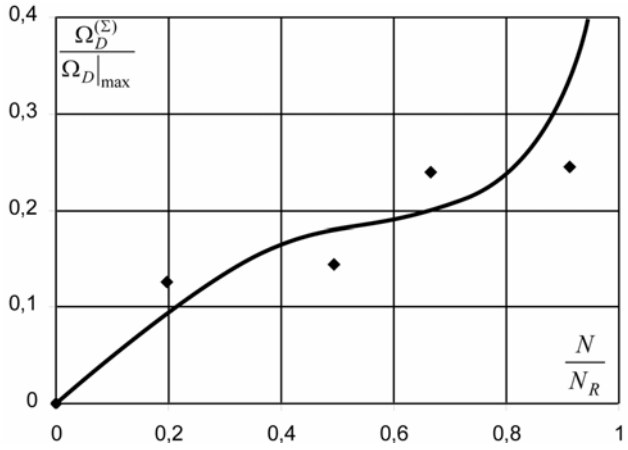

Fig. 4. Kinetic of additional damage stress energy Ω_D in low cycle fatigue: $\Omega_D\big|_{\max}$ – maximum value of Ω_D, N_R – number of cycle for destruction

When destruction takes place ($N = N_R$) the next equation can be applied

$$\Omega_D^{(N_R)} = N_R \cdot \Omega *_D^{\text{cycle}} \tag{13}$$

where:

$\Omega *_D^{\text{cycle}}$ – value of Ω_D^{cycle} in the stabilized (average) loading cycle.

For life prediction calculation It is useful to observe energy $\Omega *_D^{\text{cycle}}$ in the middle stabilized loading cycle. This value for D16T allow is shown on Figure 5.

The specific job of material destruction has to be constant and independent of stress-strain state, then criterion of macro crack initiation during quasistatic, low-cycle destruction was offered in the next form:

$$\frac{\Omega_D\big|_{\max}}{\Omega *_D{}^{cycle} N_R} = M, \tag{14}$$

where for proportional low-cycle loading $M \approx 1$.

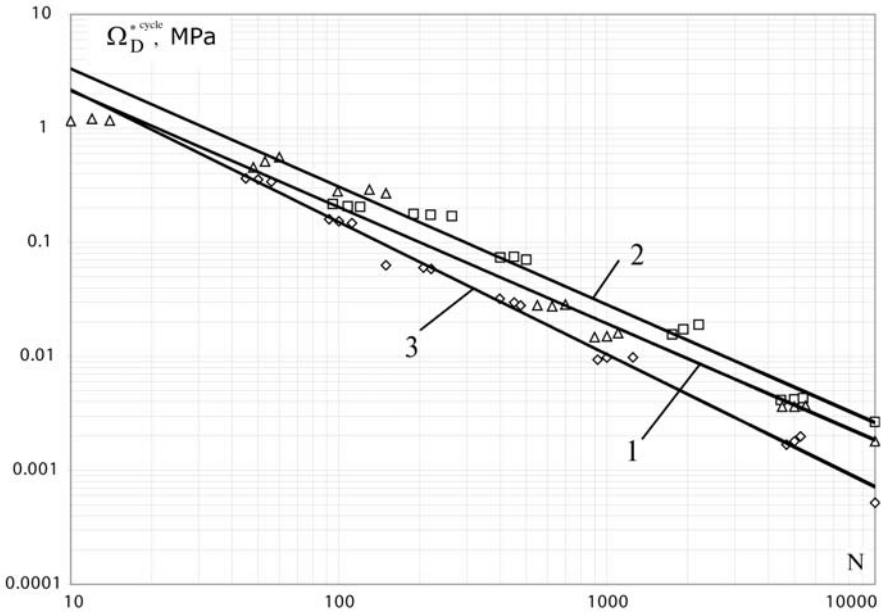

Fig. 5. Additional damage energy for aluminum alloy D16T in the middle stabilized (average) cycle during low cycle fatigue: 1 – tension-compression, 2 – torsion, 3 – complex non-proportional loading square trajectory

For non-proportional low-cycle loading

$$M = \left(\frac{\sigma_в}{\sigma_{i\ a}} \right)^{n\chi}, \tag{15}$$

where:

n – material constant,

χ – constant of the loading path ($0 \le \chi \le 1$, Table),

σ_B – breaking point stress,

σ_{ia} – intensity of the stress amplitude.

Parameter χ can be described in the next form:

$$\chi = \left(\frac{\sigma_{i\min}}{\sigma_{i\max}} \right) \Bigg|_{\text{cycle}}. \tag{16}$$

During investigation the comparison of theoretical and experimental data take place and It is results are shown on the Figure 6.

Table. Value χ in depends on the loading path

$\chi = 0$	$\chi = 0.5$
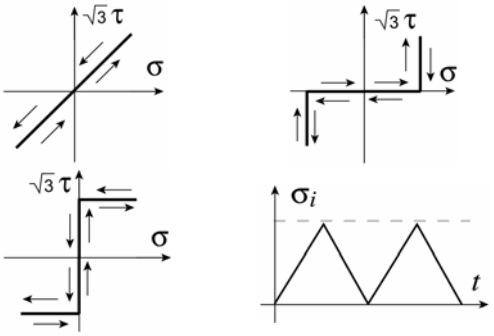	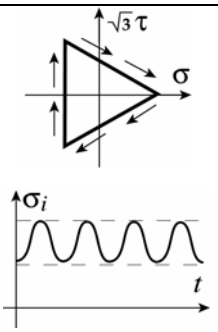
$\chi = 0.7$	$\chi = 1$
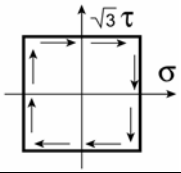	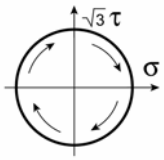
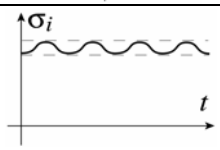	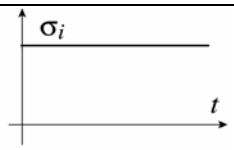

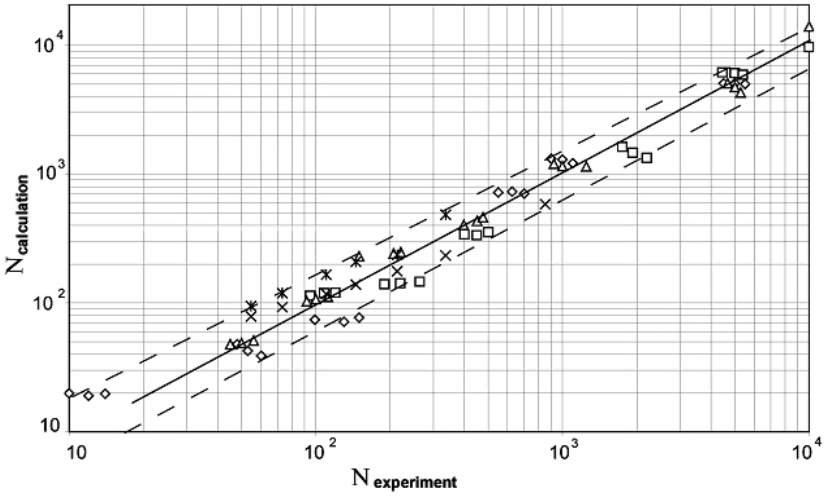

Fig. 6. Experimental and theoretical data comparison: D16T – ◇ – tension-compression, □ – torsion, △ – complex non-proportional loading by square trajectory; steel 45 – × – tension-compression, 1X13 – ✱ – tension-compression

3. Conclusion

Generalized phenomenological damage model for complex non-proportional stress state during low-cycle fatigue for construction materials has been developed. The model use energy of additional damage stress, which is caused by arising and growing of microdefects. Energical criterium of rupture, on the macrocrack initiation stage, take in to account case of loading path and let to evaluate material durability during complex non-proportional low-cycle loading.

The predictive capability of the presented models has been verified by a wide range of experimental results.

References

[1] Lemetr J.: *A Course on Damage Mechanics*, Springer Verlag, Germany, 1992. pp. 210.
[2] Kachanov L.M.: *Basis of Rupture Mechanic*, Moscow, Nauka, 1974, pp. 312.
[3] Troschenko V.T., Lebedev A.A., Strizalo V.A.: *Mechanical Behavior of Materials During Different Loading Cases*, Kiev., Naukova Dumka, 2000, pp. 316.
[4] Borodii M.V., Strizhalo V.A.: *Hardening and Lifetime Prediction Under Biaxial Low Cycle Fatigue*, Proceedings 7 ICBMFF, 2004, pp. 279–284.
[5] Chizik A.A., Petrenja U.K.: *Creep Damage and Micro Destruction Mechanisms*, USSR academy of since reports, Vol. 297, No. 6, 1987, pp. 1331–1333.
[6] Lemetr J.: *Damage mechanics*, The Bath Press, Great Britain, 1990, pp. 556.
[7] Bobyr M.I., Grabovskij A.P., Yakhno B.O.: *Damage Accumulation Model During Complex Low-Cycle Fatigue*, Vestnik NTUU "KPI". Masinostroenie, No. 44, 2003, pp. 13–15.
[8] Yakhno B.O., Bobyr M.I.: *About Damage Kinetic in the Construction Materials During Low-Cycle Loading*, Naukovi visti NTUU “KPI”, No. 6, 2004, pp. 75–78.

Analiza problemu zniszczenia materiału podczas zmęczenia niskocyklowego

W artykule zaprezentowano wyniki analizy i dyskusję nad problemem przewidywania trwałości zmęczeniowej w warunkach niskocyklowego, nieproporcjonalnego wieloosiowego obciążania materiału. Przedstawiono wyniki badań doświadczalnych stopu aluminium D16T. Analizowany materiał poddano różnym cyklom nieproporcjonalnego wieloosiowego obciążenia (rozciąganie, ściskanie, skręcanie). Zaprezentowane wyniki badań zostały potwierdzone analizą numeryczną.

ARCHIVES OF CIVIL AND MECHANICAL ENGINEERING

Vol. VIII 2008 No. 3

Computer modelling of valve lever forging with various preforms

P. CZYŻEWSKI, A. KOCAŃDA
Warsaw University of Technology, ul. Narbutta 85, 02-524 Warsaw, Poland

Application of CAE has become a common way to decrease a time for process planning and tool design in metal forming. Continuous development of numerical methods and software has provided advanced possibilities to solve various problems. In this paper a thermo-mechanical analysis of valve lever forging by means of SuperForge software was presented. There were taken into account various geometries of preforms, changes in temperature and internal stress distributions during subsequent forging stages in order to optimize metal flow. As the result, complete filling of die cavity without overlaps as well as reduction of flash volume has been obtained. Additionally, values of deformation force components (including side forces) were calculated what was helpful in a proper die design with counterlocks.

Keywords: *forging, die filling, side forces, forging process modelling*

1. Introduction

Progress in forging processes leads to requirements on increased geometrical accuracy of forgings and minimization of flash volume. In order to fulfill these requirements, there have been used various numerical methods and software in process planning phase. These methods have provided extensive possibilities for virtual analysis of alternative solutions of processes. Hence, it has been possible to pick out the best forging conditions. In such a case, a number of prototyping tools to find optimum conditions for the process could be substantially limited. This paper describes numerical modeling of valve lever forging by means of SuperForge software. There have been found process parameters to avoid folding and force components in the die cavity.

2. Valve lever forging

Geometry of the forging is shown in Figure 1. The selected forging could be regarded as asymmetrical in shape with extensive curved surfaces and flat parting surface. The forging made of 40HM steel is medium weighted (9.5 kg). Preform was cut off from square bar and heated. The tools were also heated before forging. Forging process consisted of four stages: initial upsetting of rod and next forging in fuller impression, blocker impression and finisher impression. Deformed material should fill out die cavity what depended considerably on a shape of preform. There were analyzed different shapes of preform. As the result of numerical analysis a suitable shape of preform was determined.

First version of preform (I) was elongated in the fuller impression which shape is shown in Figure 2. Second version of preform (II) was simplified in the shape. The modifications were initiated by taking into account the results of numerical analysis of forging process with the first preform.

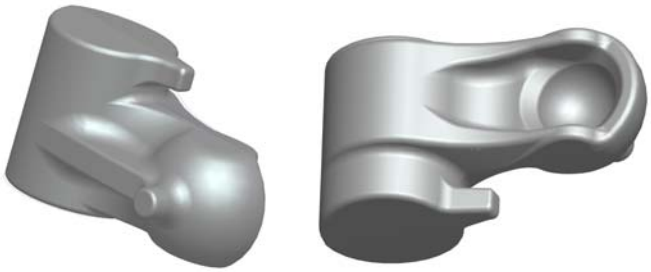

Fig. 1. Final shape of forged valve lever

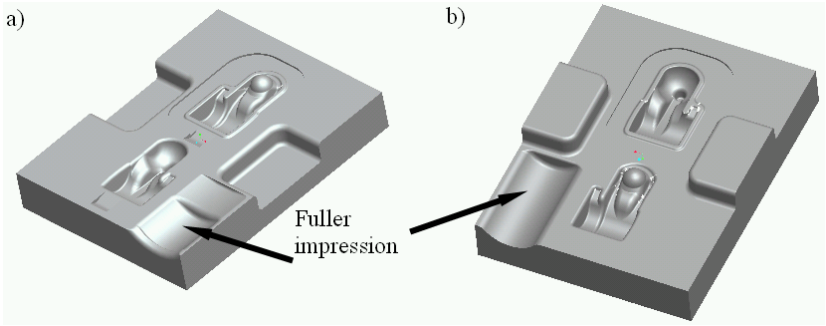

Fig. 2. View of upper (a) and lower (b) industrial dies with fuller, blocker and finisher impressions (version I)

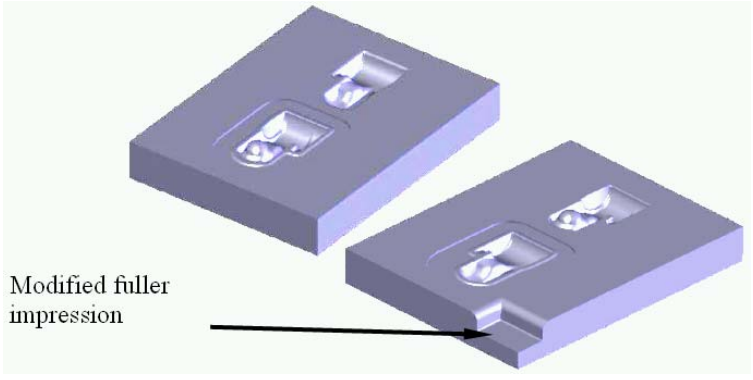

Fig. 3. Numerical models of dies with modified fuller impression (version II)

The third version of preform (III) was the ideal preform designed by taking into account distribution of material volume in the final forging with a flash. Having numerous cross sections of the forging with calculated volumes, the diameters of these cross sections were determined [1]. Finally, a shape of ideal preform was found, Figure 4. Numerical analysis of forging process was performed for all of the three versions of preforms.

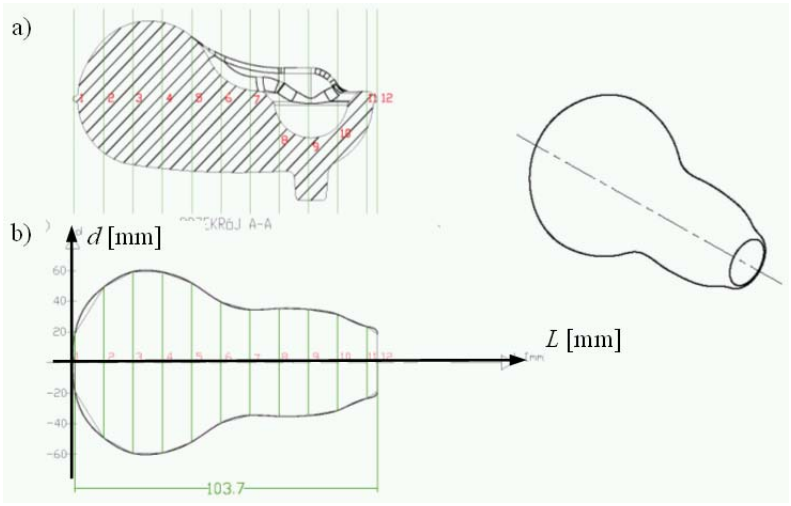

Fig. 4. Characteristic cross sections of the forging (a) and the ideal preform (b)

3. Numerical modeling of forging

Numerical modeling of forging with different versions of preforms was performed by means of SuperForge package and finite volume method. Geometrical models of dies were prepared by means of SolidWorks program. The dies were assumed as rigid bodies. Combined thermo-mechanical numerical analysis has taken into account all stages and blows of the forging processes. Geometrical changes, residual stress and temperature fields have been imported as data bases for all subsequent stages.

Forging process was analyzed for the following parameters:

- deformed material – medium carbon dispersion hardening ferritic-pearlitic steel DIN SCr415 (equivalent to PN 40HM steel),
- initial temperature of preform 1100 °C,
- initial temperature of die 250 °C,
- friction factor 0.3,
- crank forging press.

As for version of preforms I and II, numerical analysis was performed according to the following scheme: initial upsetting, first fullering, 90° rotation of the forged shape,

second fullering, forging in the blocker impression, forging in the finisher impression to get the final shape. View of the computer model of forging is shown in Figure 5. As for the third version of preform (III) the forging process consisted only with forging in the blocker and in the finisher impressions.

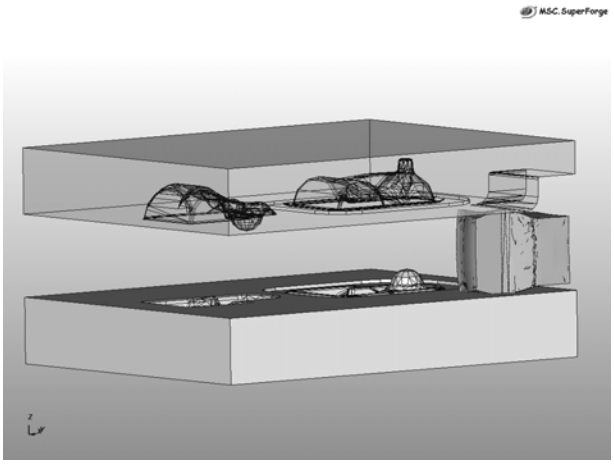

Fig. 5. Computer model of forging for the second version of preform just before starting the second fullering

4. Results of numerical analysis

Shapes of intermediate forgings after subsequent stages of the forging process are presented in Figure 6. First, detailed examinations of forgings were made in order to find some possible defects in the forgings resulting from the forging process itself. Two defects were found for forging with version I of preform:

- overlaps resulting from bending and excessive spreading of the flesh,
- inadequately filled forgings due to unsuitable shapes of preforms.

As shown in Figure 7, flash was too small in some areas what was related with inadequately filled die cavity. On the other hand, flash was too big in other areas and loss of material was too big. These problems indicated a need to change shape of preform to version II. The results of calculation for version II are shown in Figure 8.

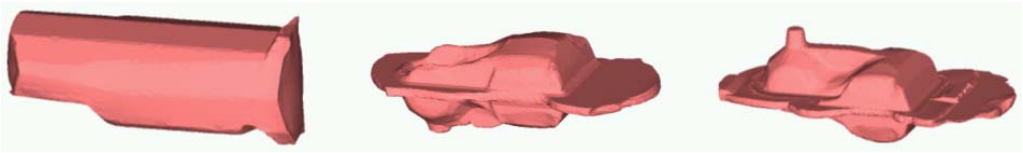

Fig. 6. Intermediate shapes of forgings (version I of preform); from left hand side: extension forging, blocker forging, and finisher forging

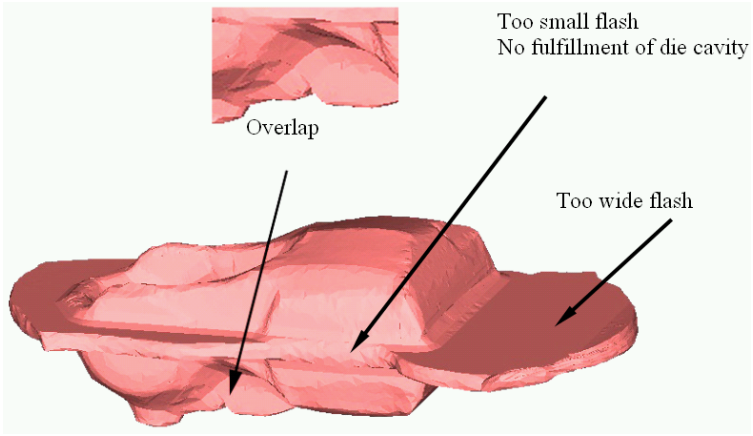

Fig. 7. View of forged shape after initial forging. Overlap and incorrect form of flash are pointed out

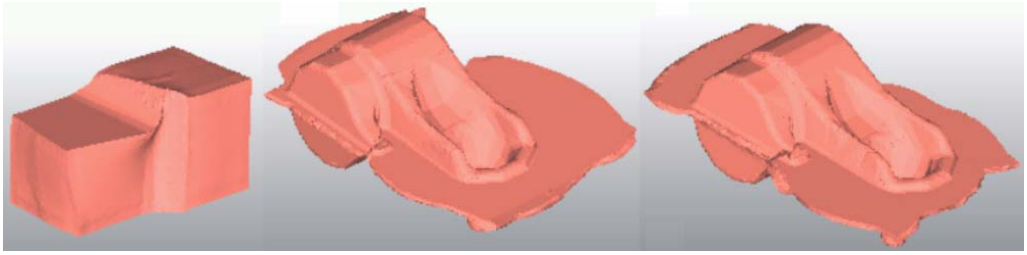

Fig. 8. Intermediate shapes of forgings (version II of preform); from left hand side: double fullering, blocker forging, and finisher forging

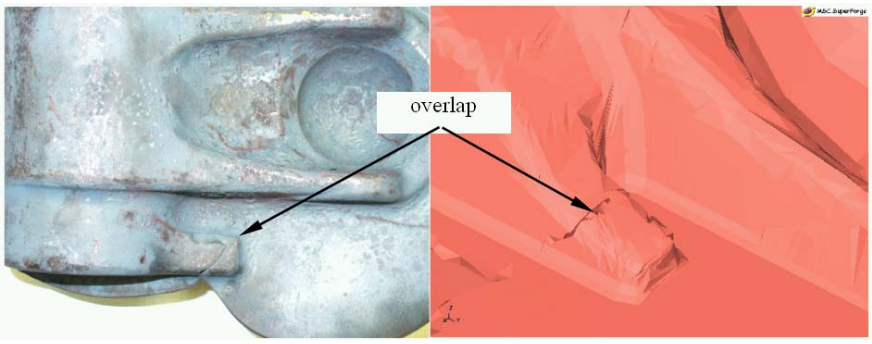

Fig. 9. An overlap formed in the forging; real production forging (left side) and numerical modeling of forging (right side) – version II of preform

A comparison of experimental and calculated results is shown in Figure 9. An overlap formed at the side of forging was exactly in the same place. Slight modifica-

tion of the version II of preform (with slight shortening of the preform length) moved the overlap into flash area what would be acceptable, Figure 10. Flash was sufficiently wide on the circumference of the forging but the width of flash was quite big in some areas. For that reason the ideal preform (version III) was tested in the next calculations. As for this case, no overlap was noticed and the flash was sufficiently narrow on the circumference of the forging, Figure 11.

Good results obtained for the ideal preform indicated the best solution for the preform shape. However, the shape of ideal preform would be quite difficult to obtain just by fullering in the die impression. The best solution would be to use special rolls. This means that the process would be more complicated and supported by additional rolling device. Then, higher quality of the forging could be obtained with higher cost of production.

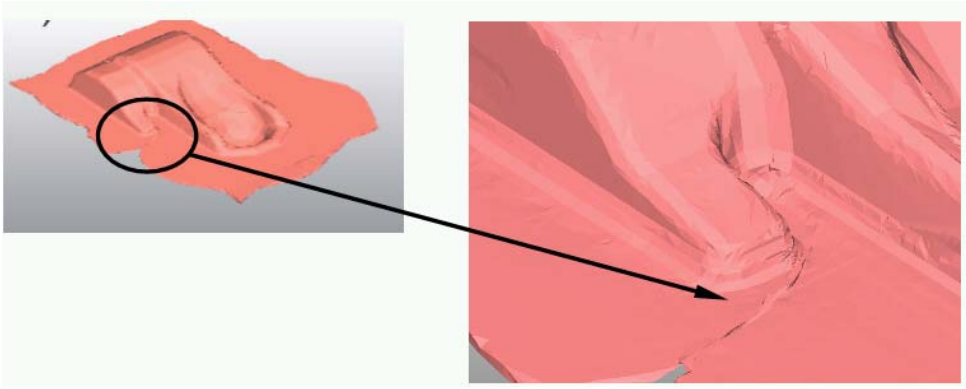

Fig.10. Geometry of forging for version II of preform

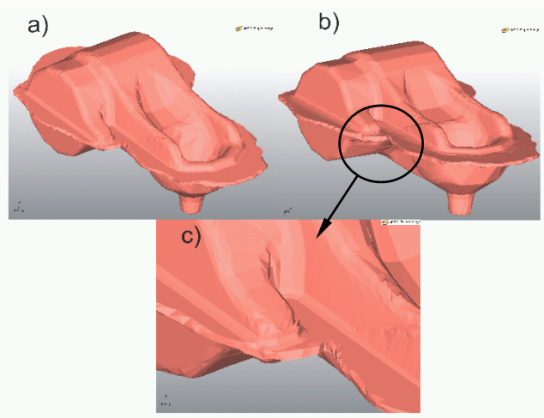

Fig. 11. View of forgings after forging in blocker (a) and finisher (b) impressions. The area which was critical for preforms I and II did not show any overlap for ideal preform III (c)

5. Side forces in die cavity

Numerical modeling enables exact control of metal flow and tool loading conditions. This leads, for example, to exact determination of deformation force components including side (or lateral) forces in the forging die [2–4]. Side forces are relatively high in production of asymmetrical or extended forgings what results in an offsetting of the upper and lower dies. This offsetting introduces geometrical inaccuracies into forgings or increased wear of some parts of die cavity. There are many ways to prevent sideways movement of the different parts of die set caused by side components of force but first the values and changes in the forces should be analyzed. Figure 12 presents history of changes in X and Y side components of forging force (working movements of dies are assumed to be exactly in vertical direction Z) for all three versions of preforms. In order to compare these three processes, some normalization of the values of forces was proposed. Rules of normalization are described as follows:

$$F_N = \frac{W_n^i}{W_{Z\,\max}^i} \cdot 100\%,$$

where:

N – direction of normalized force,

i – version of perform,

W_n – current value of side force,

$W_{Z\max}$ – maximum value of vertical force component for each version of preform.

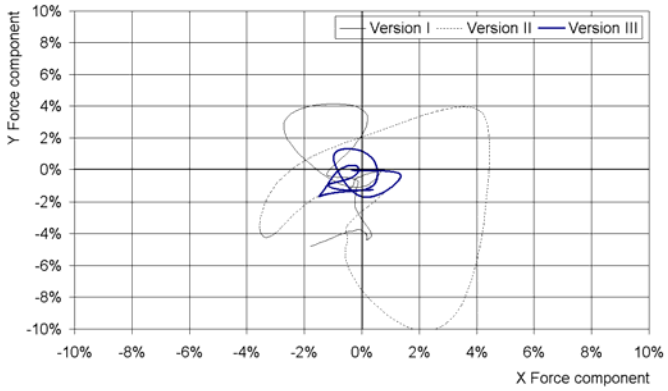

Fig. 12. History of changes in side forces X and Y for three versions of preforms

It could be seen from Figure 12 that version III of preform (ideal preform) resulted in the lowest values of side forces. Hence this version is the best from both accurate filling of die cavity without overlaps as well as minimized effects of side forces on geometrical accuracy of forgings points of view.

6. Concluding remarks

1. Three different versions of preforms were used in numerical modeling of valve lever forging. First preform was based on industrial process in which a piece of square bar was initially deformed in fuller impression. Second preform was a simplified version of the first preform and was proposed to decrease the effect of overlapping. The shape of this preform was found after analysis of results of numerical modeling.

2. The best filling of die cavity without overlaps and the best distribution of flash width on the circumference of the forging was obtained for so called ideal preform which shape was found analytically.

3. Side forces acting on die cavity were found by numerical analysis of forging process. The lowest side forces were found for the forging process with the ideal preform. Hence dies in this case would be subjected only to moderate offsetting which could be easily counterbalanced by a proper design of counterlocks.

Acknowledgement

This research work has been financially supported by the Ministry of Science and Higher Education, grant no. 4 T07D 037 29.

References

[1] Wasiunyk P.: *Die forging (In Polish)*, WNT, Warszawa, 1987.
[2] Kocańda A., Czyżewski P., Krzyszkowski P.: *Some developments in analysis of lateral forces and cyclic loading with relation to forging dies*, Proceedings of the 8th ICTP "Advanced Technology of Plasticity", Verona, 2005.
[3] Kocańda A., Czyżewski P.: *An influence of some process parameters on lateral forces in forging dies*, Computer Methods in Materials Science, Vol. 7, 2007, pp. 208–211.
[4] Kocańda A., Czyżewski P.: *Determination of side forces in a forging die*, Proceedings of 6th International Conference on Industrial Tools and Materials Processing Technologies, Bled, 2007, pp. 57–62.

Modelowanie numeryczne procesu kucia dźwigni zaworu dla różnych wariantów przedkuwek

Zastosowanie metod CAE jest jedną z efektywnych dróg do skrócenia czasu potrzebnego do projektowania procesów kucia. W artykule pokazano termomechaniczną analizę procesu kucia dźwigni zaworu z wykorzystaniem programu SuperForge. W analizowanym procesie przedstawiono wykorzystanie pakietu CAE do zaprojektowania procesu kucia w ten sposób, aby uniknąć wad kuźniczych. Dodatkowo przeanalizowano wpływ poszczególnych wariantów procesu na przebieg sił bocznych działających na matryce kuźnicze.

ARCHIVES OF CIVIL AND MECHANICAL ENGINEERING

Vol. VIII 2008 No. 3

The advanced forming process model including the elastic effects of the forming press and tool

KNUT GROßMANN, HAJO WIEMER, ANDRE HARDTMANN, LARS PENTER
Institute of Machine Tool and Control Engineering, Technische Universität Dresden, Germany

This article addresses process, stamping, and manufacturing engineers, as well as tool designers (prototype and series production tools), and press shop planners in the range of metal forming. The paper deals with methods of modelling and simulating the metal forming process and their application in product design, production, and forming process planning. In models usually applied major effects on the forming process are neglected. For instance, the elastic behaviour of presses and die tools is not considered in process and tool planning. Thus, reworking of tools is a consequence of this model oversimplification. The paper illustrates how interactions between forming press, tool and metal forming process can be modelled by enhancing conventional FE models. Several examples demonstrate the information value of the Advanced Forming Process Model (AFPM).

Keywords: *simulation of forming process, digital simulation of behaviour, virtual press, advanced forming process model, AFPM*

1. Introduction

Established as a powerful tool for sheet metal process planning, the Finite-Element-Simulation contributes to product engineering as well as production, process, and tool planning.

Currently applied process models merely consider the sheet metal component and the interface between sheet metal and tool, called workpiece-die interface [1]. Commonly, sheet metal components are described by shell elements with simple constitutive equations. The workpiece-die interface is represented by friction and contact law with constant coefficients. According to the actual state of FE-simulation the forming tool and machine are modelled as rigid i.e. the effect of the forming tool and machine on the forming process is neglected. In reality, both forming tool and machine evidently affect the forming process as required tool rework during the try-out demonstrates. Therefore, the purpose is to minimize time and effort in try-outs by using better simulation methods during the tool planning stage.

If quality and efficiency of metal forming processes are to be controlled already during the planning stage, interactions between subsystems machine, tool, work piece, and forming process need to be included in a complete forming model.

The Advanced Forming Process Model (AFPM) extended by effects of machine and tool is object of research work currently conducted at the “Institute of Machine Tools and Control Engineering” of the TU Dresden. In the following, some results are presented.

2. Ways of Model Advancement

Comprehensive modelling of the forming process demands coupling of subsystems as machine, tool, and work piece influencing the forming process. Principle concepts connecting the FE workpiece model (the common metal forming model) and press model are presented in [4]. Here, coupling variants are to be differentiated according to their way of integration.

- *Offline coupling (non-reactive)* is process characterization within the machine model based on process force progressions. Process force progressions calculated by the workpiece model are loaded from the FEA-environment via ASCII file into the press model [5]. Amongst others, this coupling method is applicable to analyze the operating performance of the machine and to detect the load on assemblies. In [5, 6] the ram deflections of a multi ram press were estimated. In [7] the effects of a tilted ram on the deep drawing process were analyzed.
- *Integrated coupling* is the workpiece model extended by a press model in the FEA-environment. The integrated FE-model realizes direct interaction between the process load and tool position as a result of the press behaviour. The concept describing the press by a reduced structure representing process relevant effects is exemplified in [2, 3].
- *Coupling of discrete models*, the machine effects are depicted in independent press models. Advantageously, the complex influences of the machine behaviour (drive, guidance system, frame, etc. [9]) are modelled in detail by Multi-Body-Simulation (MBS) while the workpiece description is made by FEM. Thus, two simulation tools (MBS and FEM) connected by simulator coupling are to be applied. The simulator coupling organizes the exchange of data and synchronizes the different solution algorithms. A complete forming model by coupling discrete simulation models is exemplified in [8].

To design the forming process, only press behaviour directly affecting the process is relevant. Interactions between assemblies inside the press are less important. Hence, the integrated solution realized in [2, 3] is adequate. Furthermore, applying the integrated approach avoids the independent major problem of coupling different simulation software.

3. AFPM considering elastic press effects

3.1. Relevant static effects

Accuracy defining effects of the press based on its deformation and deflection behaviour are significant to the sheet metal forming process [2]. In standard [10], these effects are determined as accuracy parameters of presses. For the time being, only static effects are to be considered by the model advancement:

- vertical total stiffness c_{totZ},

- horizontal total stiffness c_{totX} and c_{totY},
- resistances against tilt (tilting stiffness) c_α and c_β.

The resulting stiffness parameters combine all static effects of the press assemblies each regarding to one degree of freedom in the press' coordinate system.

3.2. Press model

In the following, step by step the above mentioned press effects are added to the AFPM. Currently, tool components are handled as rigid bodies as described above. Therefore it is sufficient to define the tool bearing on a rigid ram. A rigid ram takes the advantage of directly applicable principle stiffnesses of the press describing the effects by concentrated parameters. The concentrated stiffnesses are connected to the centre of gravity of the ram as shown in Figure 1a.

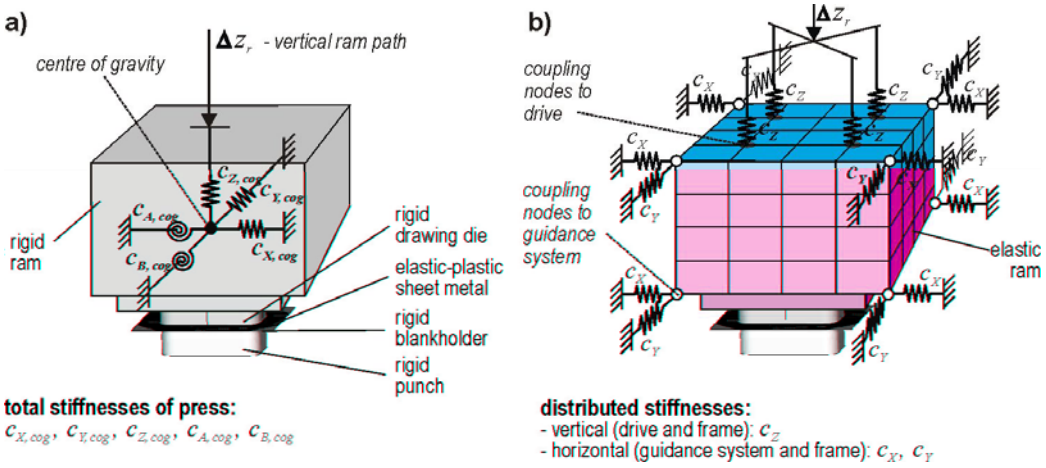

Fig. 1. Advanced Forming Process Model AFPM: a) extended by a press model considering elastic mounting of the rigid ram in the centre of gravity; b) extended by press model separated in drive and guidance springs for the application of an elastic ram (example: O-frame press with 4-point configuration)

Hence, forming process models will be enhanced by elastic tool models demanding elastic embedding in the machine. That implies that the press has to be modelled by an elastic ram and an elastic table of the press. Analogously to real press structures the bearing of the elastic ram in the press is determined by drive and ram guidance.

Figure 1b illustrates the AFPM extended by distributed spring elements. On the corner nodes spring elements in horizontal direction (X- and Y-) and in vertical direction (Z-) according to the drive system are connected to the ram model. Via position and parameterisation of this spring elements the following properties are educible:

- principle stiffnesses of presses,

- drive system (1-, 2-, and 4-point configuration),
- frame stiffness and design (C-frame and O-frame) and structure (frame, ram, table of the press),
- guidance (with and free of clearance).

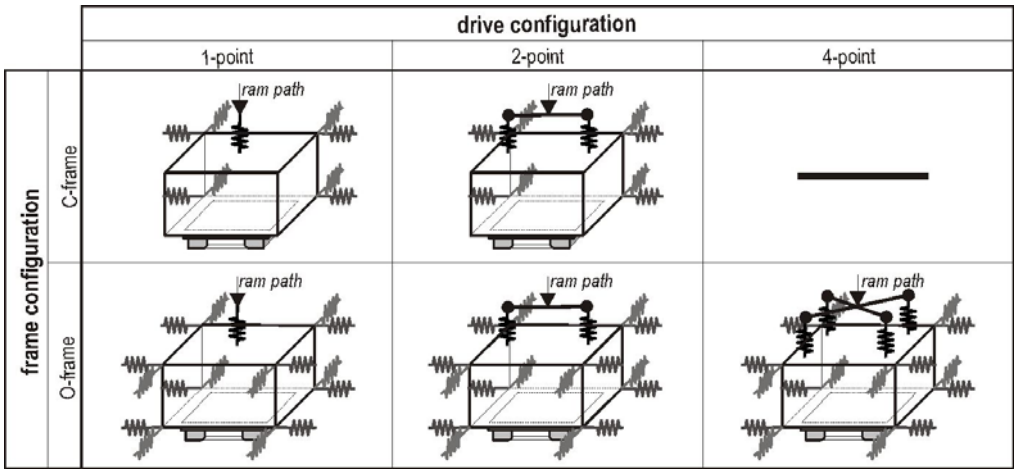

Fig. 2. Scheme of press models for different press structures

Press models for different press structures are charted in Figure 2. The stiffness values of horizontal and vertical spring elements can be obtained by measured values based on [10]. The conversion of tilting stiffnesses c_α, c_β and total vertical stiffness c_{totZ} into spring constants c_X, c_Y and c_Z is carried out using a moment balance system. For this purpose geometrical parameters as ram size and distance between force transmitting drive elements x_{dr} and y_{dr} are necessary. Equations (1–3) exemplify this correlation for an O-frame press with a 4-point configuration.

$$c_x = \frac{c_\alpha - \frac{c_{totZ} \cdot x_{dr}^2}{4}}{2 \cdot z_{ram}^2}, \tag{1}$$

$$c_Y = \frac{c_\beta - \frac{c_{totZ} \cdot y_{dr}^2}{4}}{2 \cdot z_{ram}^2}, \tag{2}$$

$$c_Z = \frac{c_{totZ}}{4}. \tag{3}$$

3.3. Example "effects of press stiffnesses"

As an example, the AFPM is applied to the following press configurations:

- Model 1: rigid (free of elastic bearings)
- Model 2: O-frame press with 4-point configuration (c_{totZ} = 1250 kN/mm; $c_\alpha = c_\beta$ = 125 MNm) and
- Model 3: C-frame press with 1-point configuration (c_{totZ} = 630 kN/mm; c_α = 45 MNm; c_β = 32 MNm)

The parameters appropriate to a 1000 kN press were obtained from [11]. To get marked effects regarding to tilting an eccentric load case was implemented by eccentric tool positioning.

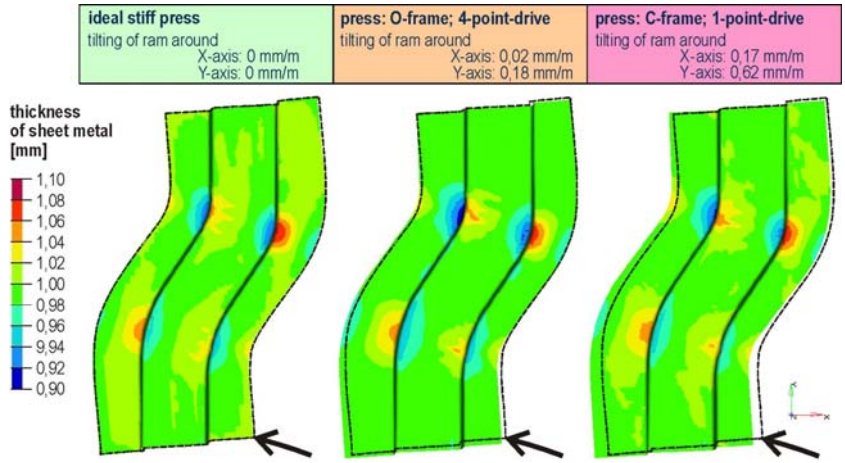

Fig. 3. Thickness distribution and sheet metal flow at a drawing depth of 40 mm for the "S-Rail"

The computer simulation refers to single action presses with hydraulic die cushion. The blankholder force defined as constant in stroke is represented by a constant distributed load applied on the blankholder surface. The simulation results (LS-DYNA) shown in Figure 3 illustrate the increasing effect of ram tilting to sheet metal flow and thickness as a consequence of an eccentric process load (tool assembled 200 mm eccentric in X-direction) and press stiffness. The effect to the material flow is clearly recognizable. This behaviour is justifiable by the asymmetric distributed compression at the contact area in the flange.

3.4. Example "compensation of press effects"

The example demonstrates the feasibility to realize the tool tryout in Virtual Reality. Previous, ram tilting was calculated under process load. The effect of ram tilting can be compensated by an inclined tool installation.

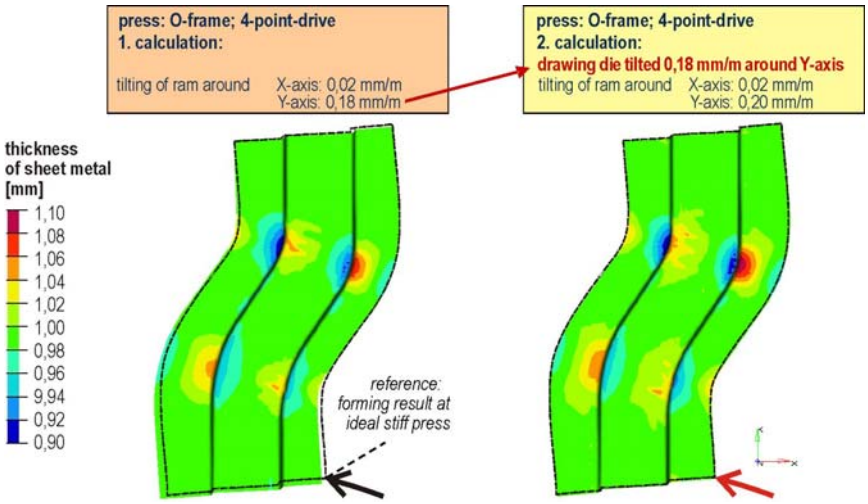

Fig. 4. Compensation of press effects (ram tilting) by inclined die installation (thickness distribution and sheet metal flow at a drawing depth of 40 mm for the "S-Rail" part)

Figure 4 displays the simulation results. On the left, the sheet metal flow in case of a straight assembled tool is illustrated. In comparison with the ideal press (free of tilting) the machine effect is in evidence. The result on the right side verifies that the variation of sheet metal flow caused by ram tilting was compensated by inclined tool installation.

4. AFPM extended by elastic die cushion effects

4.1. Relevant static die cushion effects

An elementary influence on contact and friction conditions at the interface between die and blankholder results of the blankholder. According to the usual practise, in the AFPM describe above the blankholder is represented by a constant distributed load on the blankholder surface. But in reality the distributed load on the blankholder surface results from the equilibrium between process load variable in time and place, blankholder deflection and deformation, respectively. Demonstrating this essential effect on drawn parts in the forming simulations demands the extension of the model by the deformation and deflection of the blankholder. First preparatory works for advanced research studies planned in [12] led to the following approach.

4.2. Die cushion model

The blankholder shape under process load depends on its elastic properties. Its location is determined by elastic properties of:

- the press (drive, blankholder ram, ram guidance, frame) in case of double action press or
- the die cushion (drive, die cushion plate, guidance) in case of a single action press and
- the tool guidance.

To model the blankholder bearing in case of a double action press the prefixed press models are applicable. In order to realize the blankholder bearing of a die cushion the model structures were successively developed, first to apply rigid and then elastic blank holders [9].

The die cushion model for an elastic blankholder is shown in Figure 5. The stiffnesses of die cushion drive, guidance, pressure pin, and pin guidance are represented by substitutional springs. This spring elements are arranged on the coupling nodes of the elastic blankholder as they are in the real structure. The stiffness of the spring element was parameterized according to [13].

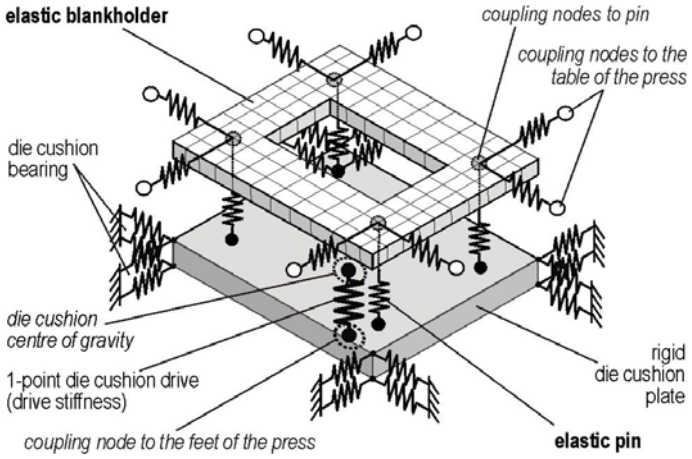

Fig. 5. Model structure of the die cushion for applying an elastic blank holder

4.3. Example "effect of die cushion bearing stiffness"

The example visualizes how die cushion and blankholder affect the deep drawing process of a rectangular tub. The process models 1 to 3 of the previous example were extended by an elastic die cushion bearing.

The simulation results of the process models with integrated die cushion model are shown in Figure 6. It illustrates sheet thickness and flow in forming process models with different levels of abstraction. For comparison, in Figure 6 the conventional forming process model (rigid machine, tool, and die cushion model) is displayed. Due to a constant distributed load across the contact surface the tub possesses a symmetric sheet thickness distribution and a symmetric sheet metal flow. In contrast, applying

the AFPMs the eccentric tool location results in ram tilting (see Figure 6b) or in ram and blankholder tilting (see Figure 6c), respectively. Tilting leads to asymmetric thickness distribution and asymmetric sheet metal flow. In this example, the effect of the blankholder deflection to the drawn part is stronger than the tilting of the ram.

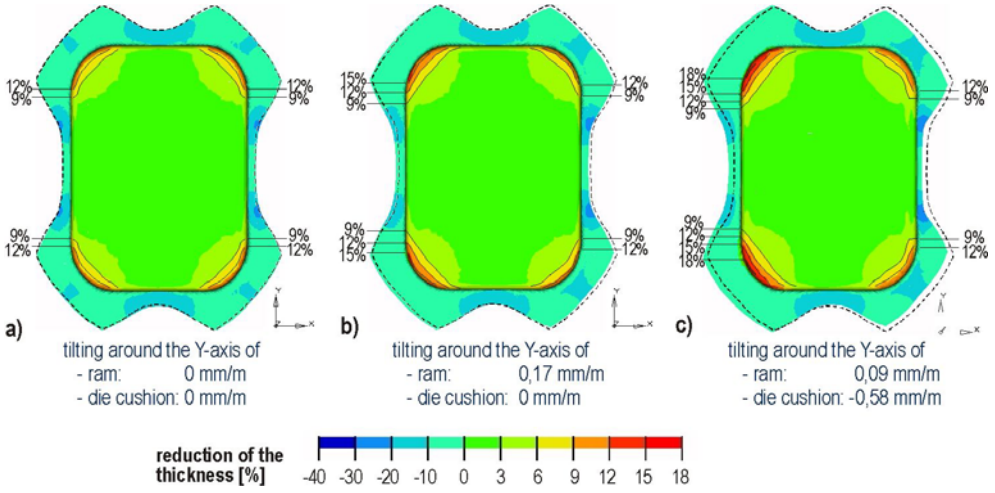

Fig. 6. Sheet thickness reduction and material flow, O-frame press with 1-point configuration: a) rigid press and tool, rigidly supported die cushion, b) elastic press, rigidly supported die cushion, rigid tool, c) elastic press, elastically supported die cushion, rigid tool

The deformations and surface pressures on the blank-holder according to the results in Figure 6 show different distributions corresponding to the interactions between the die cushion, machine and process and justify the sheet metal flow as shown. In all calculations the resulting blankholder force was the same.

5. Experimental verification

5.1. Experimental equipment

In order to verify the modelling concept with experiments the single action hydraulic press Wanzke HPV 160 is available at the IWM. Initially, the static tilting and stiffness behaviour of the press is determined by inducing a defined moment with the press testing equipment. The diagram shown in Figure 7a displays the tilting behaviour of the ram around the X- and Y-axis. These characteristic tilting curves result in the tilting stiffness c_α, and c_β as well as in the vertical total stiffness c_{totZ}. These values are converted into the stiffness parameters of the horizontal and vertical spring elements c_X, c_Y and c_Z of the FE model for an O-frame press with a 1-point driving system.

a)

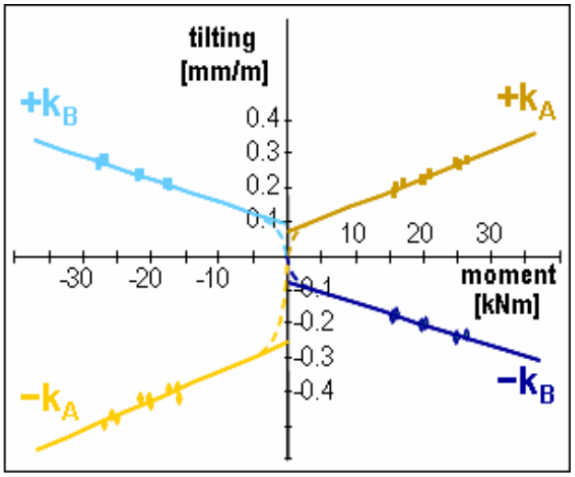

b)

nominal force	F_N [kN]	1600
vertical stiffness	c_{totZ} [kN/mm]	1015
vertical initial deflection	v_{aZ} [mm]	0,1
tilting stiffn. around X	c_α [MNm]	120
inital tilting around X	k_A [mm/m]	0,2
tilting stiffn. around Y	c_β [MNm]	156
initial tilting around Y	k_B [mm/m]	0,1
clamping width	x_0 [mm]	800
clamping depth	y_0 [mm]	780
width of ram	x_{St} [mm]	1000
depth of ram	y_{St} [mm]	780
heigth of ram	z_{St} [mm]	730
dist. of driving points	l_0 [mm]	-

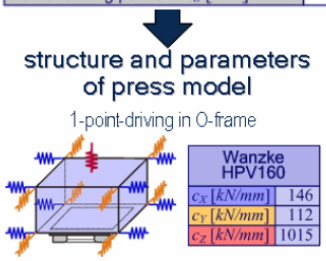

Fig. 7. Press characteristics of Wanzke HPV 160: a) tilting around X-axis (k_A) and Y-axis (k_B), b) structure and parameters of the press model

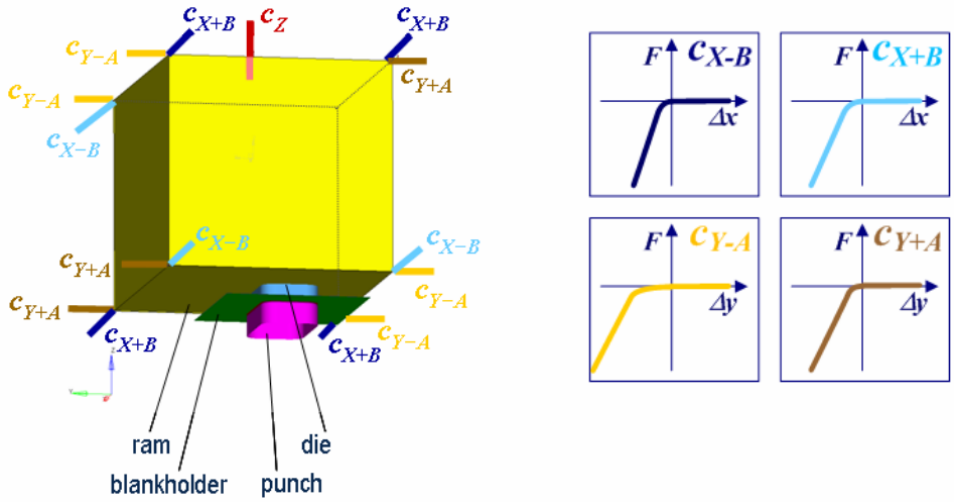

Fig. 8. Press model Wanzke HPV 160 with non-linear compression springs

Since the approach to use linear-elastic springs does not correspond with the real tilting and stiffness behaviour of the experimental press the press model is refined with non-linear spring characteristics. In order to consider the tilting behaviour, which

is dependent on the direction of the rotation, only non-linear compression springs are attached to the corner nodes of the ram (as clarified in Figure 8).

The rectangular tub shown in Figure 11 is selected as specimen for the experimental verification. The stiffness properties of the experimental tool are modified by implementing disc springs in the die to be able to vary the total stiffnesses in the press-tool system (Figure 9).

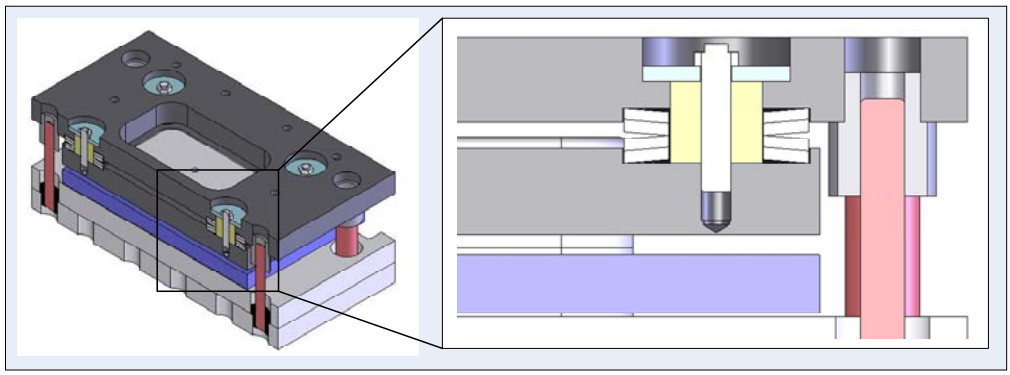

Fig. 9. Modification of the total stiffness and the tilting stiffnesses in the experimental tool by variable disc springs

5.2. Advanced forming process model of the experimental equipment

Initially, in the FE simulation setup with non-linear springs, the blank holder is rigid but is allowed to tilt. In the simulation a different tilting behaviour due to an asymmetrical tool installation in the press is observed, but no correlations with the deep drawing failures in the experiment are found. Therefore, it is necessary to setup a more comprehensive forming process model (Figure 10) in LS-DYNA, which considers the elastic properties of the press HPV 160 containing the die cushion, forming tool, and disc springs.

Since the die cushion of the experimental press is not guided but attached to the cushion cylinder only, an analogous substitute spring model is applied. The layout of the blankholder springs is derived from the properties of the die guidance. The values to parameterize the stiffnesses are obtained from the literature [13]. Due to performance and stability reasons (mass scaling, damping) the relative tool movement is realized by driving the punch (which is fixed in space in reality) instead of driving the ram.

5.3. Comparison of simulation and experiment

The performance of the advanced process model is demonstrated by integrating a specific disc spring setup in the experimental tool. The bearing of the die on the vari-

able disc springs allows for adjustment of different total stiffnesses within the press-tool system. Figure 11 shows an asymmetrical loading case.

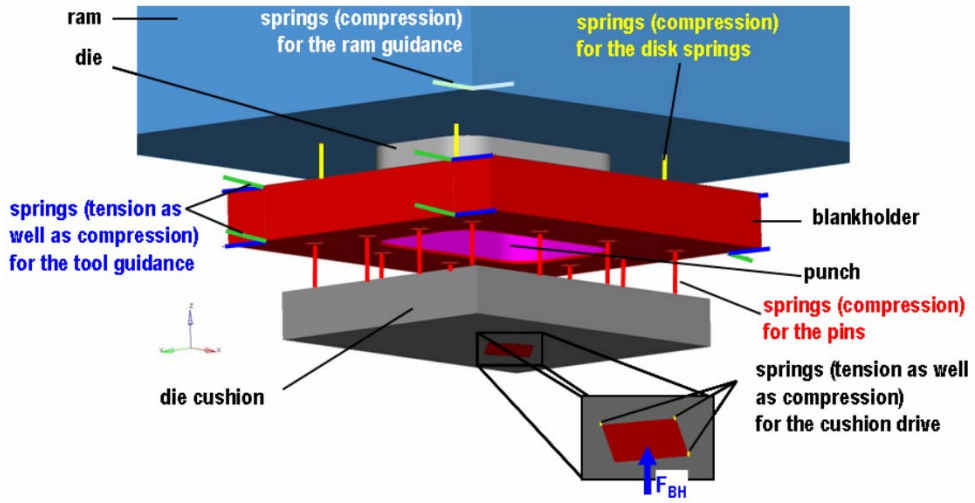

Fig. 10. Forming process model considering the elastic properties of press HPV 160

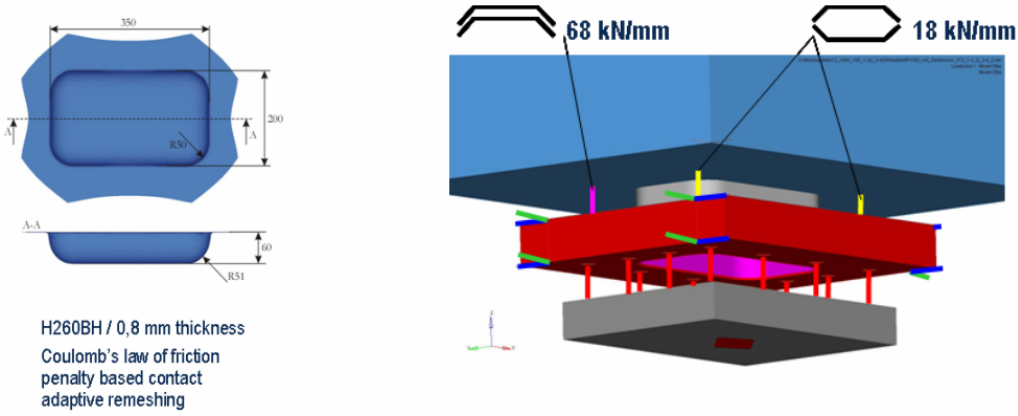

Fig. 11. The specimen and the asymmetrical load case selected for the verification

The draw-in and the thickness distribution of the drawn cup are measured for different blankholder forces. The drawing failures (such as wrinkles and cracks) and their point of origin are identified.

In the simulation setup the blank is meshed with shell elements, the blank material H260BH is described by the anisotropic model HILL3R and adaptive net refinement is applied. The tribological conditions are described by the Coulomb's law of friction and a penalty based contact algorithm.

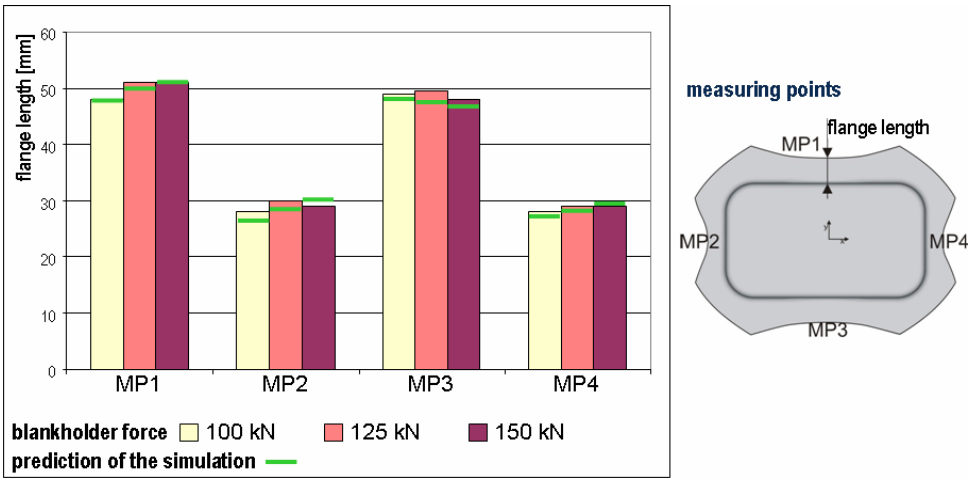

Fig. 12. Comparison between the results of the simulation and the experiment – length of the remaining flange at different blankholder forces

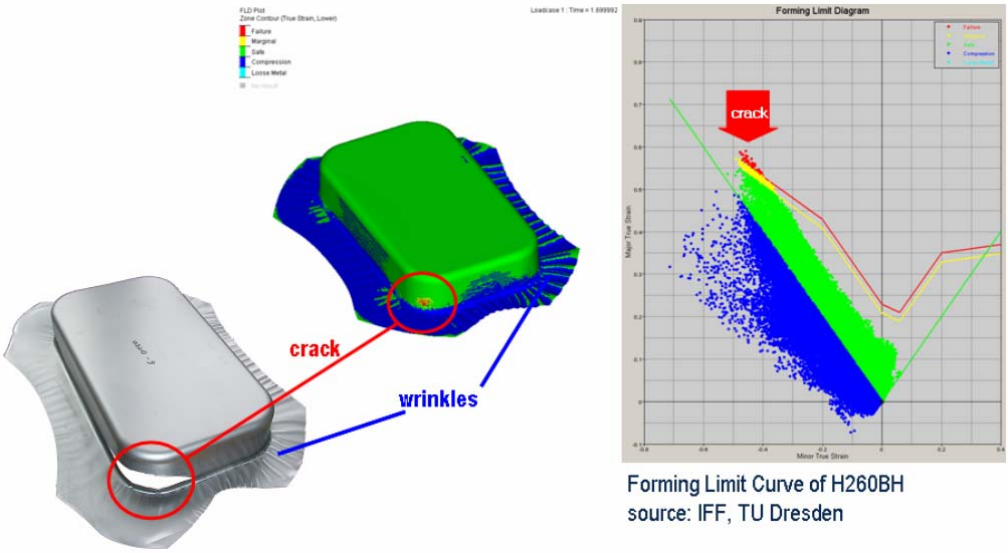

Fig. 13. Comparison between the results of the simulation and the experiment – analysis of the drawing failures using a FLC

The prediction of the simulation matches well to the experimental results as illustrated by the draw-in at the four edges of the remaining flange in Figure 12. Furthermore, the prediction of the wrinkles and cracks using a forming limit curve are confirmed by the experimental results (see Figure 13).

6. Conclusion and Outlook

Based on conventional process modelling in FE systems and analysis of the relevant effects of the press, tool, and die cushion on the forming process an advanced modelling method is developed.

The simulation results obtained by applying the AFPM and a conventional model of forming process (without elastic press, tool, and die cushion effects) are compared. The comparison shows, that the relevant static effects of the press, tool and die cushion on the forming process can be visualised by the advanced process model.

By using an example of a rectangular tub drawing tool and the associated experimental equipment it is shown that the simulation results match the experimental o.

A complete forming process model is available to consider different configurations of presses and die cushions in the process planning stage. Thus, the effort in the tool try-out and the ramp-up can be reduced by using the FE simulation.

The current research works have following main objectives:

- systematic development of models for various die cushions,
- extension of the AFPM by the tool guidance and analysis of effects on the forming process,
- applying practicable methods to reduce large FEA-tool models to handle tool models as elastic bodies,
- including of kinematic and dynamic behaviour.

References

[1] Roll K., Wiegand K.: *Eine Möglichkeit zur Berücksichtigung der Werkzeugelastizität bei der Blechformsimulation*, "Neuere Entwicklungen in der Blechumformung" Leinefelden-Echterdingen (Stuttgart), MAT INFO Werkstoff-Informationsgesellschaft mbH, Frankfurt, 2006.

[2] Großmann K., Hardtmann A., Wiemer H.: *Simulation des Blechumformprozesses unter Berücksichtigung des statischen Verhaltens der Pressmaschine*, *Simulation of the sheet metal forming process considering the static behaviour of the press*, ZWF Zeitschrift für wirtschaftlichen Fabrikbetrieb, 101, No. 10, 2006, pp. 600–605.

[3] Großmann K., Wiemer H., Hardtmann A., Penter L.: *Stand der Simulation von Umformprozessen mit den elastischen Einflüssen aus Maschine und Werkzeug*, Tagungsband T 27 des EFB-Kolloquiums „Neue Wege zum wirtschaftlichen Leichtbau" in Fellbach, EFB, Hannover, 2007, pp. 185–198.

[4] Großmann K., Wiemer H.: *Maschine, Werkzeug und Prozess – ein ganzheitliches System*, "6. Sächsische Fachtagung Umformtechnik", Dresden, 1999.

[5] Großmann K., Wiemer H., Thoms V., Schirmacher F.: *Modellierung des Blechumformprozesses in der Anlagensimulation auf Grundlage von Ergebnissen der FEM-Prozeßsimulation*, EFB-Forschungsbericht, No. 178, EFB Hannover, 2001.

[6] Großmann K., Wiemer H.: *Simulation of the Process Influencing Behaviour of Forming Machines*, Steel research international 76, Verlag Stahleisen GmbH Düsseldorf, No. 2/3, 2005, pp. 205–210.
[7] Schirmacher F., Wiemer H.: *Kopplung von Prozess- und Anlagensimulation – ein wesentlicher Teilschritt auf dem Weg zum „Virtuellen Umformen"*, Tagungsband T 21 des EFB-Kolloquiums „Prozessoptimierung in der Blechverarbeitung" in Fellbach, EFB Hannover, 2001, pp. 11.1–11.18.
[8] Brecher C., Schapp L., Paepenmüller F.: *Gekoppelte Simulation von Presse und Massivumformprozess*, Werkstattstechnik online Jahrgang, 96, 2006, pp. 7/8.
[9] Wiemer H.: *Stand und Möglichkeiten der Systemsimulation von mechanischen Pressmaschinen*, *State and Potentials of Forming Press Simulation*, Dissertation, TU Dresden, 2004.
[10] N.N.: *German Standard. Deutsche Normschrift DIN 55189: Ermittlung von Kennwerten für Pressen der Blechverarbeitung bei statischer Belastung*, Beuth Verlag Berlin, 1988.
[11] N.N.: *German Standard. VDI-Richtlinie VDI 3145: Pressen zum Kaltmassivumformen. Blatt 1: Mechanische und hydraulische Pressen*, VDI-Verlag Düsseldorf, 1985.
[12] Großmann K., Hardtmann A., Wiemer H.: *Entwicklung und Bewertung von Simulationstechnologien für die Blechumformung unter Berücksichtigung der Wechselwirkungen zwischen Maschine-Werkzeug und Prozess-Werkstück*, laufendes Vorhaben der DFG im SPP, pp. 1180.
[13] Pahl K.J.: *Elastische Wechselwirkungen im Ziehapparat einfach wirkender Pressen*, VDI Verlag, Düsseldorf, 1994.

Zaawansowany model procesu kształtowania plastycznego uwzględniający sprężyste odkształcenie prasy i narzędzie

Artykuł dotyczy procesów tłoczenia i kierowany jest do inżynierów produkcji, jak również projektantów procesów i narzędzi (ich prototypów i produkcji seryjnej narzędzi). Publikacja ukazuje metody modelowania i symulacji procesów kształtowania plastycznego metalu i ich zastosowania w projektowaniu produktu i produkcji. W zwykle stosowanych modelach procesów kształtowania efekty sprężyste są pomijane. Na przykład sprężyste zachowanie pras i matryc nie są brane pod uwagę podczas projektowania narzędzi, powoduje to ich częste przerabianie już w trakcie procesu rzeczywistego. Artykuł ilustruje jak wzajemne relacje między prasą, matrycą i procesem kształtowania plastycznego mogą zostać zamodelowane poprzez ulepszanie konwencjonalnych modeli MES. Zostało to zademonstrowane na kilku przykładach.

ARCHIVES OF CIVIL AND MECHANICAL ENGINEERING

Vol. VIII 2008 No. 3

Automotive component development by means of hydroforming

A. KOCAŃDA, H. SADŁOWSKA
Warsaw University of Technology, ul. Narbutta 85, 02-524 Warszawa, Poland

Hydroforming processes have become popular in recent years, due to the increasing demands for lightweight parts in various fields, such as bicycle, automotive, aircraft and aerospace industries. This technology is relatively new as compared with rolling, forging or stamping, therefore there is not much knowledge available for the product or process designers. Comparing to conventional manufacturing via stamping and welding, tube (THF) and sheet (SHF) hydroforming offers several advantages, such as decrease in workpiece cost, tool cost and product weight, improvement of structural stability and increase of the strength and stiffness of the formed parts, more uniform thickness distribution, fewer secondary operations, etc. The paper presents extensive possibilities of component development in automotive industry by means of hydroforming processes. There are also presented some examples on computer modelling of these processes and limiting phenomena.

Keywords: *hydroforming, THF, SHF, FEM*

1. Introduction

Hydroforming uses fluid pressure in place of the punch as comparing with a conventional tool set to form the component into the desired shape of the die. Generally, hydroforming processes would be classified as tube or sheet hydroforming depending on the initial shape of workpiece. In the tube hydroforming process (THP), the initial workpiece is placed into a die cavity, which corresponds to the final shape of the component, Figure 1. Next, the dies are closed under the force and the tube is internally pressurized by a liquid medium to effect the expansion of the component (internal pressure, p_i) and axially compressed by sealing punches to force material into the die cavity (axial force, 2). Hence the component is formed under the simultaneously controlled action of p_i and axial force. The process should be controlled to avoid failures such as buckling, wrinkling and bursting.

Appropriate fundamentals to determine process controls were developed by experimental approaches as well as by means of FE simulations, e.g. [1–6]. Water–oil-emulsions are typically used media to apply internal pressure, which is usually increased to 250 MPa, and in certain cases up to 600 MPa. The necessary amount is influenced significantly by the wall thickness of the component, the material strength and hardening as well as by the component shape [7–10].

The hydroforming is very useful for producing whole components that would otherwise be made from multiple stampings joined together. For example, a typical chas-

sis component that would normally be made by pressing up to six channel sections and joining by spot welding can be hydroformed as a single part. Other examples of hydroformed parts from automotive industry are shown on Figure 2.

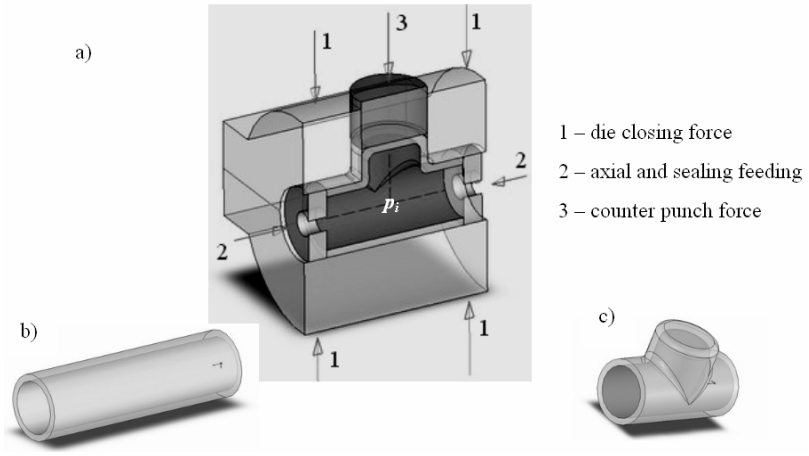

Fig. 1. The hydroforming principles: a – tool setup, b – initial tube, c – final product (T-joint)

In the majority of cases the complexity of the components requires that additional preforming operations are considered together with the hydroforming process itself. These preforming operations can involve bending and mechanical forming of the initial component to ensure that it is capable of insertion into the hydroforming die or to obtain an optimized material distribution [13].

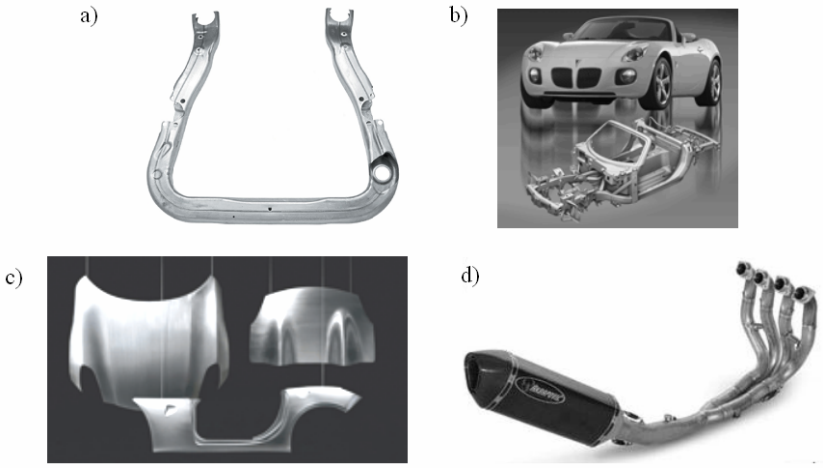

Fig. 2. Industrial examples of tube and shell hydroforming: (a) – engine cradle [0], (b), (c) – Pontiac Solstice and parts made by hydroforming [12], (d) – exhaust system of Kawasaki [14]

In the last few years, the demand for weight reduction in modern vehicle construction has led to an increase in the application of hydroforming processes for the manufacture of automotive lightweight components made from steel or aluminium. It results from improvements in stiffness and crash behaviour due to the reduction of welding seams, and with reduced assembly costs. Currently, use of aluminium alloy which is light weight material is increasing. Extruded aluminium profiles have been used for automobile frame parts [10] to get higher stiffness and light weight, Figure 3. Many progresses have been made in forming of square sectioned profile by stretch bending [12, 15] and hydroforming [16–17].

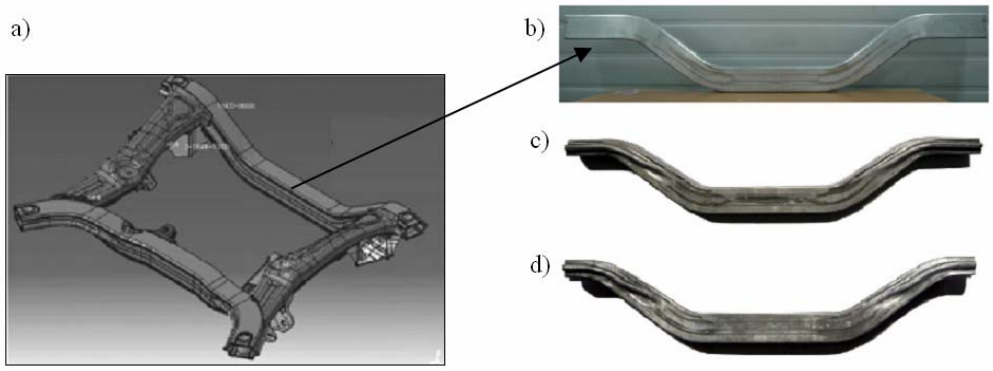

Fig. 3. Part of the subframe (a), photographs of forming of the extruded profile: bending (b), pressing (c), hydroforming (d) [21]

The use of lightweight materials such as aluminium and magnesium can reduce the weight of passenger vehicles up to 40–75% by replacing ferrous auto body structures and body panels [18]. It was reported that a 10% weight reduction in an average automotive body could improve the fuel efficiency by 6–8% [19]. However, the cost for the lightweight materials is estimated to be higher than that of the mild steel structures because of the raw material price and the production costs with the existing manufacturing technologies. For aluminium alloys, the cost increases up to 30–100% are expected while it is forecast to be around 50–150% for the magnesium alloys [18]. On the other hand, since 80% of the total energy consumption throughout the life cycle of an automobile occurs during the utilization (driving) period, the use of lightweight parts is still seen as a prominent, long-term and cost effective response to the fuel efficiency and the emission reduction demands [20].

Considerable mass savings are possible through eliminating the flanges required for welding and using thinner steel. In spite of that, stiffness is still maintained and the discontinuous spot-welded joints are eliminated [21, 23–24]. Figure 4 presents main part of exhaust system for motorcycle Kawasaki Zx 10 R produced by conventional methods and by hydroforming. Shape of hydroformed parts is more complicated but

very smooth and harmonic. What more, cost of hydroforming of these complicated parts has been lower than cost of producing and joining many parts by conventional processes.

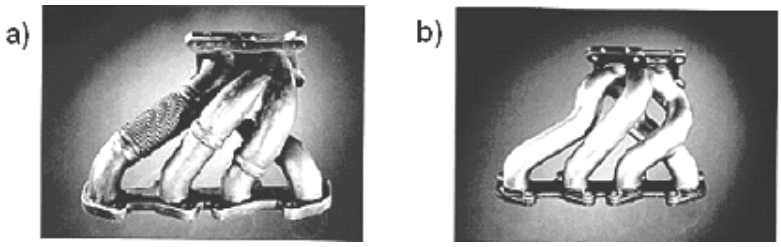

Fig. 4. Comparison of exhaust systems produced by conventional methods (a) and by hydroforming (b) [14]

Hydroforming has already been widely used in the US – more than a million engine cradles a year are produced by hydroforming processes. Some 2.8 million components a year for one of Chrysler's model are produced by hydroforming, too. In Europe the technology is being used in sub-frames for models such as Ford's Mondeo and General Motors's Vectra. Hydroforming is well advanced in Germany. However, as hydroforming – particularly high-pressure hydroforming – is at the frontier of modern steel technology, many designers and engineers still need convincing of its capabilities [24].

2. Sheet hydroforming

Today, predominantly tubular material is considered for the mass production of hydroformed parts. Hydroforming of sheet material (SHF) is up to now mainly used for small batch production due to a comparatively high cycle time. Furthermore, sheet hydroforming requires higher clamping forces than tube hydroforming, causing more cost-intensive presses. However, advances in process and press technology, e.g. [3–6], increasingly contribute to a wider industrial application of sheet hydroforming, in particular for the flexible manufacture of small batch sizes. One of the first examples for an industrial application is the sheet hydroforming of roofs for luxury class cars, Figure 5.

Figure 6 shows the scheme of a sheet hydroforming. When the punch pushes the sheet metal into the die cavity, within which oil or other liquids are contained, pressure p_i that can press the sheet metal tightly onto the punch will be generated. At the same time, the liquid in the die cavity will flow out between the upper surface of the die and the sheet metal, what results in reduction of frictional forces. By this process, the limit drawing ratio value of sheet metal can be increased. The liquid can be used as a punch, a draw die or an assisting way to improve sheet formability. Actually, almost all of the materials used in conventional stamping can be used in sheet hydroforming.

Depending on the different means, the liquid pressure in the die cavity is from around 30 to 150 MPa, but the usage of 200 MPa has also been reported [13, 25]. Roof for luxury class car (Figure 5), deep and partially conical cup (Figure 7) or cups with complicated geometries of bottoms (Figure 6) are examples of parts made by sheet hydroforming.

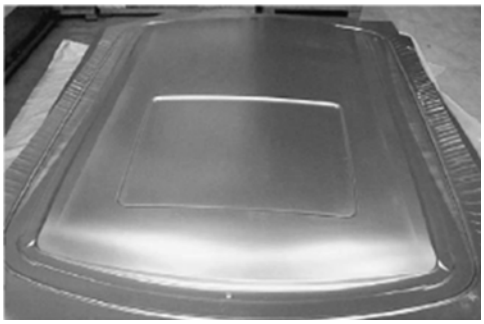

Fig. 5. Roof for luxury class cars [23]

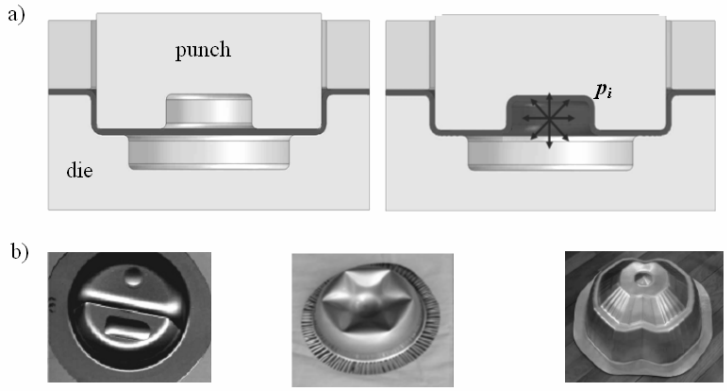

Fig. 6. Scheme of sheet hydroforming (a) and examples of products (b) [13]

It is well known that formability of the lightweight materials usually increases at elevated temperature levels [27–28].Warm forming technology with selective heating enables manufacturing of lightweight parts by utilizing the increased formability at elevated temperature [28]. However, it is quite difficult to determine optimal temperature distributions in tooling [29].

Warm hydroforming technology for lightweight materials is currently being developed to achieve reduced number of manufacturing steps and part consolidation. It makes use of the improved formability at elevated temperature while using the tooling and hydraulic medium as means of transporting heat as well as mechanical/hydraulic force at relatively low levels, Figure 8.

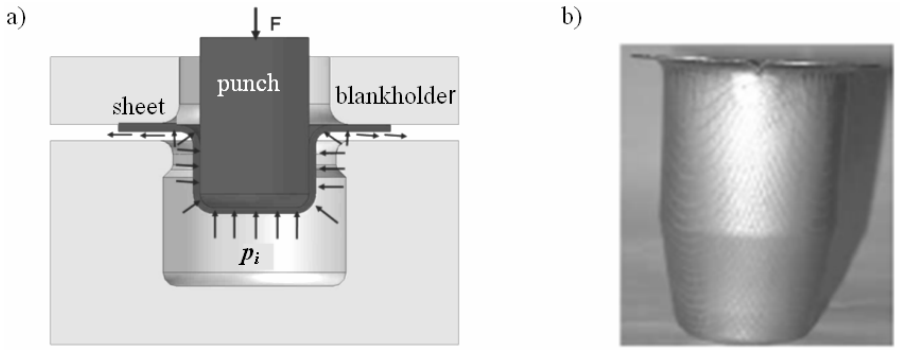

Fig. 7. Scheme of deep drawing by hydroforming (a) and example of product (b) [26]

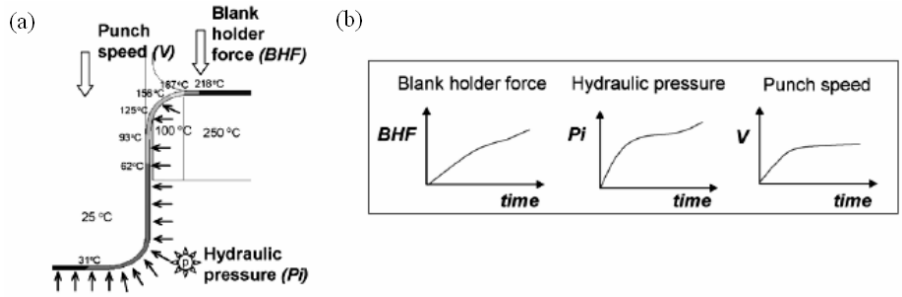

Fig. 8. An example of loading profiles: (a) – controllable variables (blank holder force, hydraulic pressure and punch speed), (b) – temporal control of loading profiles [30]

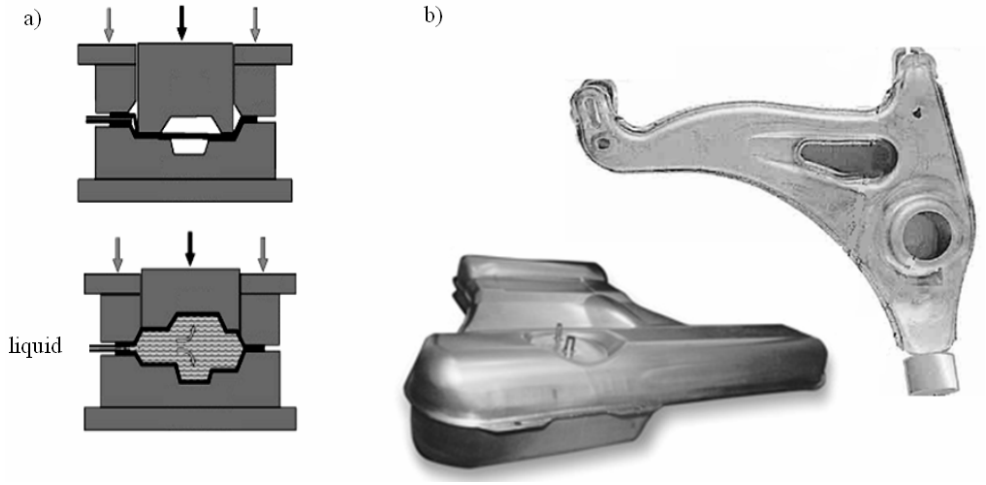

Fig. 9. Scheme of the hydroforming of metal pairs (a) [26]
and industrial examples of hydroformed metal pairs (b) [31–32]

A special case of sheet hydroforming is the hydroforming of welded-closing sheet metal pairs. Figure 9a shows the scheme of the process whereas Figure 9b shows industrial examples. The hydroforming technology of sheet metal pairs was developed some years ago [5, 26] but the number of applications in automotive industry increased especially in the last years. In the scheme (Figure 9a), the periphery of the sheet metal can be welded using laser welding. Then a liquid medium can be filled between the blanks, and pressurization can be effected by a hydraulic system. It is very difficult to realize radial feeding using this method, as it is essentially a pure bulging deformation. To some extent, this technology is similar to tube hydroforming.

3. Tube hydroforming

Grey et al. in 1939 [33] formed a T-joint using a seamless copper tube and applied for and achieved a US patent in the 1940s, which gave an indication of the coming period of tube hydroforming. Until now, the forming of T-shape used for a joint is still a problem in hydroforming. Figure 1 shows one of the schemes of tube hydroforming.

When using seamless tube or welded tube, the blank can be formed into the shape of the die cavity by internal pressure and when the side punches move in. Tube hydroforming has many advantages such as part consolidation, weight reduction, improved part strength and stiffness, highly accurate dimensions and low springback, lower tooling cost and fewer integrated processes, etc. which all promote rapid spreading of this technology in the automotive, household and aerospace industries [2, 34]. Welded tube blanks can be subjected to an internal pressure as high as 300 MPa, but exceptionally a pressure of up to approximately 700 MPa can be used [34–36].

Common semi finished products used for initial workpieces are longitudinally welded tubes made of conventional steel like unalloyed and stainless steel, and in some cases of aluminium alloys [37–38]. Today, steel suppliers offer new steel grades, e.g. high strength steels [39–40], competing with aluminium as new materials for lightweight constructions combined with hydroforming.

One of the leading automotive companies using hydroforming is BMW [41]. In the newest models of BMW (e.g. BMW M3) hydroformed exhaust components are used (Figure 10). New technology of tube hydroforming has become so profitable from many points of view, that other car producers have introduced new components into cars, as for example Audi (Figure 11).

There exists a considerable interest to reduce vehicle weight through the adoption of lightweight materials, such as aluminium alloys, while maintaining energy absorption and component integrity under crash conditions. The interaction between tube hydroforming and behaviour during crash events was studied using lightweight automotive structural members [43]. There was used a high-pressure hydroforming process in which tubes with various corner radii in the tube cross-section were produced, Figure 12. Next the tubes were subjected to axial upsetting.

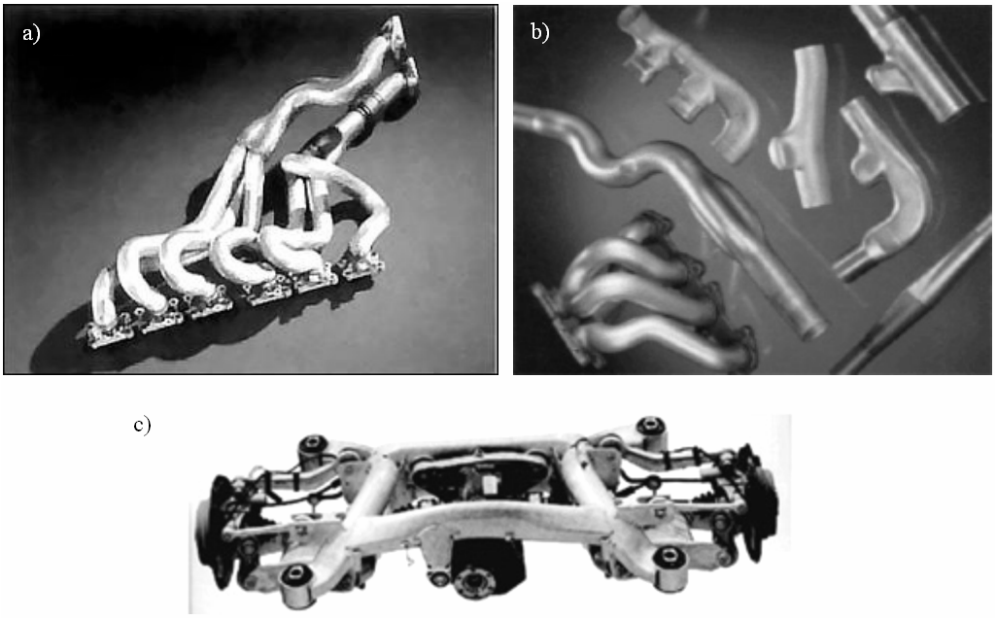

Fig. 10. Exhaust system of BMW M3 (a) and its elements formed by hydroforming (b) as well as BMW rear axles with hydroformed components (c) [42]

Fig. 11. Audi TT Coupe with hydroformed rear axle components [42]

Fig. 12. Cross-section of non-hydroformed and hydroformed tubes [43]

The tubular hydroforming process can be used to produce a bumper stay, which secures the bumper beam to the vehicle body (see Figure 13b). When the automobile is hit from the front or behind, the bumper beam collapses and the impact force is transmitted to the left and right front frames, respectively, through the bumper beam and bumper stays. The impact energy is absorbed by plastic deformation of the bumper beam and bumper stays. The conventional bumper structure is assembled from several parts (Figure 13a), so several manufacturing processing steps are needed, and the structure is somewhat complex. Most research work on bumper stays has focused on using reinforcing members that have complicated shapes [44–45]. Hydroformed bumper stay (Figure 13c,d) is rather simple in the shape but its ability to absorb energy through plastic deformation is relatively high.

In most of the tube hydroforming processes, the decrease in wall thickness is prevented by compressing the tube in the axial direction simultaneously with the action of the internal pressure (see example in Figure 1). If the internal pressure is too small, the axial compression causes the wrinkling of the tube wall. Hence the paths of internal pressure and axial compression in the tube hydroforming are keys to prevent the occurrence of these defects. The finite element simulation has been employed to determine the pressure paths [16, 47–50]. A pulsating hydroforming process of tubes has been developed for the forming of hollow products with a complex shape [51]. An improvement of the formability by means of the pulsating hydroforming have been investigated [52–53] and simulated by the finite element method [52].

The deformation behavior of the tube in the hydroforming is greatly influenced by the friction at the interface between the tube and die [54]. Although the friction during forming is reduced by ultrasonic vibration of dies [55], the friction in the pulsating hydroforming has been hardly decreased by the oscillation of internal pressure [56]. In the pulsating hydroforming, the local thinning is prevented by the uniform expansion, and thus the formability is improved. Figure 14 shows the difference between shape of free bulged tube with constant and pulsating pressure. The tube is uniformly expanded by repeating the appearance and disappearance of the small wrinkling, and thus the local thinning is prevented. The pulsating hydroforming is attractive for the improvement of the formability of tubes.

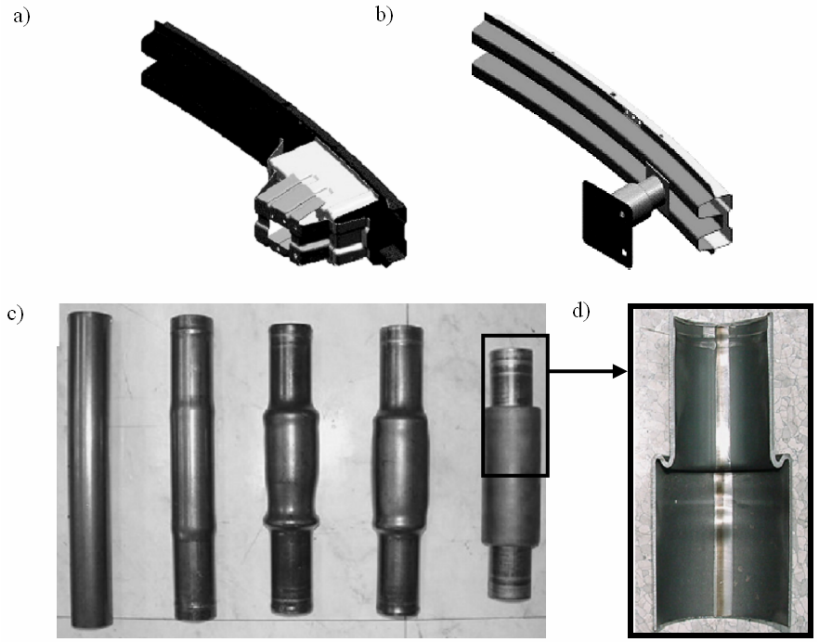

Fig. 13. A conventionally produced bumper stay (a), hydroformed bumper stay (b), bumper stay hydroforming process (c) with detailed shape of tube wall (d) [46]

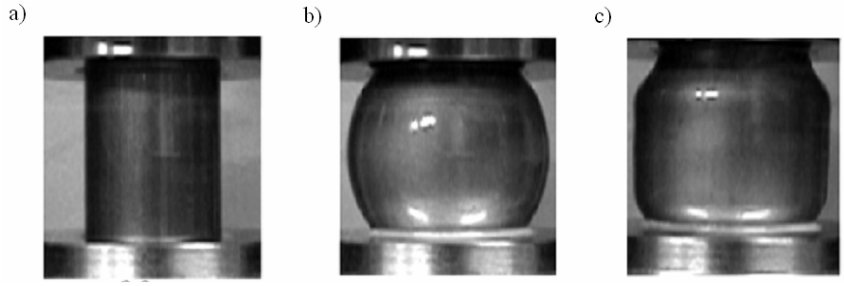

Fig. 14. Difference between constant and pulsating hydroforming: tube before forming (a), deforming shape of free bulging region for high constant pressure (b) and for pulsating pressure (c) [53]

Bellows are quite important group of products made by hydroforming of tubes, Figure 15. They are commonly used in piping systems to absorb expansion and mechanical movement and they have widespread applications in industrial and chemical plants, power systems, heat exchangers, and automotive vehicle parts [57]. Special stands for expanding the tube wall by internal pressure and axial compression of the tube in order to produce bellows were developed in Metal Forming Department at Warsaw University of Technology in 1960s. There were produced bellows with one and multi-layer walls [58–59].

Fig. 15. The hydroformed bellows [57, 58]

Fig. 16. An example of hole made by hydropiercing [60]

Cost-effectively produced, correctly positioned holes are essential, functional requirements in nearly all structural automotive components [60]. Holes can be cut into a part by drilling/milling, laser or plasma cutting, flow drilling, and punching in the die (hydropiercing), or post-piercing. Hydropiercing can produce various hole styles just in the primary process. Figure 16 shows an example hydropierced hole where a slug was pushed out from the cavity by internal pressure. Holes that cannot be hydropierced must be done in a secondary cutting or piercing operation at additional cost and reduced positional accuracy and repeatability.

4. Product development cycle

The development of hydroformed parts for series production necessitates efficient methods to meet the requirements of short development times, and high part quality with an optimized process chain. An important factor in achieving these short development lead times is the use of CAD, CAM and CAE techniques, including process simulations exploiting the potential of FEA [70]. This is particularly important as the spectrum of the hydroformed components increases continuously in quantity and complexity.

Finite element analysis (FEA) has been commonly used in numerical simulation of hydroforming. As exemplary for joints, mainly two models with shell [61–65] and solid elements [66–69] have been reported in most of the recent papers. It is rather difficult to say which model would be good enough for a specific application. Hence, a comparison of calculated results obtained by means of different numerical models could be very helpful in finding some indications for using those models.

Typical steps and phases of a product development cycle for a hydroformed component are illustrated in Figure 17. The basis of this cycle is the CAD model of the component. The first analysis of the component, e.g. the determination of cross-sectional circumferences, corner radii, bent mean axis [71] and the application of one-step simulations, gives a rough estimation as to whether the part can be manufactured by hydroforming or not. It gives also a first indication of forming loads such as internal pressure, axial forces and the force to close the die during the forming process.

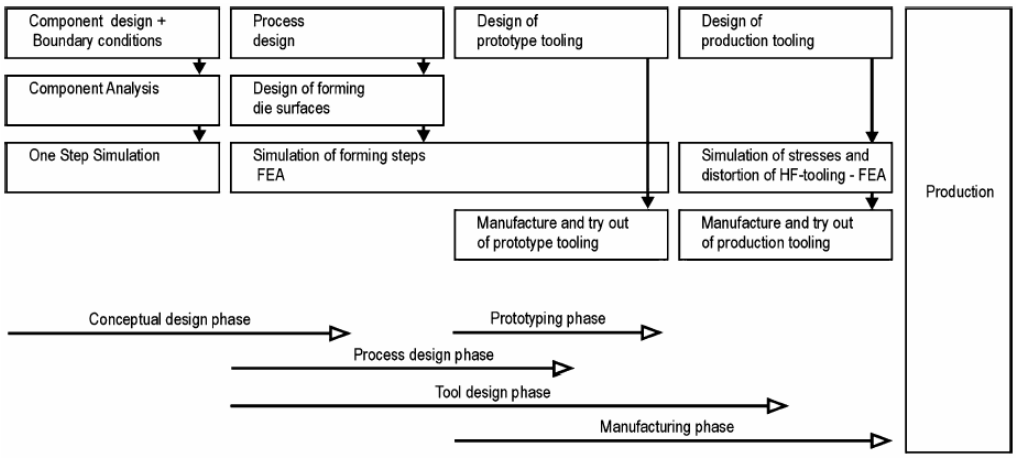

Fig. 17. Characteristic product development cycle for hydroformed components [70]

If the feasibility of the part is proven, and additional forming steps such as bending and pre-forming are determined, a more accurate simulation can be performed by finite element simulation methods. The forming die shape of the hydroforming die model is usually generated directly from the CAD-data, complete with the tool parting line and the end feed sections of the workpiece.

Even during the experimental prototyping phase, FEA is used to optimize the process design. Necessary modifications of the dies can also be investigated by "virtual manufacturing". This enables the saving of time and costs for the whole product development cycle. Successful prototyping showing the part's feasibility and process reliability is followed by the design, manufacture and try-out of the series production tooling. To ensure adequate tooling life time and a constant part quality, the FEA is used in this stage to determine the stresses and elastic deformation acting on the tool

elements due to the forming loads. In the context of the above described component and process design, the FEA is used:

- to check the production feasibility of the component,
- to analyze and optimize the final component quality and expected process reliability,
- to determine an indication of the required process forces for the die and machine design, e.g. [62].

The forming possibilities of the hydroforming process are crucial for product development. The tube model passes through the individual forming steps, so that the strains and stresses from each preceding step are considered [9]. For the tube model, four-node shell elements with complete integration over the shell thickness work satisfactorily. In practically all cases, the component curved surfaces are the most critical areas in the hydroforming process. Very good simulation results can be achieved by the detailed reproduction of the bending process. Final dimensions can be calculated with an accuracy variation of less than 2% by such coherent simulation.

There was also shown [9] the comparison of calculated component properties with the properties of the manufactured component for an aluminium rear axle component, manufactured by pre-forming and hydroforming. The forming limit curve (FLC) of the aluminium material was used to estimate the process feasibility with the FEA during the component and process design [73]. This was done on the assumption that the ratio of maximum to minimum strain is almost constant during the forming. Besides other boundary conditions, the choice of the friction law and friction coefficients is important for the accuracy of the simulation results. For most if the simulations, Coulomb's law of friction was used. A modified friction test, working with pressurized tubes, enables the determination of suitable values for the friction coefficient [72].

The optimisation of the hydroformed engine cradle geometry with the aid of FEA in the course of an experimental prototyping was presented in [74]. In this example the first execution of the pre-forming operation resulted in wrinkles on a bent area of the part. It was not possible to flatten those wrinkles with the internal pressure by the subsequent hydroforming operation. To remove this potential failure, different variants of pre-forming die shapes were investigated by FEA and the most suitable one was translated into the new die cavity. A saving of time and costs of about 70% was achieved with the aid of FEA in comparison to an experimental try-out.

Wide spreading of the HF has been limited by a kind of secrecy on knowledge bases and the lack of specific material specifications for incoming shapes and tubes. Hence, new component applications cause many problems that usually must be solved individually. Excellent example can be hydroformed X and T-joint. Hydroforming process feasibility of X-joint has been discussed in [75–76]. Experimental results of X-joint hydroforming have been compared with the results of extensive FEA simulations in order to find a method of failure prediction.

5. Concluding remarks

Sheet and tube hydroforming processes have been placed at the frontier of modern metal forming technologies. The future of the processes remains quite prospective due to the development of computer modeling but there have been some limitations on prediction of forming limits. As the industry has developed, it has become standard practice that hydroforming requires an intense focus on process simulation to predict as many difficulties as possible beforehand.

As comparing with conventional metal forming technologies, hydroforming is still quite new. Following the development of the relevant technologies, such as equipment design and manufacturing, automatic control systems or ultra pressure units, many different methods have been invented and hydroforming can be applied successfully in large volume production. The future of the hydroforming still remains quite exciting and prospective though a huge achievement has been obtained at this time mainly for tube hydroforming in the automotive industry. Once a break-through component is found in sheet hydroforming in some application fields, possible development will be even much faster.

References

[1] Chałupczak J.: *Application of hydroforming for making T-joints and X-joints* (in Polish), Scientific Papers of Technical University of Kielce, Mechanics, 41, 1988.
[2] Ahmetoglu M., Sutter K., Li X.J., Altan T.: *Tube hydroforming: current research*, Journal of Materials and Technology, 98, 2000, pp. 224–231.
[3] Kleiner M. et al.: *New 100.000 kN press for sheet metal hydroforming*, Proceedings of the International Conference on Hydroforming, Stuttgart, Germany, 6th/7th November, 2001, pp. 351–362.
[4] Geiger M.: *Neue Entwicklungen beim IHU von Blechen und deren Einsatzpotenziale für Leichtbauteile*, Proceedings of the Third Chemnitz Car Body Colloquium, Chemnitz, Germany, 25th/26th September, 2002, pp. 225–241.
[5] Novotny S., Hein P.: *Hydroforming of sheet metal pairs from aluminum alloys*, Proceedings of the SheMet'99, 9th September, 1999, pp. 591–598.
[6] Novotny S., Geiger M.: Process design for hydroforming of light weight metal sheets at elevated temperatures, Journal of Material Process and Technology, 138, 2003, pp. 594–599.
[7] Altan T.: *Formability and Design Issues in Tube Hydroforming*, Proceedings of the International Conference on Hydroforming, Stuttgart, Germany, 12th/13th October, 1999, pp. 135–151.
[8] Dohmann F., Hartl Ch.: *Hydroforming – a method to manufacture light-weight-parts*, Journal of Material Process and Technology, 60, 1996, pp. 669–676.
[9] Hartl Ch., Bauer H., Haas A.: *Optimierungserfolge durch Simulation in der Innenhochdruck-umformung*, EFB-Kolloquium Wirtschaftliche Blechumformung durch Simulation, Fellbach b. Stuttgart, Germany, March, 1999, pp. 9–10.

[10] Vollesten F. Sprenger A., Krauss J.: *Extrusion, channel, and profile bending: a review*, Journal of Materials and Technology, 87, 1990, pp. 1–27.
[11] Kelder M., Edgar K.: Hydroforming dual-phase steel, The Tube & Pipe Journal 7th December, 2004, pp. 53–57.
[12] Maki T., Walter C.: *Liquid curves – Sheet hydroforming helps the sporty Solstice stand out*, Stamping Journal, 8th May, 2007, pp. 32–37.
[13] Zhang S.H., Danckert J: *Development of hydro-mechanical deep drawing*, Journal of Materials Processing Technology, 83, 1998, pp.14–25.
[14] http://www.carpimoto.com/content/prod/l_EN/s_1_Home/pr_16884_Akrapovic_Complete_Racing_Hydroforming_Exhaust_System_Kawasaki_ZX_10R_04_05_full_titanium_Oval_muffler_with_titanium_sleeve.htm.
[15] Paulsen F., Welo T., Sovik O.P.: *A design method for rectangular hollow section in bending*, Journal of Materials and Technology, 113, 2001, pp. 699–705.
[16] Yang J.B., Jeon B.H., Oh S.I.: *Design sensitivity analysis and optimization of the hydroforming process*, Journal of Materials and Technology, 113, 2001, pp. 666–672.
[17] Asnafi N., Nilsson T., Lassl G.: *Tubular hydroforming of automotive side members with extruded aluminum profiles*, Journal of Materials Processes Technology, 142, 2003, pp. 93–142.
[18] Carpenter J.A.: *The Freedom CAR Challenge and Steel*, American Iron and Steel Institute, Great Designs in Steel Seminar, Livonia, MI, 2004, pp. 96–111.
[19] Schultz R.A.: *Aluminum for light vehicles – an objective look at the next ten to twenty years*, in: 14th Int'l Aluminum Conference, Montreal, Canada (Ducker Research), 15th September, 1999, pp. 243–250.
[20] Mildenberger U., Khare A.: *Planning for an environment-friendly car*, Technovation, 20, 2000, pp. 205–214.
[21] Choi Y., Yeo H.T., Park J.H., Oh G.H., Park S.W.: *A study on press forming of automotive sub-frame parts using extruded aluminum profile*, Journal of Materials Processing Technology, 187–188, 2007, pp. 85–88.
[22] Godwin J.: Materials World, Hydroforming Techniques, Vol. 6, No. 8, 1998, pp. 483–84.
[23] Hartl Ch.: *Research and advances in fundamentals and industrial applications of hydroforming*, Journal of Materials Processing Technology, 167, 2005, pp. 383–392.
[24] USS – materials available in http://ussautomotive.com/auto/steelvsal/alintensive.htm.
[25] Vollertsen F., Prange T., Sander M.: *Hydroforming: needs, developments and perspectives*, Proceedings of the Sixth International Conference on Technology Plasticity, Advanced Technology of Plasticity, Vol. 6, Berlin, Germany, 1999, pp. 1197–1210.
[26] Kleiner M., Gartzke A., Kolleck R., Ramer J., Weidner T.: *Finite element simulation for high pressure sheet metal forming (HBU process) and tool construction*, Adv. Technol. Plast. 2, 1996, pp. 975–983.
[27] Li D., Ghosh A.: *Tensile deformation behavior of aluminum alloys at warm forming temperatures*, Mater. Sci. Eng. A, 352, 1–2, 2003, pp. 279–286.
[28] Naka T., Torikai G., R. Hino, F. Yoshida: *The effects of temperature and forming speed on the FLD for type5083 Al–Mg alloy sheet*, Journal of Materials and Technology, 113, 2001, pp. 648–653.
[29] Kim H.S., Koc M., Ni J.: *Determination of app.ropriate temperature distribution for warm forming of aluminum alloys*, Trans. NAMRC 32, 2004, pp. 573–580.

[30] Zhongqi Yu, Zhongqin Lin, Yixi Zhao: *Evaluation of fracture limit in automotive aluminum alloy sheet forming*, Materials and Design, 28, 2007, pp. 203–207.
[31] Vahl M., Hein P., Bobbert S.: *Hydroforming of sheet metal pairs for the production of hollow bodies*, 2000, available on http://www.edpsciences.org/articles/metal/pdf/(2000)/ 10/ p1255.pdf.
[32] Vollrath K.: Hydroforming gains ground in German, 2002, available on http://www.the fabricator.com/Hydroforming/Hydroforming_Article.cfm?ID=106.
[33] Grey J.E., Devereaux A.P., Parker W.N.: *Apparatus for making wrought metal T's*, US Patent 2, 203, 1939, pp. 868.
[34] Constantine B., Roth R., Clark J.P.: *Substituting tube-hydroformed parts for automotive stamping: an economic model*, J. Mat., 53, 8, 2001, pp. 33–38.
[35] Zimniak Z., Piela A.: *Finite element analysis of a tailored blanks stamping process*, Journal of Materials Processing Technology, 106, 2001, pp. 254–260.
[36] Kuvin B.F.: *Hydroformer evolves into complete source for prototype and short-run sheet*, Metalforming, 12, 2002, pp. 26–29.
[37] Luecke H.-U., Hartl Ch., Abbey T.: *Hydroforming, Proceedings of the International Conference on Sheet Metal*, Erlangen Nuremberg, Germany, 27th/28th, September, 1999, pp. 607–614.
[38] Leitermann W. et al.: *Innovative Forming Technologies for Space Frames*, Proceedings of the International Conference on Advanced Technology of Plasticity, Nuremberg, Germany, 19–24 September, 1999, pp. 1183–1188.
[39] Flehmig T., Schwarz S.: *Hydroforming complex hollow sections*, Steel Grips 1, 6, 2003, pp. 408–412.
[40] Kroef et al.: *Untersuchungen von Stahl und Bestimmung von Umformcharakteristiken fur hydraulische Umformprozesse*, Proceedings of the Third Chemnitz Car Body Colloquium, Chemnitz, Germany, September 25/26, 2002, pp. 69–80.
[41] http://nsm.eng.ohio-state.edu/THFModule1/html/app.lications.html.
[42] http://www.salzgitterhydroforming.de/westsachsen/crimmitschau/salzgitter/de/produkte / abgaskomponenten/bsp_kruemmer/.
[43] Williams B.W., Oliveira D.A., Simha C.H.M., Worswick M.J., Mayer R.: *Crashworthiness of straight section hydroformed aluminum tubes*, International Journal of Impact Engineering, 2007, pp. 1451–1464.
[44] Oyama M., Masuta N.: *Automotive bumper stay structure*, US Patent 5441319, 1995.
[45] Kariatsumari K., Kobe: *Car body energy absorber and bumper stay*, US Patent 6481690 B2, 2002.
[46] Sohn S.M., Kim B.J., Park K.S., Moon Y.H.: *Evaluation of the crash energy absorption of hydroformed bumper stays*, Journal of Materials Processing Technology, 187–188, 2007, pp. 283–286.
[47] Rimkus W., Bauer H., Mihsein M.J.A.: *Design of load-curves for hydroforming app.lications*, Journal of Materials Processing Technology, 108, 1, 2000, pp. 97–105.
[48] Fann K.-J., Hsiao P.-Y.: *Optimization of loading conditions for tube hydroforming*, Journal of Materials Processing Technology, 140, 1–3, 2003, pp. 520–524.
[49] Aue-U-Lan Y., Ngaile G., Altan T.: *Optimizing tube hydroforming using process simulation and experimental verification*, Journal of Materials Processing Technology, 146, 1, 2004, pp. 137–143.

[50] Imaninejad M., Subhash G., Loukus A.: *Loading path optimization of tube hydroforming process*, International Journal of Machine Tools and Manufacture, 45, 12–13, 2005, pp. 1504–1514.
[51] Yogo T., Ito M., Mizuno T.: *Digital master system of hammering hydroforming*, (in Japanese), Journal of the Japan Society for Technology of Plasticity, 45, 527, 2004, pp. 1022–1025.
[52] Mori K., Patwari A.U., Maki S.: *Improvement of formability by oscillation of internal pressure in pulsating hydroforming of tube*, Annals of the CIRP 53, 1, 2004, pp. 215–218.
[53] Mori K., Maeno T., Maki S.: *Mechanism of improvement of formability in pulsating hydroforming of tubes*, International Journal of Machine Tools & Manufacture, 47, 2007, pp. 978–984.
[54] Manabe K., Amino M.: *Effects of process parameters and material properties on deformation process in tube hydroforming*, Journal of Materials Processing Technology, 123, 2, 2002, pp. 285–291.
[55] Murakawa M., Jin M.: The utility of radially and ultrasonically vibrated dies in the wire drawing process, Journal of Materials Processing Technology, 113, 1–3, 2001, pp. 81–86.
[56] Mori K., Maeno T., Bakhshi-Jooybari M., Maki S.: *Measurement of friction force in free bulging pulsating hydroforming of tubes*, in: P.F. Bariani et al. (Ed.), Advanced Technology of Plasticity, Edizioni Progetto Padova, Padova, 2005, pp. 192–200.
[57] Kang H., Lee M. Y., Shon S. M., Moon Y. H.: *Forming various shapes of tubular bellows using a single-step hydroforming process*, Journal of Materials Processing Technology, 194, 2007, pp. 1–6.
[58] Erbel S., Kuczyński K.: *Metalforming of bellows part 1* (in Polish), Mechanik, Vol. 4, 1962, pp. 180–183.
[59] Erbel S., Kuczyński K.: *Metalforming of bellows part 2* (in Polish), Mechanik Vol. 5, 1962, pp. 281–285.
[60] Morphy G.: *Tube Hydroforming Design Flexibility—Part VII: Holes*, Exclusive to The Fabricator.com, February, 2005, available on http://www.thefabricator.com/ Hydroforming/ Hydroforming_Article.cfm?ID=1047.
[61] Hama T., Ohkubo T., Kurisu K., Fujimoto H., Takuda H.: *Formability of tube hydroforming under various loading paths*, Journal of Materials Processing Technology, 177, 2006, pp. 676–679.
[62] Jirathearanat S., Hartl Ch., Altan T.: *Hydroforming Y-shapes – product and process design using FEA simulation and experiments*, Journal of Materials and Technology, 146, 2004, pp. 124–129.
[63] Kim T.J., Yang D.Y., Han S.S.: *Numerical modelling of the multi-stage sheet pair hydroforming process*, Journal of Materials Processing Technology, 151, 2004, pp. 48–53.
[64] Plancak M., Vollertsen F., Woitschig J.: *Analysis, finite element simulation and experimental investigation of friction in tube hydroforming*, Journal of Materials Processing Technology, 170, 2005, pp. 220–228.
[65] Ray P., Mac Donald B.J.: *Determination of the optimal load path for tube hydroforming processes using a fuzzy load control algorithm and finite element analysis*, Finite Elements in Analysis and Design, 41, 2004, pp. 173–192.
[66] Aydemir, A., Vree, J.H.P., Brekelmans W.A.M., Geers M.G.D., Sillekens W.H., Werkhoven R.J.: *An adaptive simulation approach designed for tube hydroforming processes*, Journal of Materials Processing Technology, 159, 2005, pp. 303–310.

[67] Mac Donald B.J., Hashimi M.S.J.: *Finite element simulation of bulge forming of a cross-joint from tubular blank*, Journal of Materials Processing Technology, 103, 2000, pp. 333–342.
[68] Mac Donald B.J., Hashimi M.S.J.: *Tree-dimensional finite element simulation of bulge forming using a solid bulging medium*, Finite Element Analysis and Design, 37, 2001, pp. 107–116.
[69] Zadeh H.K., Mashhadi M.M.: *Finite element simulation and experimental in tube hydro-forming of unequal T shapes*, Journal of Materials Processing Technology, 177, 2006, pp. 303–310.
[70] Dohmann F., Hartl Ch.: *Hydroforming-applications of coherent FE Simulations to the development of product and processes*, Journal of Materials and Technology, 150, 2004, pp. 18–24.
[71] Hartl Ch.: *Theoretical fundamentals of hydroforming*, Proceedings of the International Conference on Hydroforming, Stuttgart, Germany, 12th/13th, October, 1999, pp. 28–37.
[72] Vollertsen F.: *Challenges and chances of hydroforming of aluminum alloys*, in: O. Hahn, X.-S. Yi (Eds.), Proceedings of the Chinese–German Ultralight Symposium, DVS-Berichte Band, Vol. 218, 2001, pp. 71–91.
[73] Bauer H., Hartl Ch., Haas A.: *Hydroforming-optimized process design with the aid of the FEA*, Proceedings of the Advanced Technology Symposium on Tube Hydroforming, Iron and Steel Society, Detroit, MI, USA, 20–22 June, 1999, pp. 98–105.
[74] Böhm A., Hartl Ch., Abbey T.: *Process and tool technology for hydroforming: case study and technical and economic considerations*, Proceedings of the International Conference on Tube Hydroforming, Columbus, USA, 13–14, June, 2000, pp. 123–128.
[75] Kocańda, A., Sadłowska, H.: *An approach to process limitations in hydroforming of X-joints as based on formability evaluation*, Journal of Materials Processing Tech, Volume: 177, Issue: 1–3, 3th July, 2006, pp. 663–667.
[76] Sadłowska H., Kocańda A.: *Comparison of numerical models for hydroforming of X-shapes*, Computer Methods in Materials Science, Vol. 7, No. 2, 2007, pp. 294–298.

Wykorzystanie kształtowania hydromechanicznego do rozwoju części samochodowych

Kształtowanie hydromechaniczne zaczęto coraz częściej stosować w ostatnich latach w związku z rosnącymi potrzebami obniżenia wagi różnych wyrobów w przemyśle lotniczym, kosmicznym i motoryzacyjnym. Jest to stosunkowo młoda technologia w porównaniu z walcowaniem, kuciem, czy tłoczeniem i stąd stosunkowo mało jest dostępnych danych niezbędnych do projektowania wyrobów i procesów. W porównaniu z klasycznymi procesami tłoczenia i spawania, kształtowanie hydromechaniczne rur (THF) i blach (SHF) przynosi wiele korzyści: zmniejszenie kosztu wyrobu, kosztu narzędzi, wagi wyrobu, poprawę stabilności konstrukcji, zwiększenie wytrzymałości i sztywności wyrobu, bardziej równomierny rozkład grubości, zmniejszenie ilości operacji dodatkowych, itd. W referacie zaprezentowano rozległe możliwości rozwoju produkcji wyrobów poprzez zastosowanie procesów kształtowania hydromechanicznego, ze szczególnym uwzględnieniem wyrobów dla przemysłu motoryzacyjnego. Podano także uwagi na temat komputerowego modelowania tych procesów i zjawisk ograniczających.

ARCHIVES OF CIVIL AND MECHANICAL ENGINEERING

Vol. VIII 2008 No. 3

Numerical modelling of flow through moving water-control gates by vortex method. Part I – problem formulation

S. W. KOSTECKI
Wrocław University of Technology, Wybrzeże Wyspiańskiego 25, 50-370 Wrocław, Poland

A vortex method for simulating a flat flow within moving complex boundaries is presented. Thanks to the use of Lagrange variables (the trajectories of vortex particles) to determine the evolution of vorticity and velocity fields the method offers the possibility of modelling high Reynolds number flows. A procedure for formulating boundary conditions for flows confined by a moving impervious boundary, consisting in the superposition of three velocity fields: the first originating from the vortex particles, the second being a potential field satisfying the no-through-flow boundary condition and the third one resulting from the fact that the vortex sheet is modelled along the impervious boundaries and satisfying the no-slip-flow condition, is described. The original derivation of a formula for vortex sheet intensity, based on the single layer potential theory and leading to the formulation a second-kind Fredholm equation for vortex sheet intensity, is presented. This paper is the first part of a work covering the theoretical foundations and general description of the vortex method algorithms and boundary conditions. An example illustrating the computation of the vorticity and velocity fields of the flow through a moving hydraulic gate will be provided in the second part of the work.

Keywords: *hydraulic gates, turbulence flow, vorticity, vortex method, moving boundary*

1. Introduction

One of the principal hydraulic engineering problems is the calculation of the velocity of the water flow through moving hydraulic gates. As the hydraulic gate moves, conditions conducive to boundary layer separation and considerable pressure fluctuations arise. The flow around the gate may become very unstable, producing a highly variable load and so vibrations.

Similar problems as above also occur for the flow through hydraulic machines (turbines), in off-shore drilling (e.g. the water flow around riser tubes transporting oil from the seabed to the surface) and in aerodynamics (during the turbulent flow over the wings and fuselage of airplanes and in the wind engineering of bridges and high buildings).

The flow around moving hydraulic gates has been the subject of several experimental studies in recent decades. Their primary aim was to identify the mechanism causing gate vibrations. Thang [15] and Billeter [4] carried out model studies of the flow under a vibrating lift gate and found that the instability of the single shear layer separating from the gate lip results in sharp fluctuations in the pressure acting on the gate's bottom and rear edge. The fluctuations are the most common cause of gate vi-

brations. Aydin et al. [1] carried out studies on a hydraulic model of the gate as it was moving in a pressure conduit to determine the hydrodynamic force averaged over time.

The solution of the above problem is beset with numerous difficulties due to the high Reynolds number (usually exceeding 10^5) and the geometric complexity of the boundary, which may move or deform under the action of the liquid and this motion, in turn, affects the flow. For this reason, an analytical solution cannot be obtained, except for very simple cases of flow.

This paper presents a numerical method of computing the velocity and vorticity within a flow region bounded by a moving boundary with boundary velocity-liquid velocity consistency conditions imposed on it. In order to determine the dynamics of the liquid in such a region one must solve the Navier-Stokes equation (fully combined with the boundary elastic deformation equation) in three-dimensional space. The solution of the problem simplified to a flat flow with a moving inelastic boundary, constituting the first significant step towards the full problem solution, is derived here. The method will be extended to deformable boundary and three-dimensional problems in later work.

The discrete vortex method in a stochastic formulation, which is effective for high turbulence flows, is applied to solve the flow problem.

The vortex method formulation is based on vorticity field discretization into a finite number of particles (vorticity carriers) and the description of their motion in the Lagrangian coordinates. The problem solution consists in tracking the evolution of the particles (their position and intensity), resulting from advection, and simulating vorticity diffusion by the stochastic (random walk) method. The flow velocity field is explicitly recovered from the vorticity distribution by means of the Biot-Savart integral. The boundary conditions for the flow problem, including the moving boundary condition, stem from the friction forces produced by viscosity and are expressed by the equality between the velocity of the moving boundary and that of the liquid contiguous to it.

2. Governing equations

The flow of an incompressible viscous liquid in region D confined by boundary S is described by the Navier-Stokes Equation (1), mass conservation Equation (2) Dirichlet boundary condition (3) and initial condition (4):

$$\frac{\partial \mathbf{u}}{\partial t} + \mathbf{u} \cdot (\nabla \mathbf{u}) = -\nabla P + \nu \nabla^2 \mathbf{u}, \quad \mathbf{x} = [x_1, x_2, x_3] \in D,\ t > 0, \tag{1}$$

$$\nabla \cdot \mathbf{u} = 0, \tag{2}$$

$$\mathbf{u} = \mathbf{U}_b,\ \mathbf{x} \in S, \tag{3}$$

$$\mathbf{u} = \mathbf{u_0} \text{ for } t = 0, \tag{4}$$

where:

$\mathbf{u} = [u_1, u_2, u_3]$ is a liquid velocity vector,

$\mathbf{U}_b$ – a boundary velocity vector,

$P = p/\rho$ – kinematic pressure,

ν – a kinematic viscosity coefficient,

∇^2 – the Laplace operator.

3. Discrete vortex method formulation

The vortex method is formulated by reducing flow problem (1–4) to the vorticity transport problem acting with rotation operator on the Navier-Stokes equation whereby one gets the following system of equations:

$$\frac{\partial \boldsymbol{\omega}}{\partial t} + \mathbf{u} \cdot \nabla \boldsymbol{\omega} - \boldsymbol{\omega} \cdot \nabla \mathbf{u} - \nu \nabla^2 \boldsymbol{\omega} = 0, \qquad \mathbf{x} = [x_1, x_2, x_3], \qquad t > 0, \tag{5}$$

$$\nabla \cdot \mathbf{u} = 0 \tag{6}$$

$$\boldsymbol{\omega}\big|_{t=0} = \boldsymbol{\omega}_0. \tag{7}$$

The first of which (called the Helmholtz equation) expresses vorticity transport in terms of velocity $\mathbf{u} = [u_1, u_2, u_3]$ and vorticity $\boldsymbol{\omega} = [\omega_1, \omega_2, \omega_3]$, the second one represents the mass conservation law and the third one is the initial condition. The above relations do not contain any description of the boundary condition corresponding to Equation (3). This is due to the fact that the vorticity on the boundary is unknown. The way in which this boundary condition can be satisfied will be described in the next section.

Vorticity $\boldsymbol{\omega}$ is interrelated with the velocity vector as follows:

$$\boldsymbol{\omega} = \nabla \times \mathbf{u}, \tag{8}$$

$$\nabla \times \boldsymbol{\omega} = \nabla \times (\nabla \times \mathbf{u}) = \nabla (\nabla \cdot \mathbf{u}) - \nabla^2 \mathbf{u} = -\nabla^2 \mathbf{u} \tag{9}$$

It follows from (8) that the vorticity field has zero divergence $\nabla \cdot \boldsymbol{\omega} = \nabla \cdot (\nabla \times \mathbf{u}) \equiv 0$.

Throughout the paper we are interested in flat flows only. Therefore we assume that $\mathbf{u}(x_1, x_2, x_3) = \mathbf{u}(x_1, x_2), \mathbf{u}[u_1, u_2, 0]$ and $\boldsymbol{\omega} = [0, 0, \omega]$. Moreover, we can confine our considerations to the plane $x_3 = 0$ and take $\mathbf{x} = (x_1, x_2)$. For flat flows the vorticity

vector $\boldsymbol{\omega} = [0, 0, u_{2;x_1} - u_{1;x_2}]$ is orthogonal to **u** and the vorticity-stretching term vanishes in (5), $\boldsymbol{\omega} \cdot \nabla \mathbf{u} = 0$. To simplify notation we denote the velocity field by $\mathbf{u} = [u_1, u_2]$ and the scalar vorticity $\omega = u_{2;x_1} - u_{1;x_2}$.

In these settings the relation (9) takes the form

$$-\nabla^2 \mathbf{u} = \left[\omega_{x_2}, -\omega_{x_1}\right], \tag{10}$$

and its solution can be obtained by applying the generalized Biot-Savart law, which gives:

$$\mathbf{u}(\mathbf{x}, t) = \mathbf{K}(\mathbf{x}) * \omega(\mathbf{x}, t), \tag{11}$$

where "*" denotes the convolution operation. From the definition of convolution one gets the following integral form of the velocity field equation:

$$\mathbf{u}(\mathbf{x}, t) = \int_{\Re^3} \mathbf{K}(x - x')\omega(x', t)dx', \qquad x \in \Re^2. \tag{12}$$

For the flat flow problem, kernel **K** of integral (12) is the following vector function:

$$\mathbf{K}(\mathbf{x}) = \left(-\frac{x_2}{2\pi |\mathbf{x}|^2}, \frac{x_1}{2\pi |\mathbf{x}|^2} \right). \tag{13}$$

Velocity field (12) locally has an infinite value of kinetic energy $E_k(r)$, which follows from the singularity of kernel **K**(**x**)

$$\begin{aligned} &E_k(r) = \int_{r \le \rho} |\mathbf{u}|^2 dr = \infty, \textit{ for every } \rho > 0, \\ &r = |x|, \qquad x \in \Re^2 \end{aligned} \tag{14}$$

The kinetic energy of a physical velocity field is always finite. In order to avoid an error in the approximation of the velocity and vorticity fields **K**(**x**) should be replaced by a mollified kernel bounded in point **x** = 0. Mollified kernel $\mathbf{K}_\varepsilon(\mathbf{x})$ is obtained through regularization consisting in its convolution with a mollifying function:

$$\mathbf{K}_\varepsilon(\mathbf{x}) = f_\varepsilon(\mathbf{x}) * \mathbf{K}(\mathbf{x}). \tag{15}$$

Function f_ε is a properly selected mollified function which has this general form:

$$f_\varepsilon(\mathbf{x}) = \varepsilon^{-2} \cdot f\left(\varepsilon^{-1}\mathbf{x}\right), \qquad \varepsilon > 0, \tag{16}$$

where f is called a cut function. The function is axially symmetric and must fulfill specific conditions to ensure the convergence of the vortex method [10], [11], but first of all it must approximate δ – Dirac distribution when a cut radius $\varepsilon \to 0$:

$$\int_{\Re^2} f_\varepsilon(\mathbf{x})dx = 1, \qquad x \in \Re^2. \tag{17}$$

In the literature one can find several different forms of the mollifying function depending on the expected order of method convergence. The functions are based on a combination of exponential functions [2], [3], [6], [11], polynomials [6] and Bessel functions [10] or use hyperbolic functions [9]. Here the following Cauchy function was adopted [14]:

$$f(\mathbf{x}) = \frac{1}{\pi}\left(1+|\mathbf{x}|^2\right)^{-2} \text{ and } f_\varepsilon(\mathbf{x}) = \frac{1}{\pi\varepsilon^2}\left(1+\left|\frac{\mathbf{x}}{\varepsilon}\right|^2\right)^{-2}. \tag{18}$$

In the vortex method, the motion of liquid particles (vorticity carriers) is analyzed. As a result of kernel mollification procedure (15) the vortex particles have a limited support and form a vortex blob. If the liquid velocity field is properly smooth, then the blob trajectory equation has this form:

$$\frac{d\mathbf{X}^\varepsilon(\boldsymbol{\alpha},t)}{dt} = \mathbf{u}\left(\mathbf{X}^\varepsilon(\boldsymbol{\alpha},t),t\right), \qquad \mathbf{X}^\varepsilon(\boldsymbol{\alpha},t)\big|_{t=0} = \boldsymbol{\alpha} \tag{19}$$

where $\boldsymbol{\alpha} = [\alpha_1, \alpha_2]$ is the initial position of blobs.

In order to calculate the velocity from Equation (12) one needs to know the vorticity field. Vorticity is determined from the system of Equations (5–7). The viscous liquid flow problem is usually solved by assuming that liquid particles (vorticity carriers) move along trajectories determined from the Euler equation and perform chaotic Brownian motions as a result of diffusion. For this purpose, Helmholtz Equation (5) is decomposed and it is assumed that in the same time step vorticity field evolution is subject first to advection and then this field is modified in the process of diffusion. This procedure was proposed by Chorin [5] and is known as random walk. The vortex method with the random walk mechanism is often referred to as the stochastic or random vortex method.

When decomposition (known as the splitting method) is applied to the transport Equation, one gets a system of two Equations. The first one – Euler Equation (20) – describes vorticity advection while the second one (21) describes vorticity diffusion:

$$\frac{\partial \omega}{\partial t} + \mathbf{u} \cdot \nabla \omega = \frac{D\omega}{Dt} = 0, \qquad \mathbf{x} = [x_1, x_2], \qquad t > 0, \tag{20}$$

$$\frac{\partial \omega}{\partial t} = \nu \nabla^2 \omega . \tag{21}$$

From relation (20) one can infer that the vorticity of blobs is preserved during their motion along trajectories:

$$\omega\left(\mathbf{X}^{\varepsilon}(\boldsymbol{\alpha}, t), t\right) = \omega_0(\boldsymbol{\alpha}) . \tag{22}$$

Relation (20) indicates that vorticity propagates through the motion of the viscous liquid. Let us substitute trajectory Equation (19) for the velocity vector in (12). Then instead of integrating over the whole space one should integrate along the particle trajectories, i.e. $\mathbf{x}' = \mathbf{X}^{\varepsilon}(\boldsymbol{\alpha}', t)$, since the vorticity values on them are known. For an incompressible liquid the Jacobian of this transformation is equal to unity [12].

Taking into account relation (15) one gets the following integral-differential Equation describing vortex blob trajectories:

$$\begin{aligned} &\frac{d\mathbf{X}^{\varepsilon}(\boldsymbol{\alpha}, t)}{dt} = \int_{\Re^2} \mathbf{K}_{\varepsilon}(\mathbf{X}^{\varepsilon}(\boldsymbol{\alpha}, t) - \mathbf{X}^{\varepsilon}(\boldsymbol{\alpha}', t))\omega_0(\boldsymbol{\alpha}')\, d\boldsymbol{\alpha}', \\ &\mathbf{X}^{\varepsilon}(\boldsymbol{\alpha}, t)\big|_{t=0} = \boldsymbol{\alpha}, \qquad x \in \Re^2. \end{aligned} \tag{23}$$

The solution of Equation (23) allows one to investigate the motion of vortex blobs and on this basis to determine the vorticity field and the velocity field.

Vortex blobs are obtained by discretizing the continuous vorticity field. This can be done by imposing space lattice $\Lambda^h = \left\{\boldsymbol{\alpha}_i : \boldsymbol{\alpha}_i = h \cdot i = h \cdot (i_1, i_2), i \in Z^2\right\}$ on the computation area, where Z is a set of integers forming a grid of squares with side $h > 0$. Vortex particles with a circulation corresponding to the product of the grid mesh area and the vorticity value in the middle of this mesh are placed in the grid nodes. The vortex blob circulation determined from the integral of the square area is given by this formula:

$$\Gamma_{0i} = \omega_{0i}(\boldsymbol{\alpha}_i) h^2, \qquad \boldsymbol{\alpha}_i \in \Lambda^h \tag{24}$$

In this way, after vorticity discretization and approximation by the regularization procedure, the problem of vorticity transport in the flat flow reduces itself to a system of ordinary differential Equations whose unknowns are vortex blob trajectories:

$$\begin{aligned}
&\frac{d\mathbf{X}_i^{\varepsilon h}(t)}{dt} = \sum_{j\in Z^2} \mathbf{K}_\varepsilon\left(\mathbf{X}^{\varepsilon h}(\boldsymbol{\alpha}_i,t) - \mathbf{X}^{\varepsilon h}(\boldsymbol{\alpha}_j,t)\right)\omega_{0j}(\boldsymbol{\alpha}_j)h^2 \\
&= \sum_{j\in Z^2} \mathbf{K}_\varepsilon\left(\mathbf{X}_i^{\varepsilon h}(t) - \mathbf{X}_j^{\varepsilon h}(t)\right)\Gamma_{0j}, \qquad (25)\\
&\mathbf{X}^{\varepsilon h}(\boldsymbol{\alpha}_i,t)\big|_{t=0} = \boldsymbol{\alpha}_i, \qquad i\in Z^2, \qquad \boldsymbol{\alpha}_i \in \Lambda^h
\end{aligned}$$

where $\mathbf{X}^{\varepsilon h}(\boldsymbol{\alpha}_i, t) = \mathbf{X}_i^{\varepsilon h}(t)$ blob trajectories approximated by the mollification procedure.

The system can be approximately solved by any method, e.g. by the explicit Euler method in which the vorticity field evolution, expressed by the displacement of vortex blobs, is determined according to the step-by-step scheme:

$$\widehat{\mathbf{X}}_i^{\varepsilon h}(t+\Delta t) = \mathbf{X}_i^{\varepsilon h}(t) + \Delta t\,\mathbf{u}_i^{\varepsilon h}(t), \qquad (26)$$

where: $\mathbf{u}_i^{\varepsilon h}(t) = \sum_{j\in Z^2} \mathbf{K}_\varepsilon\left(\mathbf{X}_i^{\varepsilon h}(t) - \mathbf{X}_j^{\varepsilon h}(t)\right)\Gamma_{0j}$.

If a more accurate procedure of integration over time, e.g. the Runge-Kutta method, is used, more accurate vortex displacements in time and so better approximations of the vorticity and velocity fields will be obtained.

Equation (26) is the solution of the first calculation stage which resulted from the decomposition of the incompressible inviscid liquid flow problem represented by Euler Equation (20). In the second stage, Equation (21) representing vorticity diffusion will be solved. The diffusion problem in the random walk method consists in the probabilistic interpretation of the diffusion equation on the basis of the agreement between the diffusion equation solution and the description of the Brownian motions of particles (vorticity carriers). In each time step, the velocity field determined from the vorticity advection on the basis of Equations (25) and (26) is then modified in the diffusion process. The modification consists in assigning the displacement resulting from the Brownian motion to each vortex blob. In this way the position of blob $\mathbf{X}^{\varepsilon h}(t)$ changes by value $\boldsymbol{\eta}(t)=(\eta_1, \eta_2, t)$:

$$\mathbf{X}_i^{\varepsilon h}(t+\Delta t) = \widehat{\mathbf{X}}_i^{\varepsilon h}(t+\Delta t) + \boldsymbol{\eta}(t+\Delta t). \qquad (27)$$

Equation (27) is the solution of the vorticity transport problem described by the system of Equations (5–7), where $\boldsymbol{\eta}(t)$ is a two-dimensional random number which

comes from the normal Gaussian distribution with the expected value equal to zero and variance 2*tv*:

$$G_t(\mathbf{x},t)=\left(4\pi\nu t\right)^{-1} e^{-\frac{|\mathbf{x}|^2}{4t\nu}}=G_t(x_1,t)G_t(x_2,t)=\left(\frac{1}{\sqrt{4\pi t\nu}}e^{-\frac{x_1^2}{4t\nu}}\right)\left(\frac{1}{\sqrt{4\pi t\nu}}e^{-\frac{x_2^2}{4t\nu}}\right). \tag{28}$$

Since the variance depends on kinematic viscosity coefficient *v* (or Reynolds number Re for dimensionless variables), the influence of vorticity diffusion on the vortex particle (blob) motion trajectories will be smaller in a more turbulent flow.

The other sought vorticity and velocity fields are calculated from the relations:

$$\omega^{\varepsilon h}\left(\mathbf{x},t\right)=\sum_{j\in Z^2} f_\varepsilon\left(\mathbf{x}-\mathbf{X}_j^{\varepsilon h}\left(t\right)\right)\Gamma_{0j}, \tag{29}$$

$$\mathbf{u}^{\varepsilon h}\left(\mathbf{x},t\right)=\sum_{j\in Z^2} \mathbf{K}\left(\mathbf{x}-\mathbf{X}_j^{\varepsilon h}\left(t\right)\right)\Gamma_{0j}, \tag{30}$$

The distribution of the vortex stream function can be determined from the Poisson's equation:

$$\Delta\psi_\omega=-\omega. \tag{31}$$

Since $\psi_\omega=G*\omega$, where $G\left(x_1,x_2\right)=-\left(2\pi\right)^{-1}\ln|\mathbf{x}|$, $|\mathbf{x}|=\sqrt{x_1^{\,2}+x_2^{\,2}}$ is the fundamental solution of the Poisson's equation, one gets from (29) the following approximate vortex stream function distribution:

$$\psi^{\varepsilon h}\left(\mathbf{x},t\right)=\sum_{j\in Z^2} G_\varepsilon\left(\mathbf{x}-\mathbf{X}_j^{\varepsilon h}\left(t\right)\right)\Gamma_{0j}, \qquad G_\varepsilon\left(\mathbf{x}\right)=G\left(\mathbf{x}\right)*f_\varepsilon\left(\mathbf{x}\right) \tag{32}$$

4. Moving boundary and initial conditions

The vortex method equations were derived assuming that the flow takes place in the whole two-dimensional space (denoted by *D*) in which vortex points or blobs can move freely. In most engineering problems one deals with the problem of a boundary on which specific conditions must be fulfilled. In engineering calculation problems the flow is confined by a boundary in which the following parts can be distinguished: an inlet (usually with a prescribed velocity distribution), an outlet (with a prescribed direction of velocity vectors) and an impervious boundary. For the flow of a viscous liquid, the condition of no liquid slip along the impervious boundary is introduced into calculations. The boundary can be stationary or moving. In both cases, the velocity

component perpendicular to and the one tangent to the boundary must be consistent with the velocities of the boundary itself (in a special case of the stationary boundary, the velocity components are equal to zero).

4.1. Prescribed normal velocity

In the case of the flow described by the Euler equation, the boundary condition for an inviscid liquid is connected with the impermeability of the boundary whereby the velocity vector component normal to boundary S becomes zero:

$$\mathbf{u} \cdot \mathbf{n} = \mathbf{U}_b \cdot \mathbf{n}\big|_S \tag{33}$$

where:

$\mathbf{U}_b$ – the boundary velocity, which for a stationary boundary is equal to zero,

$\mathbf{n}$ is an external vector normal to the boundary.

In the vortex method this boundary problem is solved in two ways. One consists in creating images of vortexes with the same circulation, symmetrically to the boundary. Since vortex blobs have a compact support, which quickly decreases with the distance from the vortex centre, not all the vortexes must have their images outside the boundary, but only the ones which lie in the zone of influence. The width of the zone depends on the mollifying function and cut radius ε and it is usually enough to assume width 5ε [13]. Figure 2 shows a one-dimensional distribution of vorticity as a function of the vortex blob distance from the boundary, based on Equation (29), for $\varepsilon = 0.2$ and circulation $\Gamma = 1.0$. The blobs located at a distance greater than $x = 1$ have no effect on the vorticity value on the boundary. When the images of the blobs are introduced into the calculations, the liquid velocity vector becomes tangent to the boundary.

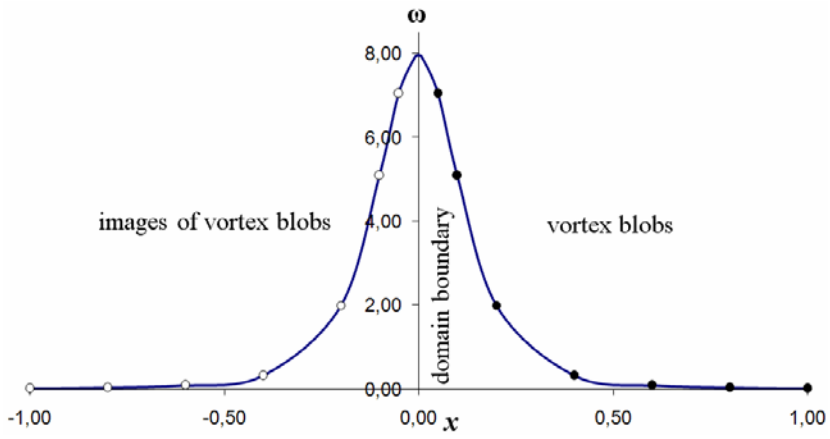

Fig. 1. Vorticity on boundary ($x = 0$) as function of distance of blobs and their images from boundary

The method performs well for simple and smooth boundaries. But when the flow region is irregular (as in the case of a conduit with a hydraulic gate), a proper conformal transformation procedure [6] is needed to determine the position of the vortex blob images since contiguous vortex blobs and their images may mutually interact in the bends of the boundary and the no-through-flow condition will not be fulfilled.

The other way to obtain a zero velocity component normal to the boundary is to determine an additional potential velocity field which when added to the vortex velocity field will make the velocity component normal to the boundary vanish. The additional field will have no effect on the vortex evolution solution, which can be proved using the Helmholtz principle of decomposition of velocity field **u** into two components:

$$\mathbf{u} = \mathbf{u}_\omega + \mathbf{u}_p, \qquad \mathbf{u} = \left[u_1, u_2\right] \tag{34}$$

where both components $\mathbf{u}_\omega$ and $\mathbf{u}_p$ are nondivergent and smooth and component $\mathbf{u}_p$ is additionally irrotational whereby it can be written in the two-dimensional gradient form:

$$\mathbf{u}_p = \nabla\varphi\,. \tag{35}$$

Acting with the divergence operator on Equation (34) one gets:

$$\nabla^2\varphi = 0\,, \tag{36}$$

where φ is a function of the velocity potential which obviously satisfies the Laplace equation. Then acting with the two-dimensional rotation operator on Equation (34) one gets:

$$\nabla\times\mathbf{u} = u_{2;x_1} - u_{1;x_2} = \nabla\times\mathbf{u}_\omega = \omega\,, \tag{37}$$

which means that potential velocity field $\mathbf{u}_p$ does not alter the vorticity in the region.

Since the value of normal component of potential derivative on the boundary is known:

$$\left.\frac{\partial\varphi}{\partial n}\right|_S = \mathbf{u}_p\cdot\mathbf{n} = \left(\mathbf{U}_b - \mathbf{u}_\omega\right)\cdot\mathbf{n}\Big|_S\,, \tag{38}$$

$\varphi(\mathbf{x})$ can be calculated from Equation (36) with Neumann boundary condition (38). Then potential velocity field $\mathbf{u}_p$ could be determined on the basis of (35). But then the

solution would be with accuracy to the additive constant. Therefore it is better to solve the potential flow problem, using potential stream function $\psi_p(\mathbf{x})$:

$$\nabla^2\psi_p(\mathbf{x},t)=0, \qquad \psi_p(\mathbf{x},t)\in D, \qquad t\geq 0, \qquad \mathbf{x}\in\Re^2. \tag{39}$$

On the part of the boundary with no through flow it is convenient to formulate a Dirichlet no-through-flow condition:

$$\psi_p(\mathbf{x},t)=\psi(\mathbf{x},t)-\psi_\omega(\mathbf{x},t), \qquad \mathbf{x}\in S, \tag{40}$$

where the approximate value of vortex stream function $\psi_\omega(\mathbf{x}, t)$:, for a specified time is given by relation (32). The value of stream function $\psi(\mathbf{x})$ on the solid boundary is constant and it stems from the physical interpretation of the difference between two streamlines, which is equal to the volume flow rate between the streamlines:

$$Q(\overset{\frown}{AB})=\psi(B)-\psi(A)=\int_{\overset{\frown}{AB}}\hat{\mathbf{u}}\cdot\mathbf{n}\,dS, \quad A,B\in S, \tag{41}$$

$\hat{\mathbf{u}}$ is the vector of the velocity of the flow through the part of the boundary between points A and B, constituting the inlet. In flow engineering problems the outlet is the boundary part for which a Neumann condition can be assumed:

$$\frac{\partial\psi_p(\mathbf{x},t)}{\partial n}=0, \qquad \mathbf{x}\in S. \tag{42}$$

The way in which $\psi(\mathbf{x})$ is assumed for the particular segments of the boundary is shown in Figure 2.

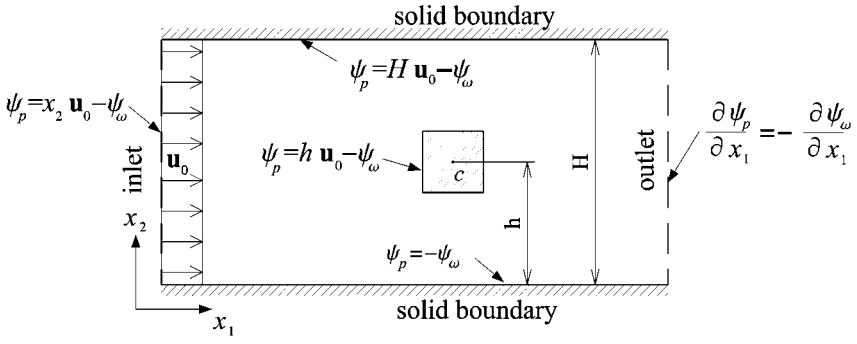

Fig. 2. Assumption of boundary condition for potential stream function

Problem (39)–(42) was solved here using Green's identity and the boundary element method [8]:

$$c(\xi)\psi_p(\xi,t)=\int_S \frac{\partial}{\partial n_x}G(\xi-\mathbf{x})\psi_p(\mathbf{x},t)d\mathbf{x}+\int_S G(\xi-\mathbf{x})\frac{\partial}{\partial n_x}\psi_p(\mathbf{x},t)d\mathbf{x}, \quad \xi,\mathbf{x}\in S, \tag{43}$$

where $G(\mathbf{x})=-(2\pi)^{-1}\ln|\mathbf{x}|$ and $c(\xi)$ is a coefficient dependent on the boundary's smoothness.

Therefore the solution by the vortex method will be the sum of solutions in interval $(t, t+\Delta t)$:

- at instant t auxiliary smooth velocity field $\mathbf{u}_\omega$ definite in the whole plane is generated on the basis of the location of vortex blobs,
- at instant $t+\Delta t$ gradient field $\mathbf{u}_p=\nabla\times\psi_p$ is added to the above field so that the resultant velocity field satisfies boundary condition (33).

Consequently, the trajectories of vortexes are obtained in form (44), which should be taken into account in relations (29), (30) and (32)

$$\hat{\mathbf{X}}_i^{\varepsilon h}(t+\Delta t)=\mathbf{X}_i^{\varepsilon h}(t)+\Delta t\left(\mathbf{u}_{\omega i}(t)+\mathbf{u}_{pi}(t)\right)+\boldsymbol{\eta}_i(t), \tag{44}$$

where $\mathbf{u}_{\omega i}$ and $\mathbf{u}_{pi}$ are respectively the vortex velocity component and the potential velocity component of the i-th vortex blob and $\boldsymbol{\eta}_i=(\eta_1,\eta_2)_i$ is the blob displacement due to diffusion.

4.2. Prescribed tangential velocity

The agreement between the normal velocity of the liquid and that of the boundary, described in the previous section is a condition sufficient for solving the problem of the flow of an inviscid liquid which moves at a specified tangent velocity along solid boundaries. In the case of the flow of a viscous liquid, friction forces are generated between the liquid and the wall whereby there is no slip between the liquid and the boundary. Thus the no-slip condition consists in agreement between the velocity of the boundary and that of the liquid in the direction tangent to the boundary and it can be expressed by the relation:

$$\left(\mathbf{u}_\omega(\mathbf{x},t)+\mathbf{u}_p(\mathbf{x},t)-\mathbf{U}_b(\mathbf{x},t)\right)\cdot\mathbf{s}=0, \qquad \mathbf{x}\in S, \tag{45}$$

where $\mathbf{s}$ is the vector tangent to boundary S.

In the splitting method the tangent component is made to vanish through a condition stemming from the physics of the formation of vorticity along the boundary. Physically, vorticity is as a result of the torque imparted to the particles when an adhe-

sion force originating from the boundary and a friction force originating from the particles flowing by (constituting the main flow-around stream) act on them. This mechanism is responsible for the formation of a vortex sheet along the boundaries, which with time carries vorticity into the region according to the course of the advection-diffusion phenomenon.

Mathematically the no-slip condition can be defined as a Dirichlet type condition by modeling the formation of a vortex sheet on the solid boundary. The forming sheet is then approximated with vortex blobs with a specific circulation. The velocity field produced by the blobs makes the liquid velocity component tangent to the boundary disappear. The original author of such a vorticity generation model was Chorin [5]. He proposed to discretize the boundary with segments with a specified length. In his method, vortex particles with their circulation corresponding to the product of the jump in tangent velocity (the difference in velocity between the boundary and the liquid) and the length of given boundary segment ds_i are assumed to exist in the centre of the segments:

$$d\Gamma_i = [\mathbf{u}](\mathbf{x},t)ds_i, \qquad [\mathbf{u}] = \mathbf{u}_\omega + \mathbf{u}_p - \mathbf{U}_b. \tag{46}$$

The particles generated in this way are subject to advection and diffusion in accordance with Equation (44).

In order to accurately determine the vorticity generated by the flow of a viscous liquid let us consider layer $\gamma(\mathbf{x}, t)$ contiguous to a smooth impermeable boundary. The relation between the vortex field circulation and the intensity of the layer is expressed as follows:

$$d\Gamma_i = \gamma(\mathbf{x},t)ds_i, \tag{47}$$

where: $\gamma(\mathbf{x}, t)$ – the intensity of the vortex sheet, which, according to Figure 3, can be defined as $\gamma(\mathbf{x},t) = \lim_{dx_2 \to 0} \omega(\mathbf{x},t) \cdot dx_2$.

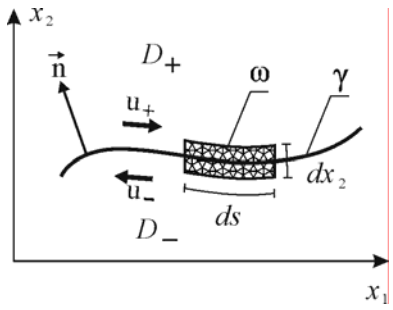

Fig. 3. Definition of vortex sheet intensity

Thanks to the existence of the vortex sheet, the stream function in the flow region is continuous and satisfies the Laplace equation. Hence to describe it one can use the single layer potential theory:

$$\psi(\boldsymbol{\xi}) = \int_S \sigma(\mathbf{x}) G(\mathbf{x},\boldsymbol{\xi}) dS(\mathbf{x}), \qquad \mathbf{x} \in S, \quad \boldsymbol{\xi} \in D/S, \tag{48}$$

where source density function $\sigma(\mathbf{x})$ is defined as the intensity of vortex sheet $\gamma(\mathbf{x})$. Determining stream function derivative (48) in the direction normal to the layer one gets:

$$\frac{\partial \psi(\boldsymbol{\xi})}{\partial \mathbf{n}_{\boldsymbol{\xi}}} = \int_S \gamma(\mathbf{x}) \frac{\partial G(\mathbf{x}-\boldsymbol{\xi})}{\partial \mathbf{n}_{\boldsymbol{\xi}}} dS(\mathbf{x}), \qquad \mathbf{x} \in S, \quad \boldsymbol{\xi} \in D/S. \tag{49}$$

Shifting point ξ from domain to the layer, i.e.$\xi \to \xi_0 \in S$ one gets the Fredholm equation of the second kind:

$$\frac{\partial \psi(\boldsymbol{\xi}_0)}{\partial \mathbf{n}_{\boldsymbol{\xi}_0}} = \pm \frac{1}{2} \gamma(\boldsymbol{\xi}_0) + \int_S \gamma(\mathbf{x}) \frac{\partial G(\mathbf{x}-\boldsymbol{\xi}_0)}{\partial \mathbf{n}_{\boldsymbol{\xi}_0}} dS(\mathbf{x}), \qquad \mathbf{x}, \boldsymbol{\xi}_0 \in S. \tag{50}$$

The sign in front of the first term on the right side of Equation (50) depends on the direction of the vector normal to the vortex sheet. One can assume that if $\mathbf{n}_{\xi_0}$ is directed outside the boundary, then for the external flow one can use the negative sign and for the internal flow, the positive sign, as shown in Figure 4.

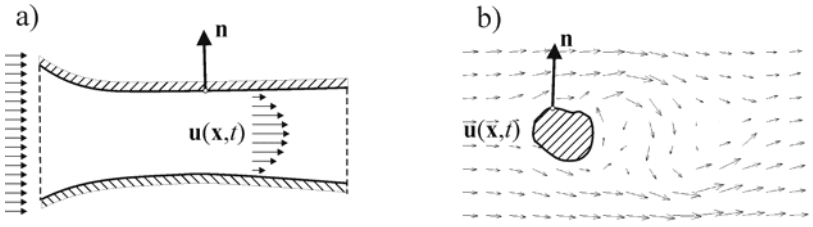

Fig. 4. Example of a) internal flow, b) external flow

The stream function derivative normal to the boundary is equal to the velocity tangent to the boundary. According to Equation (45) the tangent velocity value results from the superposition of the velocity field potential and vortex components and the boundary displacement velocity.

Taking into account the form of Green function $G(\mathbf{x}) = -(2\pi)^{-1} \ln|\mathbf{x}|$, the sought vortex sheet intensity value is given by the relation:

$$\pm\gamma(\xi_0) = -2\left(\mathbf{u}_\omega + \mathbf{u}_p - \mathbf{U}_b\right)(\xi_0)\cdot\mathbf{s}(\xi_0) + \frac{1}{\pi}\int_S \gamma(\mathbf{x})\frac{\partial \ln|\mathbf{x}-\xi_0|}{\partial \mathbf{n}_{\xi_0}}dS(\mathbf{x}), \qquad \mathbf{x},\xi_0 \in S, \quad (51)$$

where $\mathbf{s}(\xi_0)$ is a vector tangent to the boundary at point ξ_0. The solution of the relation exists provided that the Gauss condition: $\int_S \left(\mathbf{u}_\omega + \mathbf{u}_p - \mathbf{U}_b\right)\cdot\mathbf{s}dS = 0$, which leads to the conclusion that the total vorticity in the flow region should be preserved over time [6], is satisfied.

Relation (51) is similar to the formula devised by Cottet [6], but it was derived by another method and for different assumptions. It can be used to determine the vorticity generated by the flow in each point of the solid boundary. The result is more accurate than the one yielded by Chorin's formula (46).

The generated vortex sheet is then subjected to discretization:

$$\Gamma_i = -\int_{ds_i} \gamma(\mathbf{x})\cdot dS, \qquad \mathbf{x}\in S, \quad (52)$$

where ds_i is the boundary segment whose vortex sheet is changed into a vortex blob located in the centre of this segment. As a result of this operation, vortex blobs are generated in each time step, compensating the jump of the tangent velocity component on the solid boundary. As a result of advection and diffusion the vortex blobs displace whereby the vortex field evolves in the successive time steps. The displacing blobs which cross the boundaries of the flow region are eliminated from the computations.

4.3. Initial condition

According to the above description of the method of solving the flow problem, initial vorticity field (7) is approximated by a set of vortex blobs. It is assumed here that the initial vorticity field is equal to zero in each point of the region: $\boldsymbol{\omega}|_{t=0} = 0$. Thus at instant $t = 0$ the flow has a potential character. In each time step, vorticity (in the form vortex blobs) is generated along the impermeable boundaries. As a result of advection and diffusion the vortex blobs move into the region whereby the flow vorticity increases. Hence in this modeling procedure a certain number of computation steps need to be made in order to reach a balance between the number of vortex blobs generated in a given time step and the number of vortexes leaving the region through the outlet or as a result of collision with the solid boundary.

5. Conclusions

A method for simulating a flat flow confined by moving complex boundaries has been presented. The advantage of the method is that it allows one to model the evolu-

tion of a vorticity field, which means that it is suitable for high Reynolds number flow problems in which vorticity dominates, such as the flow of water through moving water-control gates and hydraulic machines and flows around airplanes and high engineering structures. By determining the velocity and vorticity fields one can analyze the hydrodynamic loads occurring during the motion of the structures, which is of great practical importance for their safety.

In the proposed method the evolution of the vorticity field is reconstructed by tracing the trajectories of the motion of vortex blobs (vorticity carriers) and recovering the velocity field on this basis. In the case of flows confined by a moving impervious boundary, specific boundary conditions (owing to which the proper velocity field is constructed in three stages) must be satisfied. In the first stage, the velocity field originating from the constellation of vortex blobs in the flow region is determined. In the second stage, the field is modified by adding a potential velocity field to it to ensure that the velocity component normal to the impervious boundaries becomes zero. The boundary element method is proposed for determining this field. In the third stage another velocity field modification, stemming from the modeling of the vortex sheet along the impervious boundaries, takes place.

An original derivation of a formula for vortex sheet intensity, based on the single layer potential theory, leading to the formulation of a Fredholm equation of the second kind for vortex layer intensity, is presented. Thanks to this it is possible to accurately calculate the vorticity of the layer from which vortex blobs are generated along the boundary of the region. The blobs make the velocity component tangent to the moving or immobile boundary disappear.

The vortex method as a particle method does not require approximation of the computation area on a numerical grid – which is its strong advantage – owing to the fact that the method's algorithm does not generate a numerical error in the form of numerical diffusion arising on the grid. Also the moving boundary condition can be easily implemented in this method since no dynamic deformation or modification of the computation grid occurs here.

This is the first part of a work covering the theoretical foundations and the general description of the vortex method algorithms and boundary conditions. An example of the computation of the vorticity and velocity fields of the flow through a moving hydraulic gate will be presented in the second part of the work.

References

[1] Aydin I., Telci I., Dundar O.: *Prediction of downpull on closing high head gates*, J. Hydraul. Res. IAHR, Vol. 44, 6, 2006, pp. 822–831.

[2] Beale J.T., Majda A.: *Vortex methods I: Convergence in three dimensions*, Math. Comp., Vol. 39, 1982, pp. 1–27.

[3] Beale J.T., Majda A.: *Vortex methods II: Higher order accuracy in two and three dimensions*, Math. Comp., Vol. 39, 1982, pp. 29–52.

[4] Billeter P.: *Properties of single shear layer instabilities and vortex-inducted excitation mechanisms of thick plates*, Journal of Fluids and Structures, Vol. 19, 2004, pp. 335–348.
[5] Chorin A.J.: *Numerical study of slightly Viscous flow*, J. Fluid Mech., 57, 1973, pp. 785–796.
[6] Cottet G.H., Koumoutsakos P.D.: *Vortex Methods: Theory and Practice*, Cambridge University Press, 2000.
[7] Eldredge J.D., Colonius T., Leonard A.: *A Vortex Particle Method for Two-Dimensional Compressible Flow*, J. Comput. Phys., Vol. 179, 2002, pp. 371–399.
[8] Gaul L., Kögl M., Wagber M.: *Boundary element methods for engineers and scientists, an introductory course with advanced topics*, Springer-Verlag, Berlin Heidelberg, 2003.
[9] Gharakhani A., Ghoniem A.F.: *Three-Dimensional Vortex Simulation of Time Dependent Incompressible Internal Viscous Flows*, J. Comp. Phys., 1997, pp. 75–95.
[10] Hald O.H.: *Convergence of vortex methods for Euler's equations II*, SIAM J. Numer. Anal., 16, 1979, pp. 726–755.
[11] Leonard A.: *Vortex methods for flow simulation*, J. Comput. Phys., 37, 1980, pp. 289–335.
[12] Majda A.J., Bertozzi A.L.: *Vorticity and Incompressible Flow*, Cambridge University Press, Cambridge, 2002.
[13] Ploumhans P., Winckelmans G.S.: *Vortex methods for high-resolution simulation of viscous flow past bluff bodies of general geometry*, J. Comput. Phys., 165, 2000, pp. 354–406.
[14] Shankar S., Van Dommelen L.: *A new Diffusion Procedure for Vortex Methods*, J. Comput. Phys., Vol. 127, 1996, pp. 88–109.
[15] Thang N.D.: *Gate Vibrations due to Unstable Flow Separation*, J. Hydr. Eng., Vol. 116, No. 3, 1990, pp. 342–361.

Numeryczne modelowanie przepływu przez ruchome zamknięcia wodne metodą wirów. Część I rozwiązanie teoretyczne

Zaprezentowano metodę wirów dyskretnych dla symulacji płaskiego przepływu ograniczonego złożonymi ruchomymi brzegami. Zaletą tej metody jest możliwość modelowania przepływu z dużą liczbą Reynoldsa, dzięki wykorzystaniu zmiennych Lagrange'a – trajektorii cząstek wirowych do wyznaczania ewolucji pól wirowości i prędkości.

Przedstawiono sposób formułowania warunków brzegowych dla przepływów ograniczonych nieprzepuszczalnym i ruchomym brzegiem, polegający na superpozycji trzech pół prędkości. Pierwszego, pochodzącego od cząstek wirowych, drugiego potencjalnego spełniającego warunek brzegowy no-through-flow oraz trzeciego wynikającego z modelowania warstwy wirowej wzdłuż brzegów nieprzepuszczalnych spełniającego warunek no-slip-flow.

W niniejszej pracy przedstawiono oryginalne wyprowadzenie formuły na wyznaczanie natężenia warstwy wirowej na podstawie teorii potencjału warstwy pojedynczej prowadzące do sformułowania równania Fredholma drugiego rodzaju dla natężenia warstwy wirowej. Niniejsza praca stanowi część pierwszą, obejmującą podstawy teoretyczne i ogólny opis algorytmów metody wirów oraz warunków brzegowych. Przykład obliczenia pól wirowości i prędkości przepływu przez zamknięcie wodne znajdujące się w ruchu zostanie przedstawiony w drugiej części pracy.

ARCHIVES OF CIVIL AND MECHANICAL ENGINEERING

Vol. VIII 2008 No. 3

Influence of internal cracks on bond in cracked concrete structures

J. PĘDZIWIATR
Wroclaw University of Technology, Wybrzeże Wyspiańskiego 17, 50-370 Wrocław, Poland

The bond between concrete and steel bars is of fundamental importance to deformation characteristics of cracked concrete structures. It has been extensively studied for many years, particularly from the early 1970s. But the results of the studies seem to be inadequate for concrete structure analysis. They are not reflected in engineering practice and codes. This is mainly due to the fact that most of the experimental research has been conducted on specimens with very short embedded length. The behaviour of such specimens differs very much from that of a real cracked concrete structure with a tension zone. One of the most important differences is the presence of internal cracks in the real member. Internal cracks arise close to the steel bars and develop towards the member's edge. Although they are invisible while inside the member, they change the strain distribution in the steel along the bars and so affect the bond. When they reach the edge, they become so-called 'secondary cracks'. Internal cracks are responsible for a large scatter in crack width and spacing. Research into internal cracking and its effect on bond can provide a convincing explanation of the phenomenon of irregular concrete strain distribution in a reinforced cross section under uniaxial tension. In Wroclaw University of Technology's Institute of Building Engineering, specimens were designed and prepared specifically for the direct observation of internal cracks and the measurement of steel and concrete strains. Such specimens and experiments are more expensive and time-consuming but the results reflect the behaviour of real concrete members much better. The experimental data confirmed the theoretical predictions and allowed us to make the model more accurate.

Keywords: *concrete, cracking, bond-slip, internal cracks propagation, specimens, research*

1. Introduction

Typical reinforced concrete structures are designed assuming that concrete and steel bars work together in carrying loads. As long as there are no cracks in the tension zone, the interaction is based on ideal primary bond. This means that in any cross section, the strain value in a steel bar is the same as in the adjacent concrete, i.e. $\varepsilon_s = \varepsilon_{ct}$. At such load levels the bond is based on adhesion forces. After cracking the situation is much more complicated. The strains in the steel are much greater than the ones in the concrete and slip occurs between the steel bar and the surrounding concrete, which breaks the adhesion. The transfer of tensile forces takes place through the bearing action of the bar's lugs and steel-concrete friction. Since a cracking state is typical for concrete members with a tensile zone, the latter bond mechanism is more important than the primary bond. Theoretical and experimental research on this phenomenon has been conducted for many years, particularly intensively in the 1980s and 90s when

a concept of the unique character of bond gained acceptance [1, 2]. As a result, specimens similar to the one shown in Figure 1 have dominated experimental research.

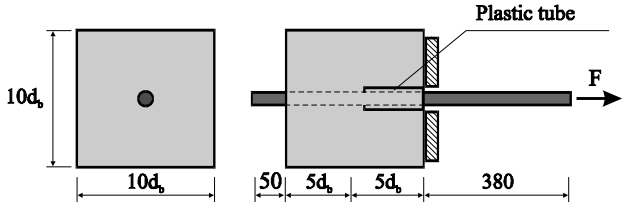

Fig. 1. Typical specimen recommended by RILEM [3]

Since characteristic transfer length l_b is very short – ranging from 3 to 5 bar diameters d_b – one can assume that steel strain changes linearly and bond stress τ_b is constant. Bond stress can be calculated from this simple formula:

$$\tau_b = \frac{F}{\pi d_b l_b}. \tag{1}$$

Hence to study bond one needs to measure only acting force F and bar slip Δ (or s). Experiments on specimens with a very short transfer length are relatively inexpensive and simple. They allow one to study many interesting parameters, e.g. rib patterns [4, 5], concrete strength [4, 5, 6], concrete cover and loading history. But the behaviour of such specimens differs greatly from that of a cracked concrete structure [7]. The most important differences are:

a) The front of the specimens behaves quite differently than the area near a crack in concrete members.

- In the specimens, slip and bond stress appear directly after loading. In concrete structures, both of them are equal to zero as long as the load is below the cracking level.
- Tests on the specimens lead to growing function $\tau_b = \tau_b(\Delta)$. This means that the peak bond stress occurs in the cracked cross section where slip is maximum and so $\tau_b = 0$. The maximum bond stress value is at a distance of about 1.5–2.0 d_b (d_b – a bar diameter) from the crack. Moreover, as the load increases, the location of $\tau_{b,\max}$ moves away from the cracked cross section.
- The specimen's smooth surface implies strain concentration in the perpendicular cross section, which may result in the deterioration of local bond. In a real member, the crack's surface is irregular whereby this effect is limited.

b) In a concrete member, cracks occur in the tension zone and so both the concrete and the steel are in tension. In a pull-out test specimen the concrete is compressed.

c) During tests one can observe that the bar's free end slips when the load is heavy enough. In cracked structural members there are always places where $\Delta = 0$, irrespec-

tive of the load level. This significantly affects bond deterioration, particularly under cyclic loading.

d) In the pullout test, some radial cracks may appear if the concrete cover is thin [8]. Such cracks originate near the bar's surface (so-called internal cracks) and propagate towards the concrete specimen's edge. They appear on the specimen's face where $\Delta = \Delta_{max}$ and $\tau = \tau_{max}$. In a structural member the problem of internal cracks is much more complicated. Two types of internal cracks, which have a very significant influence on the whole process of bond development, can be distinguished. In the pull out test only one type of cracks – longitudinal cracks – can be studied. The other type is much more important but cannot be observed in such experiments because of the too short transfer length.

2. Experimental and theoretical background

2.1. Experimental background

Primary cracks arise at the external surface of concrete members and are easy to observe. More sophisticated methods must be used to investigate internal cracking. Y. Goto was the first to carry out an experiment proving the existence of internal cracks [9]. According to him, internal cracks appear at each bar rib. Most of them have a very small width and extent. They are inclined towards the bar axis. Later, more precise studies [10] showed that such internal cracks are concentrated only in some cross sections. Thanks to the X-ray technique, it was possible to see that internal cracks are located mainly near the specimen's loaded end (in the initial part of the transfer length). Their extent is the larger, the closer they are to the loaded end.

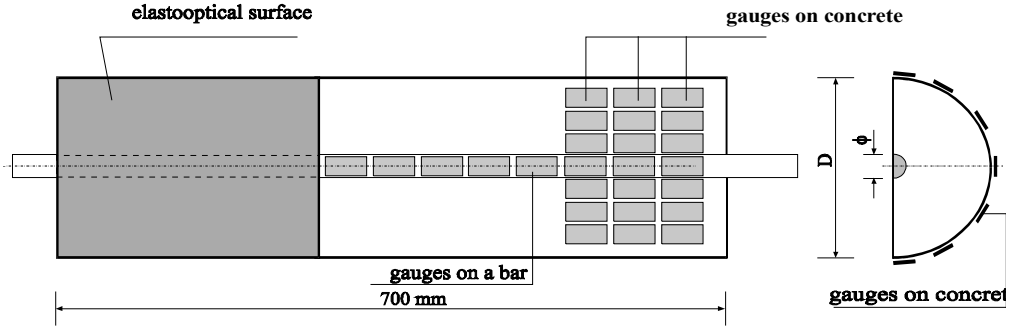

Fig. 2. Typical specimen designed in WUT

Internal cracks described in [9, 10] stay inside a member and are not visible in common concrete elements. In an atypical specimen [8], another type of internal crack was observed. The crack originated at the bar-concrete interface and quickly reached the external surface. Such cracks are called secondary since they are usually located

between primary cracks and become visible much later than the primary cracks. Even this brief overview of internal cracks indicates that they play a major role in bond processes. It also becomes apparent that no comprehensive research on this problem exists. In Wroclaw University of Technology's Institute of Building Engineering experimental research was conducted form the beginning of the 1990s to 2001. The research program and the types of tested elements were chosen on the basis of the previously developed theoretical model and the results obtained on its basis [11]. The experiments were carried out on elements under axial and eccentric tension and bending. Figure 2 shows typical specimens for eccentric tension tests.

The novel idea was to use reinforcement bars milled down to half of their diameter and place them in such a way that their even surface was flush with the surface of concrete. The milling accuracy was not lower than 2–3 % and the bar's surface area was determined similarly as the nominal diameter of the ribbed steel reinforcement. Such specimens allow one to directly measure deformations in the reinforcement and in the surrounding concrete. The use of photographs showing the deformations of a photo elastic coating applied to the element's surface was another important decision. The coating was applied in different parts of the specimen (at its end or in its middle part) and covered either ½ or ¼ of its surface. Since the photo elastic coating changes locally the surface concrete layer in the element's tension zone, it was not used in quantitative analyses, but only to observe phenomena. The visualization made it possible to continuously observe deformations in the concrete and in the reinforcement, resulting in the creation of deformation concentration zones and the initiation of primary and internal cracks. The transformation of internal cracks into secondary cracks and the phenomena associated with the gradual loss of bond in the region directly surrounding the cracks could also be observed. Typical deformed Polish steel 34GS with ϕ8–16 bar diameter was used in the experiments. The specimens were made of concrete based on ordinary Portland cement CEM I 32.5 (and partly CEM I 42.5) with the gravel to sand to cement ratio: g/s/c = 3:2:1. The w/c ratio was approximately 0.5. Because of the element size the maximum gravel grading was 8 mm. Since the mixture contained a lot of small gravel fractions, long-term curing was necessary to prevent shrinkage from disturbing the course of the observed processes.

2.2. Theoretical background

When a primary crack formed at the edge reaches the reinforcing bar, a local break down of the primary bond occurs. Secondary bond makes possible the transfer of forces from the steel bar to the surrounding concrete mainly thanks to the bearing action of the steel bar ribs – forces F_n and F_t (Figure 3). Resultant force W is in equilibrium with forces F_s and F_b acting on the surrounding concrete. Force F_s is perpendicular to the bar's axis and acts as internal pressure on the concrete cover [8]. It can split the cover if the latter is thin. Force F_b is a source of the secondary bond.

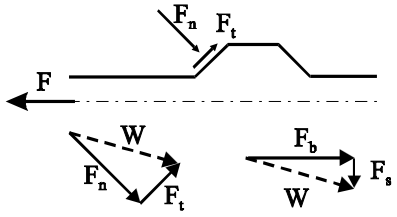

Fig. 3. Forces F_n and F_t acting on rib and forces F_s and F_b acting on concrete

After primary cracking steel strain is much greater than concrete strain at the same level and in the same cross section. Now the compatibility condition for deformation has this form:

$$\varepsilon_s(x) - \varepsilon_{ct}(x) = \frac{d\Delta(x)}{dx}. \tag{2}$$

Steel stress σ_s can decrease (with the distance from the cracked cross section (x = 0)) thanks to the bond stresses acting on the bar's surface:

$$\frac{d\sigma_s(x)}{dx} = \mp \frac{4\tau_b(x)}{d_b}. \tag{3}$$

From the experimental data and the theoretical studies the following bond function was determined:

$$\tau_b(x) = g\sigma_s(x)x^{\alpha}. \tag{4}$$

This bond function seems to be much better than the commonly used relation: $\tau_b = \tau_{b,\max}\left(\frac{\Delta}{\Delta_{\max}}\right)^{\alpha}$. The function takes into account not only the stress level (the slip value), but also the distance (x) from the cracked cross section. The experimental parameters are α and g.

Equations (3) and (4) lead to a differential equation whose solution has this form:

$$\sigma_s(x) = \sigma_0 \exp\left(-\frac{4gx^{1+\alpha}}{(1+\alpha)d_b}\right). \tag{5}$$

In Equation (5) σ_0 is the value of steel stress in the cracked cross section. Substituting (5) into (4) one can calculate the bond stress.

Bond stresses acting along the bar imply additional elongation and strain in the concrete surrounding the bar. The elongation can be estimated using the elastic theory solution for an infinite half-plane loaded by linearly distributed forces. The relationship between concrete elongations u_c (x, y) and bond stress has the following form:

$$u_c = \frac{d_b}{4E_{cm}} \int_0^x \tau_b(\alpha) \left(\left[\frac{2(1-\nu_c)}{\left(y^2+\alpha^2\right)^{0.5}} + \frac{\alpha^2}{\left(y^2+\alpha^2\right)^{1.5}} \right] d\alpha \right). \tag{6}$$

Coordinate x describes the distance from the cracked cross section along the bar while perpendicular coordinate y represents the distance from the bar's surface. Since the above function quickly decreases as y increases, the estimation is quite good. E_{cm} is a modulus of elasticity of concrete and ν_c is Poisson's ratio.

The highest values of additional strain in concrete occur at the bar-concrete interface ($y = 0$). The additional concrete strain is expressed by:

$$\delta\varepsilon_{ct}(x) = \frac{\tau_b(x) d_b}{4E_{cm}} \left[\frac{(3-2\nu_c)}{x} \right]. \tag{7}$$

A general condition at which an internal crack arises has this form:

$$\varepsilon_{ct}(x) + \delta\varepsilon_{ct}(x) = \frac{f_{ctm}}{E_{cm}}, \tag{8}$$

where f_{ctm} is an average concrete tensile strength.

A particular form of (8) depends on function $\varepsilon_{ct}(x)$ which takes into account the cross-sectional geometry and the kind of load (uniaxial or eccentric tension or bending).Generally, equation (8) has two solutions which indicate the place where an internal crack appears. One solution yields $x \approx 0$ and is associated with the dominating influence of additional strain due to bond. This solution represents internal cracks which may arise very close to the loaded end (the case of 'short transfer length') or near a primary crack. Since the additional strain decreases very quickly with distance from the bar's surface, it is obvious from (6) that such cracks will have a very small extent. For this reason they do not play a significant role in a concrete structure. A different situation occurs at the specimen's loaded end because bond stress there is the highest. As a result, the additional strain tends to infinity: for $x = y = 0$ and even for $y > 0$ it is $\delta\varepsilon_{ct} \geq \frac{f_{ctm}}{E_{cm}}$.

The other solution, in which the dominating factor is $\varepsilon_{ct}(x)$ with $x \approx a$, where a is the length of primary bond deterioration, is of much greater importance. Initially the extent of an internal crack is very small, but as the load increases, the peak value of τ_b

moves away from the primary crack and comes close to the internal crack. The role of additional strains increases and internal cracks develop. Internal cracks and their influence on strain distribution and on bond were examined during experimental tests carried out on specimens shown in Figure 2.

3. Some experimental results

3.1. Generation and development of primary and internal cracks

Primary cracks form at the edge of a specimen when the strain in its concrete reaches an ultimate value corresponding to the concrete's tensile strength. In most cases, the scatter of strength is significant. As a result, at a load level below that of average cracking only single cracks appear in places where concrete is the weakest. Initially they do not reach the steel bar and their influence on bond or strain distribution along the bar is very small. They can be called 'seeds' of cracks since only some of them will develop into primary cracks. A seed of a crack is shown in Figure 4.

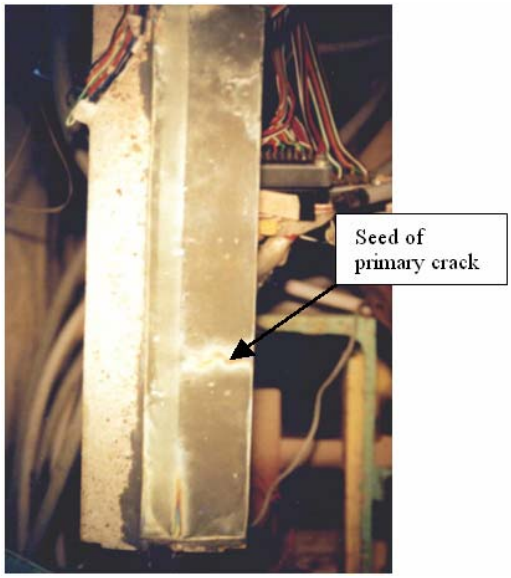

Fig. 4. Generation of primary crack

The lighter line corresponds to a local strain concentration. Since an elastic optic surface changes the properties of concrete, it was not used in quantitative analyses, but only for the registration of phenomena. In another part of the specimen electric gauges were used for more precise analysis. Figure 5 shows changes in steel strain distribution (multiplied by 10^6) for one of the tested specimens. At point $x \approx 28$ cm the first

primary crack reached the bar surface at load $F \approx 1.4$ kN. Even though the load increased to almost F ≈ 2.9 kN, 'nothing' happened in the other parts of the specimen – no other primary cracks appeared.

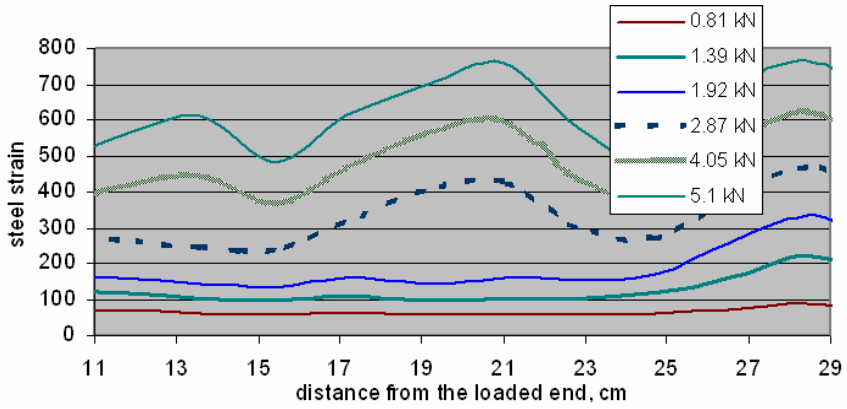

Fig. 5. Changes in steel strain distribution along bar (Steel strain multiplied by 10^6)

Similar conclusions can be drawn from Figure 6 which shows a distribution of bond stress calculated from this formula

$$\tau_{b,k} = \frac{E_s d_b}{4} \frac{\varepsilon_{s,i+1} - \varepsilon_{s,i}}{x_{i+1} - x_i}. \tag{9}$$

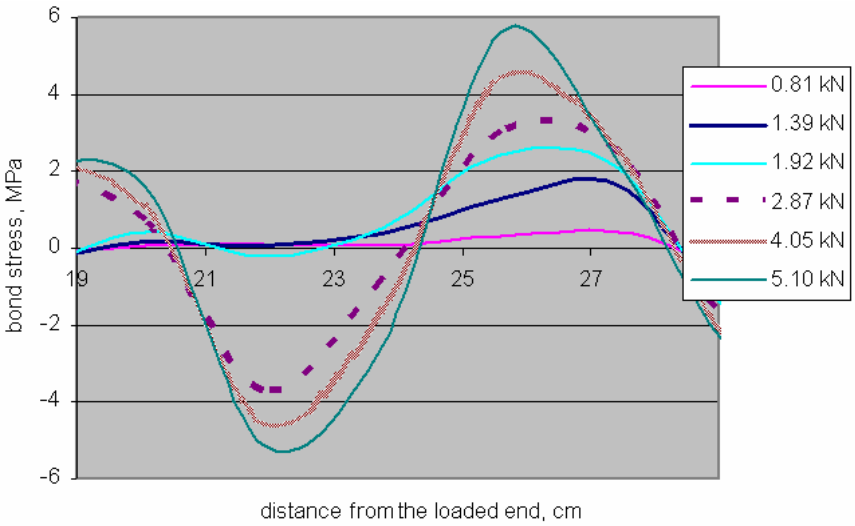

Fig. 6. Changes in bond stress distribution along bar

The $\tau_{b,k}$ value represents bond stress at point k between gauges i+1 and i. The strains in the steel were measured by electric gauges glued to the bar. Having approximated $\varepsilon_{s,i}$, one can use relation (3). The results obtained by the two methods are very similar.

The obtained results – no other cracks and practically zero bond stress – cannot be explained by the probabilistic character of concrete tensile strength since the second crack (at $x \approx 20$ cm) appears at a load twice larger and the third one (at $x \approx 13$ cm) at $F \approx 4.0$ kN. This is due to the development of internal cracks. Such a crack is shown in Figure 7. According to the theoretical model, the crack is located quite far from the primary crack. As long as there is no significant increase in load, it remains inside and has only a slight influence on bond distribution. Bond stress increases with load and its maximum shifts towards the location of an internal crack (see Figure 6), contributing to its development. The crack's width and extent increase. If the concrete cover is thin, the crack can reach the element's edge. This crack is referred to as secondary. In Figure 8 one can see that the internal crack shown in Figure 7 reached the edge and became a secondary crack.

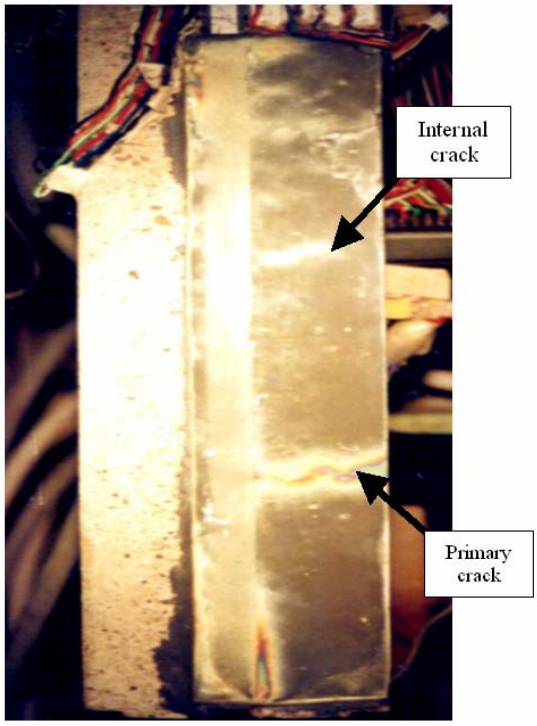

Fig. 7. Development of primary crack and generation of internal crack

This happened as a result of the simultaneous action of the external load and the bond forces. One can also see other small internal cracks in Figure 8. They are differ-

ent from the previously formed cracks and are situated very close to secondary (or primary) cracks. This means that they are caused solely by bond forces (strain in concrete near a crack is now very small). Their development is possible only if bond stress increases. At this load level changes in bond are already relatively small and in most cases such internal cracks remain inside the concrete member [12].

In our tests internal cracks can be observed, but in real concrete members they are invisible until they become secondary cracks. The development of cracks inside an element is highly interesting. Such cracks are invisible to researchers measuring the element's elongation. The only thing which they notice is that the element's deformation is larger than that of a similar element made solely of concrete. This observation suggests that reinforcement has a positive influence on the deformation of concrete and improves its homogeneity. In light of the conducted experiments this theory seems to be false.

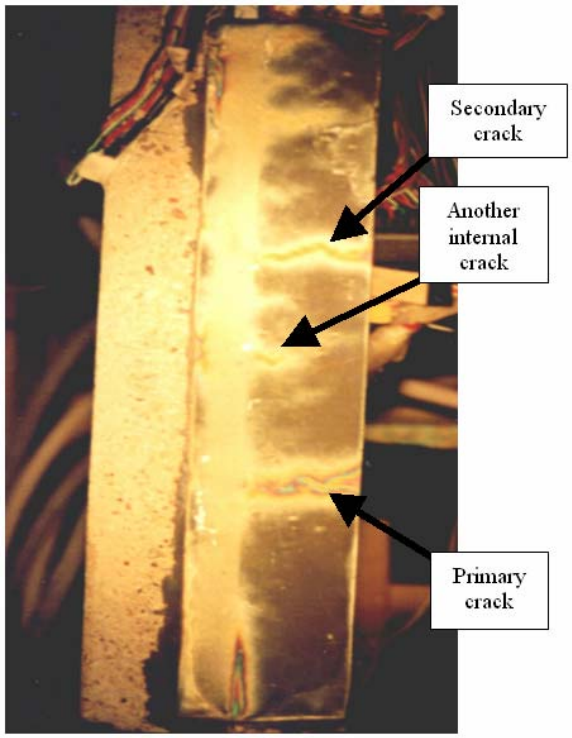

Fig. 8. Development of secondary crack and generation of internal crack

The existence of two types of cracks of different origin explains the considerable scatter of crack width and spacing observed in many tests. The differences are much larger than it could be expected from the variation in concrete tension strength. An analysis of the development of internal cracks provides a reasonable clarification. For

practical reasons, crack width is measured on the external surface of concrete. In the case of primary cracks, this is the place where their width is the largest. Whereas internal cracks are the widest at the reinforcement and their width decreases as they approach the edge. Thus the difference in width is the largest on the element surface. As the load increases the difference in crack width diminishes, but still remains significant.

The role of internal cracks is very important in members subjected to uniaxial or eccentric tension, where concrete strains in the tension zone are the same (or very similar) in the whole perpendicular cross section. Members under bending exhibit large differences in strain at the bar level and at the element's bottom end (especially when the concrete cover is thick). This is why only primary cracks are generated at the initial stage of cracking. Their 'seeds' are randomly placed, depending on local concrete strength. Some of them become primary cracks. This situation lasts for quite a long period, but it does not mean that no internal cracks appear in bending elements. Such cracks are generated by practically exclusively the deformations caused by bond forces. The deformations are comparable to the limit deformations in concrete when bond stress is considerable (10 MPa and more). This occurs at high load levels. The late formation of internal cracks is characteristic for bending elements. The cracks are similar to the ones which appear in tensioned elements after the transformation of internal cracks into secondary cracks. There is also similarity in their location close to primary cracks.

3.2. Concrete strain distribution in perpendicular cross section

Also the irregular distribution of concrete strain in the perpendicular cross section of members subjected to uniaxial tension can be explained thanks to the experiments carried out on the specimens shown in Figure 2. In some investigations and in theoretical models much higher concrete strains are observed near the bar than at the specimen's edge. The existing solutions do not provide a clue as to the origin of this phenomenon and are based on the assumptions that the ratio of average to maximum concrete stress is constant and independent of the location of the cross section and the load level. The above assumptions are incorrect and lead to erroneous conclusions.

The results of tests carried out on members subjected to eccentric tension support the theoretical model's thesis that the only source of deformations is the displacement of concrete caused by bond forces [13]. The phenomenon was investigated in detail on a few chosen elements. In some sections differently situated relative to the crack (located at a different distance from the element's front) strain gauges were installed parallel to the bar's axis. Figure 9 shows typical test results (strains in concrete are multiplied by 10^6) for a section located at a distance of x = 36 mm (about 2.0 d_b) from a crack. It is easy to notice that before cracking ($F \leq 6$ kN), deformations in concrete are almost the same in all the sections. After cracking, the bond causes additional elongation. The fact that a significant increase in deformations in the area adjacent to

the reinforcement is accompanied by a small decrease within the edge area is also worth noticing. The differences in concrete strain persist during further loading, but at a certain load level ($F \leq 15$ kN) a general decrease in concrete deformations occurs. This is mainly due to a reduction in τ_b, caused by the movement of the $\tau_{b,\max}$ value, which has already been discussed.

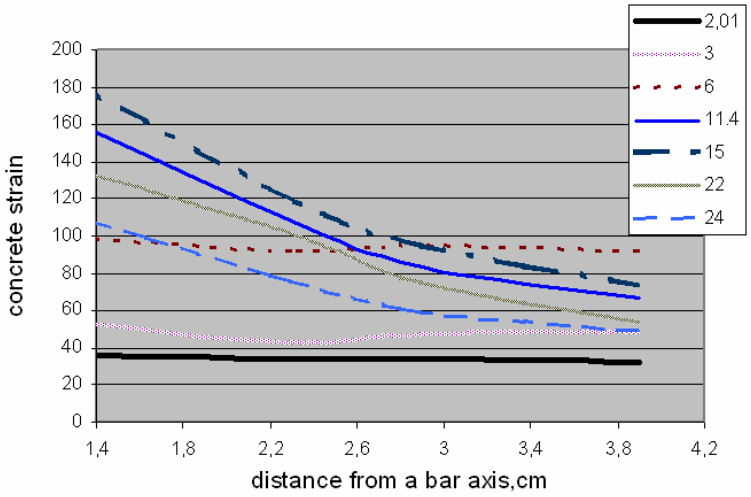

Fig. 9. Typical concrete strain distribution in perpendicular cross section

The results of similar tests done for a section located approximately in the middle of the distance between cracks are shown in Table. No significant differences in the strain gauges' indications were recorded. This confirms the theory that the differentiation in deformation is due to stresses τ_b, which are close to zero in this section. Since the additional deformations are caused by the displacement of concrete, they can exceed $\varepsilon_{ct,ult}$ without initiating a crack. Nevertheless, they add up to the deformations caused directly by the load, which results in the generation of internal cracks. This problem has already been discussed.

4. Conclusions

The transfer of forces from the steel bar to the surrounding concrete plays a fundamental role in the deformation of concrete structures after cracking. The secondary bond which then forms has a great influence on the width and spacing of cracks, the member's rigidity and the bar's elongation. Investigations of bond in a structure are complicated and require well-designed specimens. The specimens designed in WUT are sufficiently long for a few cracks to appear. Thanks to their shape and the specially prepared reinforcement which is flush with the concrete face one can observe the whole bond process. Conventional electric gauges and the photo elastic coating tech-

nique are complementary to each other. As a result, the obtained results are highly reliable. Moreover, the experimental data were found to be in good agreement with the predictions based on the theoretical model.

Some of the most interesting observations and measurements relate to internal cracks. Two kinds of such cracks can appear in a concrete structure. Both originate near the bar's surface but their causes, development and influence on the structure are different.

Table. Concrete strain distribution in section between cracks

Load, kN	Gauges number/ Concrete strain, $\mu m/m$				Average concrete strain $\mu m/m$	Variation coefficient
	4	5	6	7		
6.02	50	46	44	36	44	0.12
8.99	58	59	61	55	58	0.04
11.36	63	64	70	63	65	0.04
11.33	58	58	65	59	60	0.05
13.01	72	73	81	75	75	0.05
14.98	77	79	86	85	82	0.05
17.02	76	80	91	91	85	0.08
19.06	73	78	89	87	82	0.08
21.04	70	77	88	80	79	0.08
22.04	68	72	87	75	76	0.09
24.01	58	64	76	52	63	0.14

Cracks which appear as a result of the simultaneous action of the external tension and the additional elongation caused by bond are much more important. They mainly occur and play an important role in concrete members subjected to uniaxial or eccentric tension, i.e. when the whole perpendicular cross section is under tension. Their spacing is determined by bond. If the concrete cover is thin, they may reach the concrete surface and become secondary cracks. At the same load level their width is smaller than that of primary cracks. Small internal cracks appear at a much higher load level. They are mainly caused by additional elongation due to bond forces – at this load level, strains in concrete under tension are relatively small (and decreasing). Such internal cracks are situated quite close to a primary or secondary crack where bond stress is maximum (often equal to 10 MPa or more). Cracks of this kind appear in both tension and bending members. They have little chance of becoming secondary cracks (this depends on the thickness of the concrete cover).

It has been determined that in members under tension crack spacing is governed mainly by bond properties while in members under bending the probabilistic nature of concrete tensile strength plays a fundamental role.

The tests carried out on the specimens designed in WUT made more precise bond studies possible. They were more expensive and time-consuming than tests on short specimens, but the results are much more closer to reality.

References

[1] Base G.D.: *Bond, and control of cracking in reinforced concrete*, Proceedings, International Conference on Bond in Concrete, London, 1982, pp. 331–341.
[2] Malvar L.J.: *Confinement stress dependent bond behaviour, experimental investigation*, Proceedings, International Conference on Bond in Concrete, Riga, Oct. 1992, pp. 1–79, 1–88.
[3] RILEM/CEB/FIP, *Recommendations on reinforcement steel for reinforced concrete*, Revised edition of RC6 Bond test for reinforcement steel: (2). Pull-out test, CEB News, May 1983, No. 73.
[4] Soretz S., Hölzenbein H.: *Influence of Rib Dimension of Reinforcing Bars on Bond and Bendability*, ACI Journal, Vol. 76, No. 1, 1979, pp. 111–125.
[5] Kimura H., Jirsa J.: *Effects of Bar Deformation and Concrete Strength on Bond of Reinforcing Steel to Concrete*, Proceedings, International Conference on Bond in Concrete, Riga, Oct. 1992, pp. 1–100 to 1–109.
[6] Esfahani R., Rangan V.: *Local Bond Strength of Reinforcing Bars in Normal Strength and High-Strength Concrete*, ACI Structural Journal, Vol. 95, No. 2, 1998, pp. 96–106.
[7] Cairns J., Plizzari G.A.: *Do we need a standard test for bond*, Proceedings, International Conference – "Bond in Concrete – from research to standards", Budapest, 2002, pp. 259–267.
[8] Tepfers, R., Olsson P.: *Ring Tests for Evaluation of Bond Properties of Reinforcing Bars*, Proceedings, International Conference on Bond in Concrete, Riga, Oct. 1992, pp. 1–89, 1–99.
[9] Goto Y.: *Cracks formed in concrete around deformed bars*, Journal of ACI, Vol. 68, No. 4, pp. 244–251.
[10] Otsuka K., Ozaka Y.: *Group effect on anchorage strength of deformed bars embedded in massive concrete block*, Proceedings, International Conference on Bond in Concrete, Riga, Oct. 1992, pp.1–38, 1–47.
[11] Pędziwiatr J.: *The new model for cracking analysis of tension reinforced members*, Archives of Civil Engineering, Vol. 42, No. 1, 1996, pp. 47–64.
[12] Pędziwiatr J., Hola J., Stys D.: *Study of the transfer of tensile forces by bond in eccentric reinforced concrete members*, 13th ECF, San Sebastian, 2000, pp. 137–144.
[13] Pędziwiatr J.: *Cracking behaviour of eccentric tension concrete members*, Proc., 3rd Int. Conf. On Analytical Models and New Concepts in Mechanics of Concrete Structures. Wroclaw, 1999, pp. 223–228.

Wpływ rys wewnętrznych na przyczepność w zarysowanych konstrukcjach żelbetowych

Przyczepność jest podstawowym mechanizmem umożliwiającym przekazywanie siły ze stali na beton w zarysowanych elementach żelbetowych. Dotychczasowe intensywne studia teoretyczne i eksperymentalne na temat przyczepności nie przynoszą praktycznych efektów w odniesieniu do analizy zachowania się rzeczywistych elementów konstrukcyjnych. Jest to skutek używania nieadekwatnych elementów do prowadzenia badań i w konsekwencji przyjmowanie błędnych koncepcji teoretycznych. Badania na elementach zaprojektowanych i wykonanych w Instytucie Budownictwa Politechniki Wrocławskiej pozwoliły zdecydowanie lepiej

odwzorować warunki pracy rzeczywistych konstrukcji. W szczególności umożliwiły one określenie roli rys wewnętrznych w elemencie. Ich powstanie jest odpowiedzialne za różnice w odkształcalności elementów osiowo rozciąganych i zginanych. W elementach konstrukcyjnych o dużych otulinach są one przeważnie niewidoczne, ale już od chwili powstania modyfikują przebiegi odkształceń. Dzięki stwierdzeniu ich roli można wyjaśnić szereg paradoksów z którymi ma się do czynienia w analizie zarysowanych konstrukcji żelbetowych.

ARCHIVES OF CIVIL AND MECHANICAL ENGINEERING

Vol. VIII 2008 No. 3

Forming simulation of high-strength steels with direction-specific hardening modelling

K. ROLL, A. FAUST
Daimler AG, 71059 Sindelfingen, Germany

The behaviour of mild steels is described very well in today's forming simulation. But advanced high strength steels, especially those exhibiting induced plasticity (TRIP and TWIP steels), may show an anisotropic hardening behaviour [1] that is hardly covered by the commonly used material models. The company MATFEM offers the user material model MF Generalized Yield [2], which allows for that anisotropic hardening. In order to evaluate the usability of this model for sheet forming simulation, results of real forming experiments were compared to simulation results gained with and without the consideration of anisotropic hardening. Each hardening model was combined with a Hill 48 [3] yield locus. It can be seen that the anisotropic model delivers quite an improvement in some areas, but that this is not true in all areas of the formed part. The punch force prediction is better using the anisotropic model, but still there is no exact match with the experimental results. Overall, the model represents a very interesting concept with high potential, but still some problems. The data acquisition and treatment is very extensive and there are nearly no standardized experiments beyond the uniaxial tensile test to get the needed information about the hardening behaviour of the material. This fact, in combination with insufficient validation of the benefits of the model up to now, inhibits the usage of the model in productive simulation. But for special problems, the model delivers an attractive alternative for further yield locus optimizations.

Keywords: *anisotropy, hardening, induced plasticity*

1. Introduction

When the topic of the anisotropy of a sheet is discussed, it is the planar anisotropy that is discussed, i.e. the differences in the properties of the sheet depending on the orientation to the rolling direction. There is a range of different models available to describe this planar anisotropy. The most widespread is Hill's yield locus curve from 1948 [3]. The model extends the von Mises yield condition [4] and is presented mathematically as a rotated and slightly deformed ellipsis (Figure 1). Given its simplicity, this model, implemented in an FEM code, offers very fast computing times for satisfactory results and is very widely used in industrial application.

In addition to the yield condition, a rule is also required that describes the plastic hardening of the material during forming. Literature also offers many approaches on this subject (e.g. [5, 6]). Irrespective of which of these concepts is used, in conventional forming simulation hardening is described without taking account of the shape of the respective stress condition, i.e. tension, compression or shear, using one and the same hardening curve. From a mathematical point of view, this means that the yield locus curve is amplified uniformly in all directions (Figure 4a). The consequence of

this is that one has to find a compromise while fitting the yield locus. The parameters has to be identified for a specific equivalent plastic strain leading to a specific shape of the yield locus curve for all levels of plastic strain which cannot be changed and which has to represent the plastic behaviour and hardening in all different directions. This coordination and the procedure are very valid for the usual mild steels used to date and provide very good results. But some modern high strength and very high strength steels show a significantly non-compliant behaviour in their hardening properties in the overall plastic strain area that is of interest for forming technology. They can show a different hardening, depending on the prevalent stress condition [1]. This is shown in Figure 2 using a simulated example. As for the assumption of the isotropic hardening (Figure 2a), the yield curves for uniaxial tension, uniaxial compression, equal biaxial tension and pure shear display only a slight parallel displacement, but have the same shape and slope. This parallel displacement results from the planar anisotropy. In the right-hand section the experimental results of a transformation-intensive material are included and transferred to the model. A totally different view of the material behaviour is obtained as the result of the anisotropic hardening modelling (Figure 2b). Starting from a relatively uniform yield stress (based here on the Hill '48 model) the curves develop independent of one another in the main directions of strain of uniaxial tension, compression, shear and biaxial tensile load. This behaviour can have a specific effect if formed parts with high deformation levels are to be assessed.

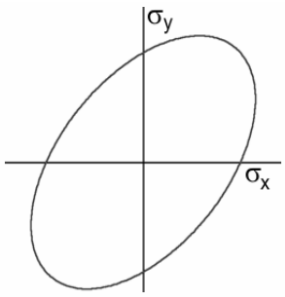

Fig. 1. Hill diagrammatic yield locus curve

If materials are to be rated with a hardening that depends in this way on the stress condition, this means that the yield locus curve with the uniform scaling of the hardening curve can illustrate this behaviour only to an unsatisfactory degree. It is more the case that the yield locus must be scaled in relation to the stress condition, which leads to a deformation of the yield locus curve during forming (Figure 4c). Even the existence of different hardening under tensile and compression strains can justify the use of an anisotropic material model for many materials and forming processes. Taking the example of a round cup, Figure 3 displays the change of the stamping force prediction of the anisotropic hardening compared to the conventional calculation for process parameters that are otherwise constant. If a conventional description of the

material in the tensile experiment is used, the actual stamping force with the set, non-optimized friction has been clearly underestimated. But if the material is adjusted not just for the tensile test, but also for other tests (compression in particular) for the anisotropic hardening model, it is not only the shape of the calculated force-path-curve that improves in comparison to the experiment. The calculated stamping force is also closer to the measured values. This results in a changed curve characteristic.

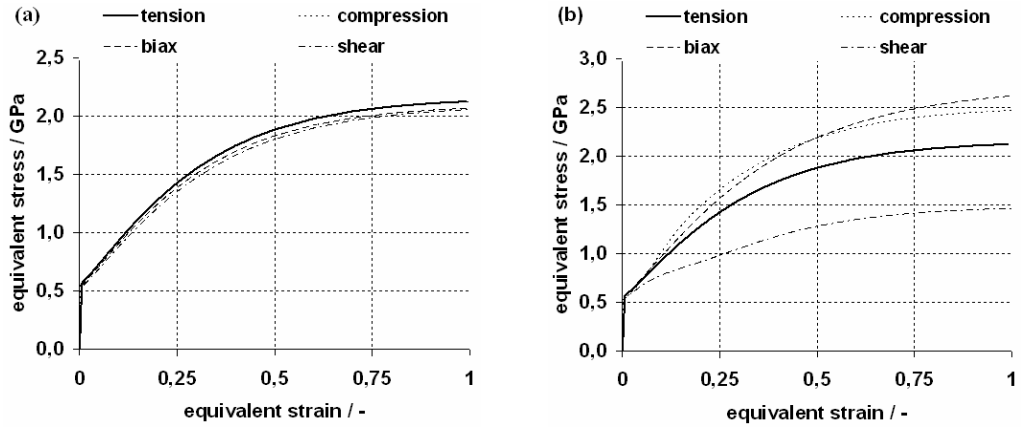

Fig. 2. Yield curves for uniaxial tension, uniaxial compression, equal biaxial tension and pure shear for the isotropic (a) and anisotropic (b) case

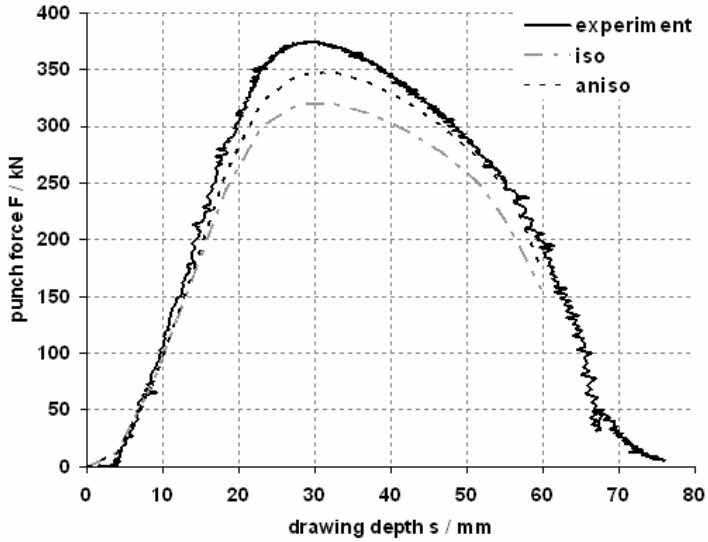

Fig. 3. Effect of the anisotropic hardening on the stamping force, using a round cup as an example

One more point about material modelling that has been investigated often to date, but that has not been fully accepted in industrial applications, is the continuous consideration of isotropic-kinematic hardening. This term means a reduction of the yield stress under a change of load, when the yield locus curve undergoes a source displacement (Figure 4b). If a uniaxial tension test is carried out and is interrupted, then the material begins to flow again at the same stress that applied when the experiment was interrupted. However, the material begins to flow at a lower stress under uniaxial compression.

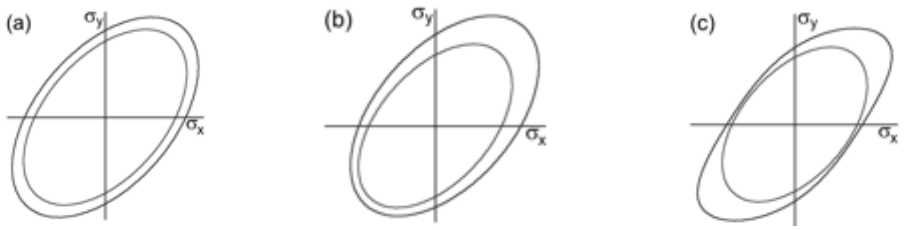

Fig. 4. Diagrammatic representation of isotropic (1), kinematic (b) and anisotropic (c) hardening

It is the case that almost all programs offer different material models that support kinematic hardening, but in most cases only in combination with von Mises' yield locus that does not take account of the planar anisotropy. The MATFEM Company has developed a user subroutine entitled MF GeneralizedYield [2] for the commercial FEM-code LS-Dyna. This program is a highly flexible interface that allows among other things the combination of almost any yield criterion with many different hardening models and can take into account anisotropic and kinematic hardening.

The theoretical differences of the different hardening models are very large, but what does this mean for the forming simulation? It must be clearly stated that the differences are important only in some circumstances. On the one hand, the very first thing is that the material must display a markedly anisotropic hardening, and this effect is greatest in steels exhibiting induced plasticity, but is not limited to them. Various structural changes and dislocation nodes that are stress-dependent as a rule occur in these steels during forming. On the other hand, there must be different stress conditions and high enough plastic strains present in the formed part to allow the differences to have an effect. The different yield curves move away from each other as the plastic strain increases, as can be seen in Figure 2. Furthermore, the effect of the isotropic-kinematic hardening is also more marked with higher plastic strains.

The results given below are based on a study in which the anisotropic hardening model was used. In addition to the pure tension test, data taken from the hydraulic bulge test, stacked compression test, compression test in the plane of the sheet material and an experiment under shear load were used to compare the different yield properties of the material in the stress combinations. All computed results were compared with those from actual experiments.

2. Tests and results

To verify the simulations, forming tests were carried out on a very high-strength steel with induced plasticity. An experimental forming tool that is also used in Daimler AG's material release process was used here (Figure 5). The tool offers e.g. the possibility to measure the actual stamping force during forming. By applying a regular point grid it is possible to ascertain the plastic strains on the surface of the finished part. The GOM Company's ARGUS system was used for the tests. A compromise had to be reached to allow for adjustment to the simulation. The simulation with membrane or shell elements runs all calculations in the middle of the sheet, the neutral fibre or membrane plane. All sizes on the surface of the sheet are ascertained indirectly from the results in the membrane plane. The optical plastic strain analysis behaves in exactly the opposite manner. In this case, all the results are obtained on the surface of the formed part and must be converted for the membrane plane. But the user must ask whether the native result from the simulation or the measurement is used. For this study all the simulation results on the shell surface were compared with the native measured result from the surface of the formed part because good experiences had been had with this method in the past. But it must be remembered to compare the same sides since the plastic strains can be different in all uneven areas on the outside and inside of the formed part.

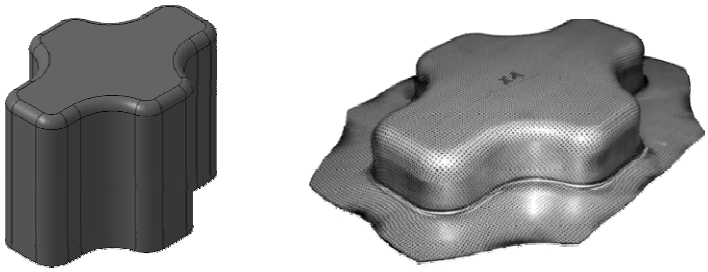

Fig. 5. Stamping geometry and test part

Deep drawing parts with a drawing depth of 40 mm were produced and then simulated with version 9.71 of LS-DYNA. Version 3.34 of the user subroutine MFGenYld was used. The yield locus was always described using the Hill model, hardening was assumed to be once isotropic, which is standard procedure, and once anisotropic.

The stamping force and the major, minor and equivalent plastic strain were used as the comparative sizes between measurement and simulation. The stamping force and the major and minor plastic strain are directly measured sizes, whereas the equivalent plastic strain is calculated from the two other plastic strains.

As well as plastic strains, one criterion for the quality of result of a forming simulation is the forming force applied to the stamping machine. This force was measured during the forming tests and is shown in Figure 6. As mentioned in the section above,

the differences between isotropic and anisotropic hardening show only at higher plastic strains, which can be identified by the fact that the force drops noticeably with effect from a drawing depth of 15 mm. It can be seen that the anisotropic calculation reflects the force maximum best of all, but none of the simulations reflect the exact force progression.

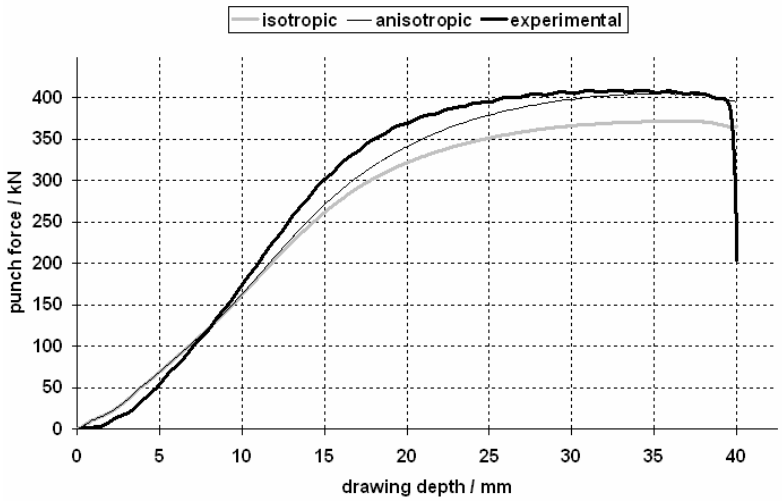

Fig. 6. Effect of the anisotropic hardening on the stamping force, using a cross cup as an example

The diagrams below show a comparison of the results obtained from measurement and the various simulations. The distributions of the major and minor plastic strain along the sections through the formed part are shown in Figure 7.

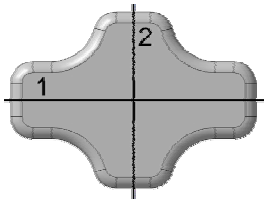

Fig. 7. Section studied

The result is not clear. As regards the major plastic strain, the areas around the die radius and the curved frame areas are better illustrated by the anisotropic calculation. At the base and stamping radius the isotropic calculation is much more like the results obtained from measurement. The representation of the minor plastic strain does not show any significant differences, the hardening modelling does not appear to have any influence here. The equivalent plastic strain shows, as a size calculated from the major

and minor plastic strain, a similar picture to the major plastic strain and is since not shown here. Part base and stamping radius are described more precisely as isotropic, frame and die radius as anisotropic.

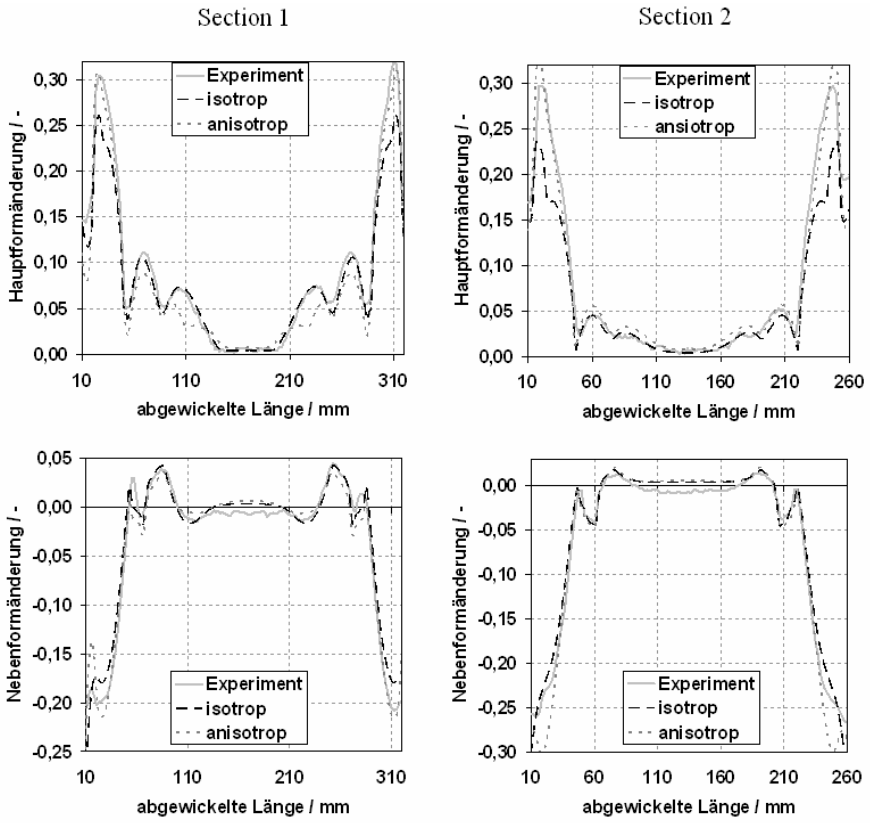

Fig. 8. Strain distribution along investigated section

3. Conclusions

The conventional simulation of deep drawing of modern high strength steels predicts only inadequately in some cases the plastic strains in the finished part. To improve the result at these locations, the consideration of the anisotropic hardening of the material represents a very promising option. In many areas a more precise prediction is obtained as a result, but in some places the result does not improve at all and even gets worse. This has many reasons. The treatment of the experimental data is extensive and is mostly based on non-standardized tests to determine them. Furthermore, only a small number of experiences with this method of description of steel hardening were gathered, thus making the verification of the compiled material cards difficult

since the earlier verification calculations are no longer adequate. There is still a great deal of potential in the processing of the experimental data, as there is in the actual determination of the input values. In the past the fundamental input value for the forming simulation was the uniaxial tension test. This test has been standardized for decades and in the meantime the result is largely independent of the testing center. In contrast, modelling of the anisotropic hardening requires some experiments that are still virgin territory experimentally and are far removed from standardization. But this is how one can get into the unfortunate position that the results for one and the same material can vary from test lab to test lab. The experiments also frequently represent an approximation to the stress condition that one would like to depict. This means, for example, in the hydraulic bulge test, the currently preferred experiment to record a yield curve under equal biaxial stress, that the biaxial tension stress is always overlaid with a bending stress that must be worked out with the help of theoretical assumptions which are of course a simplification in turn. It is also difficult to select a suitable test for recording a yield curve under pure shear. There is indeed a range of different tests, but in almost all of them the shear stress is overlaid with a not inconsiderable tension stress component, even for small plastic strains.

The behaviour of the model under load changes is also not satisfactory and experimental calculations to take account of the kinematic hardening show that this is not always correctly reflected. The anisotropic effects have also been partly overestimated, and this shows, for example, that an excessively large forming is calculated in areas with tension-compression loads in which the plastic strain is too low in the isotropic calculation. These problems stem primarily from the lack of experience with simulating sheet forming processes that take these effects into account. Further studies will be required to determine beyond doubt where the problem finally lays, whether it is the input data, the application of the model or perhaps the model itself. Overall it can be said that the method presented here has a great potential, but to exploit that potential will require some more effort and extensive development work. The current position does not yet allow for productive use in the industrial, daily forming simulation where it is vital to calculate many parts in a short time. But if the concept is pursued, then a powerful and efficient facility will be available for simulating modern very high strength steels with the same high result quality that is currently achieved with mild steels.

References

[1] Gerlach J., Keßler L.: *The impact of material testing strategies on the determination and calibration of different FEM material models*. Proc. of IDDRG 2006, 19–21 June, Porto, pp. 113–120.

[2] Gese H., Dell H., Oberhofer G.: *Verbesserte Materialmodelle für die virtuelle Auslegung von Leichtbaustrukturen im Automobilbau bei Crashbelastung, Improved material models*

for the virtual design of lightweight structures in automotive engineering under crash load, DVM 2005.
[3] Hill R.: *A theory of the yielding and plastic flow of anisotropic metals*, Proc. Roy. Soc. London, A193, 1948, pp. 281–297.
[4] v. Mises R.: *Mechanik der plastischen Formänderung von Kristallen, Mechanics of the plastic strain of crystals*, Zeitschrift für angewandte Mathematik und Mechanik, Band 8, 1928, pp. 161–185.
[5] Swift H.W.: *Plastic instability under plane stress*, J. Mech. Phys. Solids, Vol. 1, 1952, pp. 1–18.
[6] Voce E.: *The relationship between stress and strain for homogeneous deformation*., J. Inst. Met., 1948, pp. 537–562.

Symulacja kształtowania wysoko wytrzymałych stali z uwzględnieniem anizotropowego umocnienia

Obecnie w symulacjach kształtowania bardzo dobrze jest opisane zachowanie miękkich stali. Niestety wysoko wytrzymałe stale (stale TRIP i TWIP), mogą wykazywać anizotropowy sposób umocnienia, co powoduje, że źle są opisywane przez stosowane modele materiałów. Przedsiębiorstwo MATFEM oferuje użytkownikowi model materiału, który uwzględnia także anizotropowe umocnienie. Aby ocenić użyteczność tego modelu do symulacji kształtowania blach, wyniki rzeczywistych eksperymentów zostały porównane z wynikami symulacji uzyskanymi z uwzględnieniem i bez uwzględnienia anizotropowego sposobu umocnienia. Każdy model został połączony z warunkiem plastyczności Hilla 48. Wykazano, że anizotropowy model dostarcza znaczną poprawę wyników tylko w pewnych obszarach kształtowanej części. Prognozowanie siły stempla jest lepsze przy zastosowaniu modelu anizotropowego, ale nadal dokładność dopasowania do wyników eksperymentu rzeczywistego jest ograniczona. Obecnie poza próbą jednoosiowego rozciągania nie ma prawie żadnych prób do badania sposobu umacniania się materiału. Niestety, fakty te w połączeniu z niedostatecznym uzasadnieniem korzyści modelu hamują stosowanie jego w symulacjach dotyczących procesów produkcyjnych. Dla wybranych problemów, przedstawiony model jest atrakcyjny ze względu na możliwość optymalizacji powierzchni plastyczności.

ARCHIVES OF CIVIL AND MECHANICAL ENGINEERING

Vol. VIII 2008 No. 3

Caterpillar drive shaft damage causes analysis

E. RUSINSKI, P. HARNATKIEWICZ
Wroclaw University of Technology, Faculty of Mechanical Engineering, Lukasiewicza 7/9, Wroclaw 50-371, Poland

M. BOBYR, B. YAKHNO
National Technical University of Ukraine "Kiev Polytechnic Institute", Institute of Mechanical Engineering, Peremogi Ave, 37 Kiev 03056, Ukraine

The paper presents examples of fatigue stress fractures of quarry equipment drive shafts. In order to determine the real cause of this damage, we have performed a detailed analysis of the problem The paper presents the experimental data, numerical analysis and metallographic examination.

Keywords: *FE analyses, fatigue analyses, damage, crack, metallographic examination, caterpillar drive shaft*

1. Introduction

Machine elements and assemblies in the cases of the to variable loads are subject to fatigue stress, which under certain circumstances can lead to fatigue fractures and ultimately machine failure. Analysis of failures caused by fractures shows that the majority of them can be attributed to material fatigue [1].

Current design processes are still based on analytical methods and standards for defining immediate strength and fatigue parameters.

These methods are based on analytical and empirical solutions, which in many (geometrically or load-wise) complicated cases allow only for a rough approximation of strength characteristics. It is especially difficult to define strength parameters in notch shapes/technological notches, which leads to unavoidable design errors and thus can cause exploitation problems [1, 2].

Fatigue stress research is usually either oriented towards a certain practical application or a particular theoretical fatigue analysis case and therefore generally does not take into account the fact that the analyzed construction is actually not an isolated object, i.e. that it is situated within a certain environment [3, 6]. Generally, such environment can be characterized by a given variability, which more or less affects material fatigue and therefore the exploitation conditions should match design requisites [5].

Loads and forces acting on quarry equipment are assumed according to relevant standards, which unfortunately do not sufficiently take into account dynamic phenomena or vibration of load-bearing elements [3, 5, 6]. Such underestimation of all load forces can lead to damage or even catastrophic failure of objects [6].

In view of these problems, we present an analysis of the causes of quarry equipment caterpillar drive shaft damage. Our analysis includes detailed numerical modelling, exploitation tests and material research.

2. Research problem

Caterpillar drive shafts are an important element of quarry equipment chassis drive trains. The problem pertains to their failure/fracture at the journal bearing area between the sprocket wheel and gear. These fractures occur at the R6 mm notch on the side of the caterpillar sprocket wheel, as shown in Figure 1.

Fig. 1. Damaged shaft – visible wear and plastic deformation

Because of the dynamic loads, especially during driving, breaking etc., it is necessary to perform appropriate fatigue calculations and to design the shaft in such a way to obtain required durability. In order to determine the cause of failure of the analyzed shafts, we have conducted a detailed strength/load/construction analysis, as well as a metallographic examination of the damaged elements.

3. Boundary condition

In order to determine the real forces acting onto the caterpillar drive shaft, we have applied a strain measurement system to record deflections at the cone-shaped area of the shaft. This area was selected because of the best access for this type of measurements. Measurements included both bending as well as torsion forces. Measurement data was collected by a controller unit mounted to the drive shaft. A view of the shaft with a strain measurement element is presented in Figure 2.

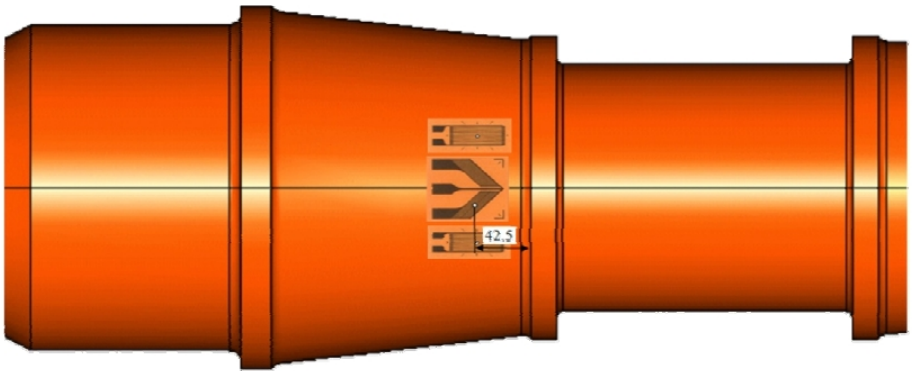

Fig. 2. Measurement point

Measurements were taken for the following types of operation: driving backwards (in the direction of the counterweight located over the reinforcement), driving forward (in the direction of the excavator wheel), braking.

These measurements were used to define the change of bending and torsion forces at the evaluated areas of the drive shaft.

4. Numerical analysis

Using the technical documentation we have created a geometrical model of the drive shaft, which then was used to create the discrete model for later numerical analysis [7].

In order to determine the strain forces (at the problem areas) occurring during exploitation, we have used the experimental results along with numerical computation. The measurement results from the test points were scaled based on the numerical model to determine the strain (dynamic change of forces) at the areas where we have observed damage. The maximum strain was consistently observed during braking of the caterpillar.

Figure 4 presents the reduced stress distribution according to the Huber-Mises hypothesis for a torsion force of Ms = 1 kNm.

For calculation of immediate strength, the maximum moment comprises of the product of the nominal moment and the engine overload factor. The maximum stress values according to the Huber-Mises hypothesis, achieved during testing were: σ_{HMH} = 651 MPa. This value was achieved during turning of the machine, where the drive overload factor was 2.26.

The object was passed also non-linear numerical analysis with the real loading conditions of the caterpillar drive shaft. Figure 5 presents the reduced stress distribution according to the Huber-Mises hypothesis for a real torsion moment in the caterpillar drive shaft.

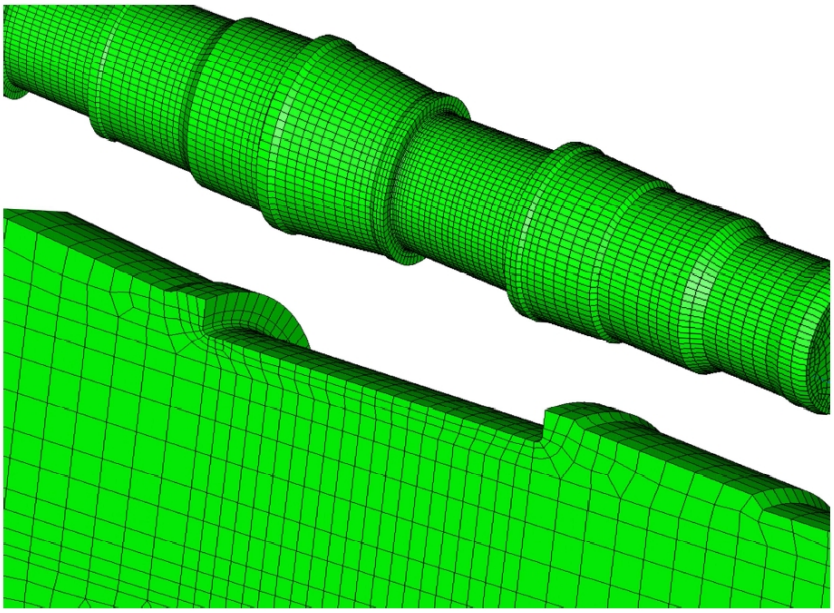

Fig. 3. Discrete model of the drive shaft

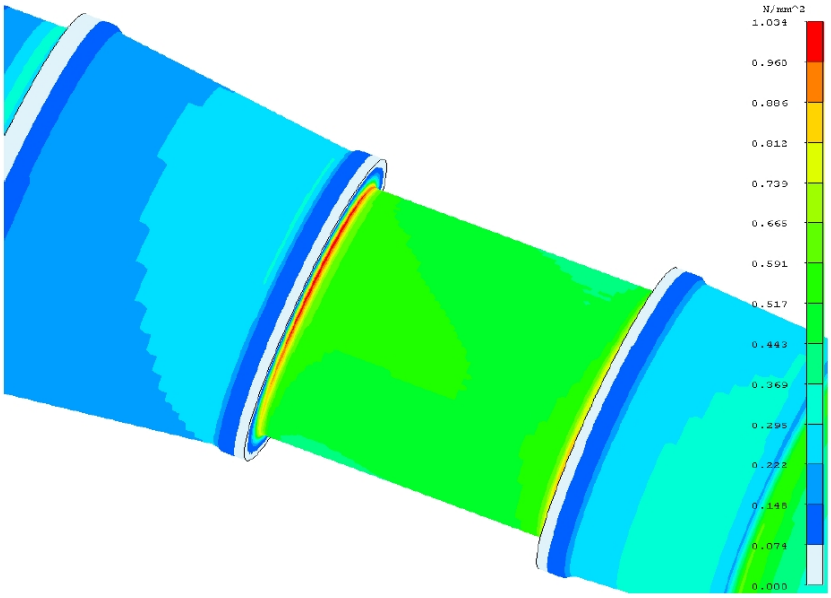

Fig. 4. Reduced stress distribution [MPa] according to Huber-Mises hypothesis for a unit torsion force of *Ms* = 1 kNm

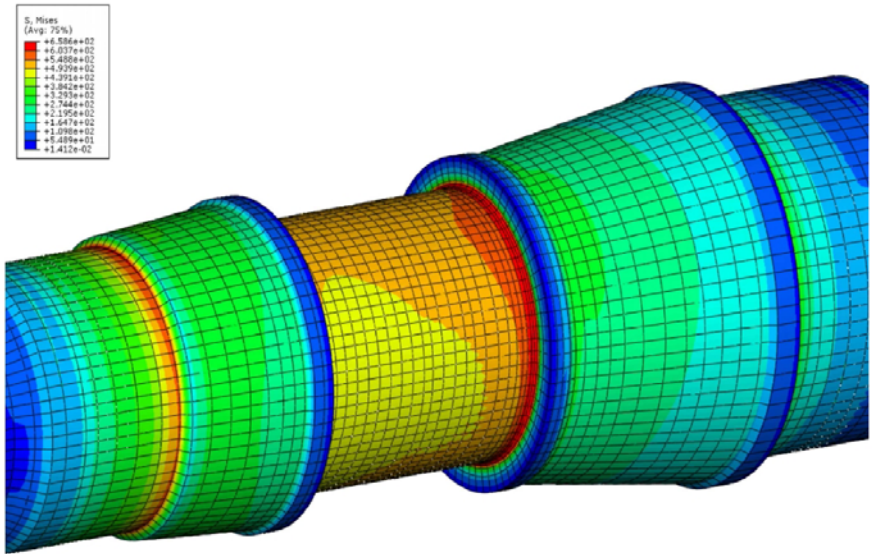

Fig. 5. Reduced stress distribution [MPa] according to Huber-Mises hypothesis for real torsion force

The maximum amplitude of stress at the notch area taking into account an overload factor (determined experimentally) of 1.71 was: σ_a = 493 MPa

The maximum allowable stress in view of fatigue stress FEM analysis, material plasticity and normal and shear forces, is: σ_a = 375 MPa

5. Analytical fatigue analysis

An analytical method was used to assess fatigue strength parameters of the material, which were:

For normal (bending) loads – FKM (2.6.1) [9]:

$$a_{BK,b} = \frac{S_{a,b}}{S_{AK,b/j_{ges}}} = 1.25 \geq 1. \tag{1}$$

For tangential (torsion) loads – FKM (2.6.1) [9]:

$$a_{BK,t} = \frac{T_{a,t}}{T_{AK,t/j_{ges}}} = 1.62 \geq 1. \tag{2}$$

For combined loads [9]:

$$a_{GH} = \sqrt{a_{BK,b}^2 + a_{BK,t}^2} = 2.05 \geq 1 \tag{3}$$

Looking at the results above, obtained through numerical [7] and analytical [9] methods, we see that the strength requirements for the area of actual damage have not been fulfilled.

6. Caterpillar shaft damage

The shaft destruction mechanism according to Friedman hypotheses can be divided on to parts: tear and shear. Then loading track scheme have two component – tension-compression (σ_s, Figure 6) and torsion (τ_s, Figure 6).

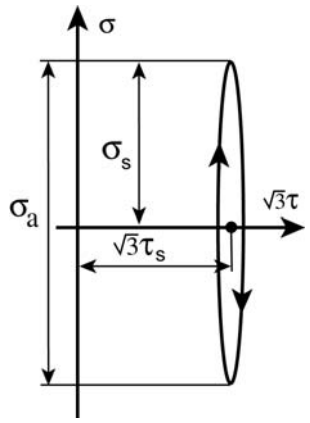

Fig. 6. Shaft loading track

Destruction mechanism is connected to micro defect initiation and growth –construction material damage. In this case damage variable is chosen in the next form [9, 10]:

$$D = 1 - \frac{\widetilde{F}}{F_0} = 1 - \frac{\widetilde{E}}{E_0}, \tag{4}$$

where:

F_0, E_0 – cross section area and Young's module for virgin material,

$\widetilde{F}$, $\widetilde{E}$ – cross section area and Young's module of damaged material.

Damage variable is feet in the range $0 \leq D \leq D_R$, where D_R – material property. When damage variable D achieve value D_R macro crack initiation take place [9].

In the case of torsion damage variable can take next form

$$D^{\tau} = 1 - \frac{\widetilde{G}}{G_0}, \tag{5}$$

where:

G_0 – Kirchhoff module for virgin material,

$\widetilde{G}$ – Kirchhoff module for damaged material.

Definition of effective stress in material σ_{ef} determines as follows:

$$\sigma_{ef} = \frac{\sigma_{\text{true}}}{1 - D}, \tag{6}$$

where:

σ_{true} – true stress.

Additional damage stress can be shown as follows [9–11]:

$$\widetilde{\sigma} = \sigma_{ef} - \sigma_{\text{true}} = \sigma_{\text{true}} \frac{D}{1 - D}. \tag{7}$$

As was shown in [12] part of damage energy for tension can be written as:

$$\Psi^{+} = \int_0^{\varepsilon_{pi}} \sigma_s \frac{D}{1 - D} d\varepsilon_p, \tag{8}$$

where:

ε_p – plastic deformation,

σ_{true} – true stress,

ε_{ip} – current plastic deformation.

Part of damage energy for compression part of loading can be written as

$$\Psi^{-} = \int_0^{\varepsilon_{pi}} \sigma_s \frac{h \cdot D}{1 - h \cdot D} d\varepsilon_p, \tag{9}$$

where:

h – parameter of compression influence on damage [12].

Part of damage energy for torsion can be written as follows:

$$\Psi^{\tau} = \int_0^{\gamma_{pi}} \tau_s \frac{D^{\tau}}{1 - D^{\tau}} d\gamma_p, \tag{10}$$

where:

D^{τ} – damage in the torsion case,

τ_S – tangent stress in the shaft,

γ_p – plastic deformation in the case of shear,

γ_{pi} – plastic deformation in the case of shear.

Then full damage energy for the shaft can be written in the next form:

$$\Psi = \Psi^{+} + \Psi^{-} + \Psi^{\tau}. \tag{11}$$

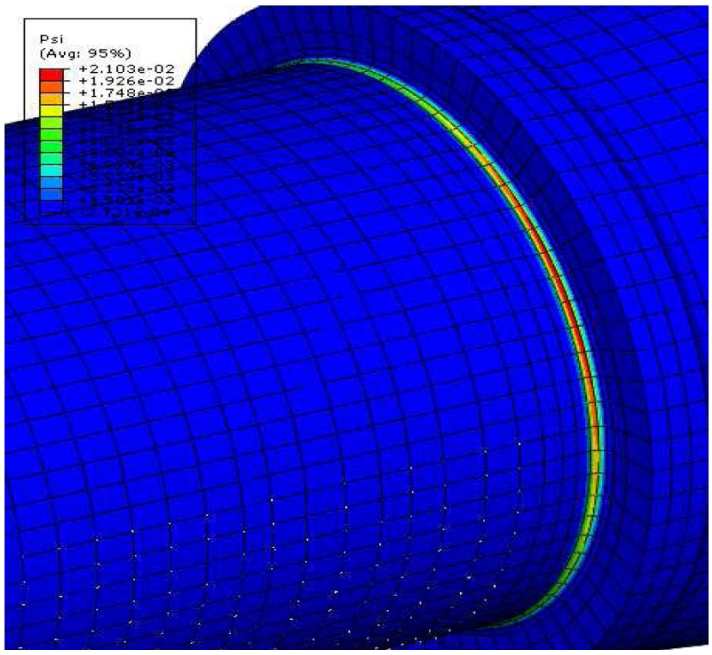

Fig. 7. Fields of damage energy Ψ in the shaft

Figure 7 presents fields of damage energy Ψ in the caterpillar drive shaft according to the Equation 12. According of the hypotheses that full work for material destruction is constant and independent of loading case [13] possible to write energetically value for damage variable:

$$\widetilde{D} = \frac{\Psi_i}{\Psi_{\max}} = \int_0^N \frac{d\Psi}{\Psi_{\max}}, \tag{12}$$

where:

$\Psi_{\max}$ – damage energy maximum is constant for material,

N – number of loading cycles.

Then energetic damage variable can be fit in the range

$$0 \le \widetilde{D} \le 1. \tag{13}$$

In the moment of time, when $N = N_R$ value $\widetilde{D} = 1$.

Then number of loading cycles [13] for destruction moment N_R can be determine in the next form:

$$N_R = \frac{d\Psi\big|_{\text{cycle}}}{\Psi_{\max}}, \tag{14}$$

where:

$d\Psi\big|_{cycle}$ – damage energy growth in the stabilized (middle) loading cycle.

Foreseeable number of work cycles the caterpillar drive shaft for definite in above – calculations conditions of work carries out 2100 cycles.

7. Metallographic examination

We have been supplied with a fragment of the damaged 270 mm shaft as shown in Figure 8, which has been earlier regenerated/resurfaced. Assessment included chemical analysis of the shaft material, (optical/microscopic) examination of the fracture as well as microstructure (optical/microscopic) examination and hardness testing.

Fig. 8. Fragment of the shaft provided for testing. Visible fatigue fracture and plastic deformation

Macroscopic examination confirmed that the shaft supplied for evaluation fractured because of fatigue, resulting from torsion force. Considering that the failure occurred during operation and that the two shaft pieces continued to rub against each other afterwards, we don't see the characteristic fatigue lines. However, it can be ascertained that this is fatigue fracture, based on the fatigue area distributed evenly around the shaft's cross section (45–50 mm from the surface) as well as based on the smoothness of this area. The middle part of the fracture's cross-section exhibits strong plastic deformation resulting from torque as well as expanded surface topography.

We have noted numerous grid-line fractures and surface imperfections (smooth indentations) on the shaft's surface (Figure 8). The arrows in Figure 8 above point to some of the fractures on the surface.

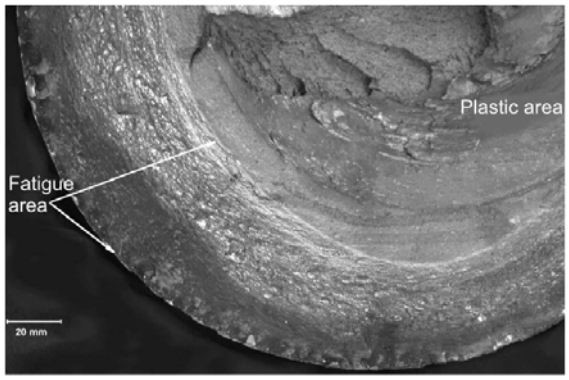

Fig. 9. Magnified image of the fracture area presented earlier in Figure 8. View of the worn down fatigue zone and the plastic deformation area

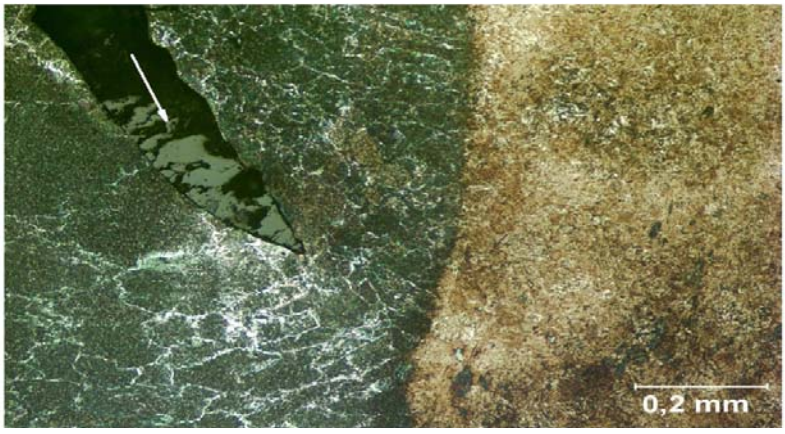

Fig. 10. Microstructure of the padding welds. Clearly visible welding defect – lack of penetration and seam filled with slag. Quasieutectoid – perlite structure in the padding weld and martensite in HAZ. Mi1Fe etching and visual (optical microscope) examination

A sample for microstructure assessment was taken from a lateral cross-section of the shaft – at the spot marked with a rectangle and symbol "A" in Figure 8. Microscopic evaluation proved that the shaft was improperly resurfaced. The distance between subsequent seams is too large, resulting in improper overlap and also insufficient weld penetration and incomplete fusion. The results of microscopic investigations of metallographic samples received from the caterpillar drive shaft were represented in the Figures 10–12.

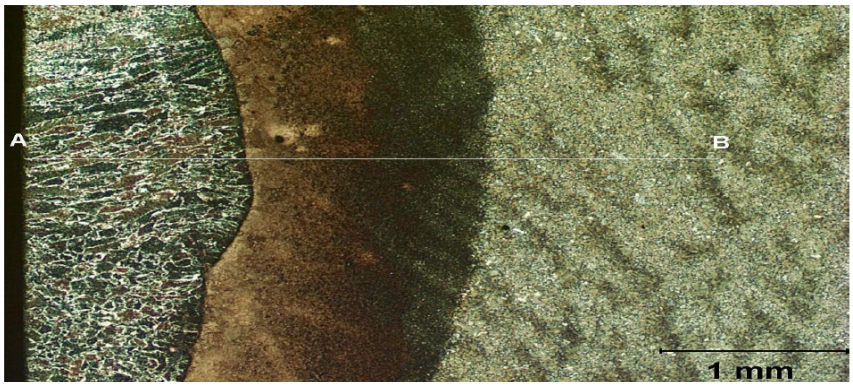

Fig. 11. Microstructure of the padding welds. Visible rapid transfer between the HAZ and base material. We have performed detailed hardness measurements along the 'A-B' line. Mi1Fe etching and visual (optical microscope) examination

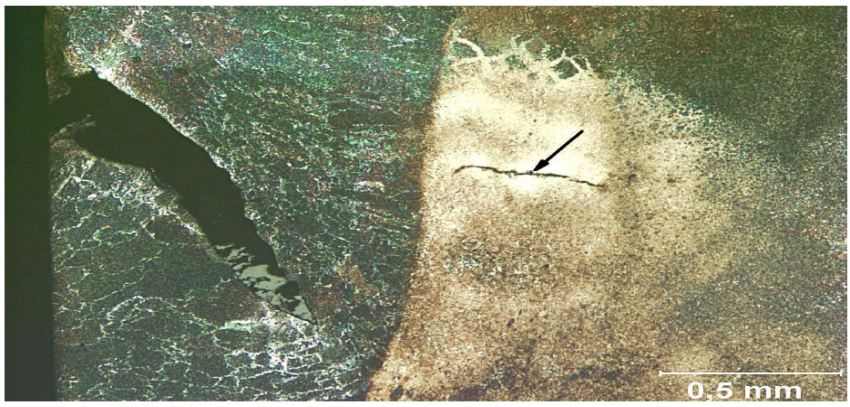

Fig. 12. Microstructure of the padding welds. Visible fractures in the HAZ – marked with an arrow, as well as a welding defect – seam filled with slag. Mi1Fe etching and visual (optical microscope) examination

Hardness measurements of the padding weld, HAZ and base material has been performed on the shaft's surface, along the "A-B" line, marked in Figure 11.

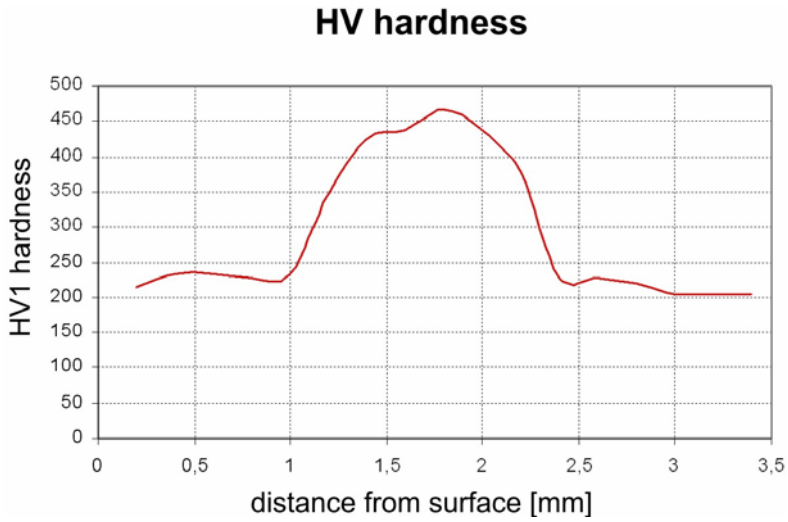

Fig 13. Padding weld, HAZ and base material hardness

The hardness measurements showed that hardness in the HAZ (heat affected zone) exceeds the maximum allowable value of 350 HV, reaching even 467 HV. This shows that the HAZ became hardened, which leads to quenching fractures. The transfer area between the padding weld, HAZ and the base material exhibits rapid change in hardness, which creates a structural notch area prone to further cracking and fractures.

8. Conclusions

The paper presents examples of fatigue stress fractures of quarry equipment drive shafts. In order to determine the real cause of this damage, we have performed a detailed analysis of the problem. By integrating experimental methods and FEM analysis we were able to define the actual strain forces acting onto the drive shaft. Then, using a numerical model of the shaft and rescaled strain measurement results, we were able to plot the strain forces for the areas of interest for the test object. Based on the obtained information, we were able to define the strength and durability parameters for the analyzed object. An analytical method was also used to assess durability for the purpose of comparison. Further analysis included metallographic examination of a fragment of a damaged shaft. This inspection confirmed the earlier stipulations, regarding damage/fractures of these elements.

The major, direct cause of quarry equipment caterpillar drive shaft fractures is the improper shape at the journal bearing area, which leads to overload in view of the immediate strength and fatigue stress occurring at the actual exploitation load levels. Based on metallographic inspection, it can be concluded that the fracture of the shaft occurred because of torsion fatigue stress. The area of fracture was then smoothed out

because the two parts of the shaft continued to rub against each other after the fracture occurred. The fracture zone also exhibits plastic deformation. An indirect cause of the damage can also be attributed to improper resurfacing of the shaft, which caused hardening of the HAZ and development of a martensite structure.

The presented combined experimental/numerical approach to the research problem allowed for full identification of strength and fatigue characteristics along with the causes of damage of the analyzed elements.

References

[1] Kocańda S., Szala J.: *Basics of fatigue calculations*, PWN, 1998.
[2] *Basis of construction of machines under*, red. Marka Dietricha, Warszawa, Publishers Scientifically – Technical, 2006.
[3] Dudek D.: *Elements of dynamics of machines of mining opencast, Canvassing of signals, Analysis of systems*, Wrocław University of Technology, Wrocław, 1994.
[4] Blicharski M. et al.: *Poland metallurgy in the years 1998–2002*, Kraków, 2002.
[5] DIN 22261-2 1997 – *Bagger Absetzer und Zusatzgeräte in Braunkohlentagebauen*.
[6] Babiarz S., Dudek D.: *Chronicle Of damage and of disasters of basic machines in Polish opencast mining*, Wrocław University of Technology, Wrocław, 2007.
[7] Rusiński E., Czmochowski J., Smolnicki T.: *Advance finite method analysis*, Wrocław University of Technology, 2005.
[8] FKM – Guideline, *Analytical Strength Assessment of Components in Mechanical Engineering*, 5th, revised edition, English Version, Forschungskuratorium Maschinenbau (FKM), Frankfurt/Main, 2003.
[9] Lemetr J.: *A Course on Damage Mechanics*, Springer Verlag, Germany, 1992, pp. 210.
[10] Kachanov L.M.: *Basis of rupture mechanic*, Moscow, Since, 1974, 312c.
[11] Lemetr J.: *Damage mechanics*, The Bath Press, Great Britain, 1990, pp. 556.
[12] Bobyr N.I., Yakhno B.O., Grabovski A.P.:, *Damage Accumulation of Structural Materials under Complex Low – Cycle Loading*, Strength of Materials, The International Journal, Ukraine, 6, 2007, pp. 25–35.
[13] Yakhno B.O.: *Damage and destruction of construction materials during complex low- cycle loading*, Manuscript, PhD Thesis, NTUU "KPI", Kiev, Ukraine, 2005.

Analiza przyczyn zniszczenia wałów napędowych pojazdów gąsienicowych

W artykule przedstawiono eksperymentalno-numeryczne podejście do problemu analizy przyczyn uszkodzeń wałów napędowych pojazdów gąsienicowych maszyn podstawowych górnictwa odkrywkowego. Przedstawiono wyniki badań eksperymentalnych, analiz numerycznych i badań metalograficznych.

ARCHIVES OF CIVIL AND MECHANICAL ENGINEERING

Vol. VIII 2008 No. 3

Experimental study with a Digital Image Correlation (DIC) method and numerical simulation of an anisotropic elastic-plastic commercially pure titanium

F. TOUSSAINT, L. TABOUROT, P. VACHER
Laboratoire SYMME, Polytech'Savoie, BP 80439, 74944 Annecy le Vieux Cedex, France

In this paper, the tensile behaviour of a commercially pure titanium is studied using a full-field strain measurement. A fine analysis of the measured strain fields is carried out in order to determine the intrinsic behaviour of the material. An elastic-plastic model taking material anisotropy into account is proposed. On the basis of experimental results, the parameters of this model are identified then introduced into a FEM code in order to simulate the behaviour of titanium. To assess the performance of the approach, the numerical results are finally analysed and compared with measurements coming from image processing. A quite satisfactory agreement between simulation and experiment is obtained.

Keywords: *mechanical testing, full-field measurement, anisotropic material, finite elements, titanium*

1. Introduction

Commercially pure (CP) titanium is a metal having several interesting physical properties: its density (ρ = 4.5 kg/m3) is 40% lower than that of carbon steels, it is non-magnetic, its aptitude to be passivated by the formation of a protective oxide film confers to it an exceptional resistance to corrosion, its biocompatibility is markedly higher than that of other metals (e.g. stainless steels). Because of all these characteristics, commercially pure titanium finds many applications and more specifically in the medical sector, in particular in orthodontic and orthopaedic appliances.

So far, research has been devoted to improve the mechanical properties of the material [1, 2], study the material behaviour in corrosion [3–5], analyse its friction resistance [6, 7]. In contrast with the significant number of studies concerned with the intrinsic properties of the material, the literature relating to the rheological properties and the numerical simulation of CP titanium forming operations is much scarce and incomplete [8–13]. However, a better knowledge of the stress-strain relation of CP titanium could contribute to improve rheological models integrated in the finite element code, the results of simulations being helpful in the optimisation of the manufacturing process of a new prosthesis, for example.

Among these former studies, Salem et al. [8] propose an interesting model of crystalline plasticity. This model is suitable to predict the anisotropic behaviour in terms of stress-strain relations as well as evolution of texture of commercially pure titanium. While this kind of modelling has significantly improved the understanding of material

deformation, computation is time- consuming for industrial forming operations such as deep-drawing for example.

The recent work of Fuh-Kuo and Kuan-Hua [13] dedicates to stamping formability of commercially pure titanium sheet metal is also very interesting from an experimental point of view. The mechanical behaviour of CP titanium sheets is studied from a significant number of tensile tests carried out at various temperatures ranging from ambient to 300 ºC and at various strain rates from 0.1 to 0.0001 s^{-1}. Tests are carried out on samples cut out in a 0.5 mm thick sheet along three different directions (0º, 45º and 90º) following the rolling direction. An anisotropic behaviour is highlighted and a behaviour independent to the strain rate is observed when $\dot{\varepsilon}$ is lower than 0.001 s^{-1}. However, in spite of the precious information underlined by this work, no rheological model is proposed to describe the behaviour of commercially pure titanium.

It appears from the previous discussion that a finer experimental analysis is needed to model and simulate the behaviour of commercially pure titanium. This point constitutes the main objective of this contribution. The behaviour of commercially pure titanium is studied from various tensile tests. The deformations of the sample are measured with a Digital Image Correlation (DIC) method presented in Section 2. A fine analysis of the results is carried out in Section 3 in order to determine the intrinsic behaviour of the material. The anisotropy resulting from the operation of rolling performed on the sheets during their industrial elaboration and from the crystallographic structure of the material is also highlighted. In Section 4, the constitutive equations of an elastic-plastic model taking this anisotropy into account are proposed. The material parameters of the model are determined from experimental data then introduced into a commercial finite element code. The numerical simulation results of CP titanium deformation under tensile loading are finally analysed and discussed in Section 5.

2. Experimental procedure

2.1. Material

Provided by ACNIS International (France), the studied material is a Commercially Pure (CP) titanium grade 2 (of French denomination T40). The limits of the chemical composition of the material are described in Table 1.

Table 1. Chemical composition limits of commercially pure titanium grade 2

Element	Ti	C	Fe	N	O	H
Weight (%)	bal.	0.10	0.30	0.03	0.25	0.015

As the material has been rolled during its industrial elaboration, we note by DL the rolling direction and DT the transverse direction. The samples tested are cut out using a wire cutting machine in a 0.5 mm thick sheet following three different directions (0º, 45º and 90º) from the rolling direction DL (Figure 1).

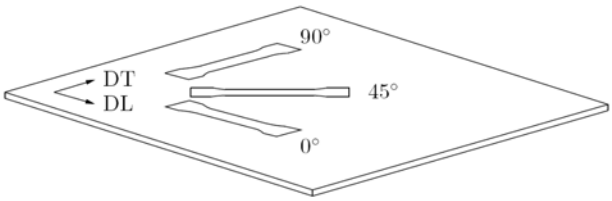

Fig. 1. Position following the rolling direction (DL) of various tensile samples in the sheet

2.2. Tensile test with full-field strain measurement

Tests are performed on a tensile testing machine INSTRON^{TM} 4569 with a load cell of 50 kN and the Merlin acquisition software. These tests are carried out at a constant crosshead speed V = 2 mm/min corresponding to a mean strain rate $\dot{\varepsilon}$ equal to approximately 1×10^{-3} s^{-1}. The deformations of samples are measured using an Digitial Image Correlation (DIC) method (Figure 2).

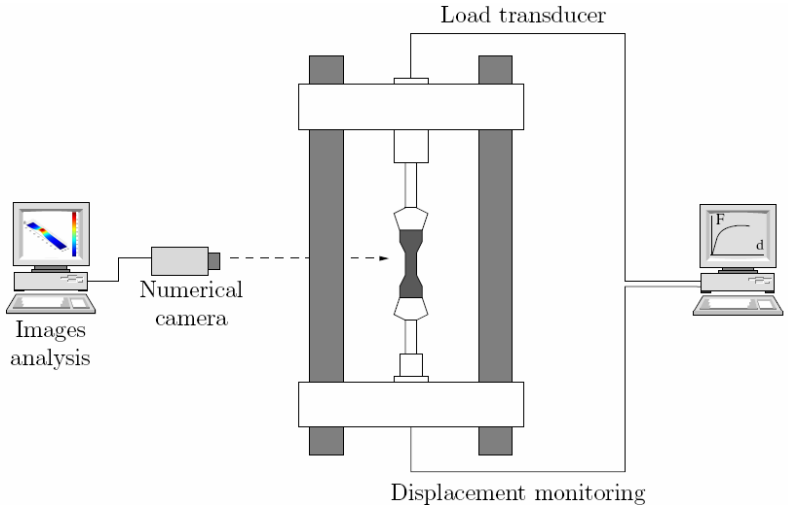

Fig. 2. Chain of numerical acquisition used during tensile tests

A face of the sample is painted with both white and black colour sprays in order to create a surface with a random grey level. During test, a digital camera (HAMAMATSU C4742-95) facing perpendicularly to the sample, records several images with a resolution of 1280 × 1024 pixels. The interval of time between each image is set at 4 seconds. About a hundred images are thus created when the test is carried out until the sample breaks. Measurements of displacements on the surface of the sample and calculations of kinematic fields are performed from the image processing software "7D" whose principle is based on a DIC method [15]. Within the software, an area of

study on the initial image is manually defined with the mouse. In this zone, we define a grid and a mask. The displacements determined by the correlation between the initial image will be represented at each node of the grid. The size of the mask is independent of the step of the grid. The search of a correspondent between two images is obtained by comparing the grey levels of the mask. This information analysed by the software makes it possible to define the components u and v of the displacement field on the surface of the sample. Within the "7D" software, these components take the following bilinear form:

$$\begin{cases} u = a_1 x + b_1 y + c_1 xy + d_1 \\ v = a_2 x + b_2 y + c_2 xy + d_2 \end{cases}, \tag{1}$$

where a_i, b_i, c_i and d_i, i = (1, 2) are constants determined by minimisation of the correlation coefficient. The "raw" information measured during a tensile test using this technique of image processing is shown in Figure 3.

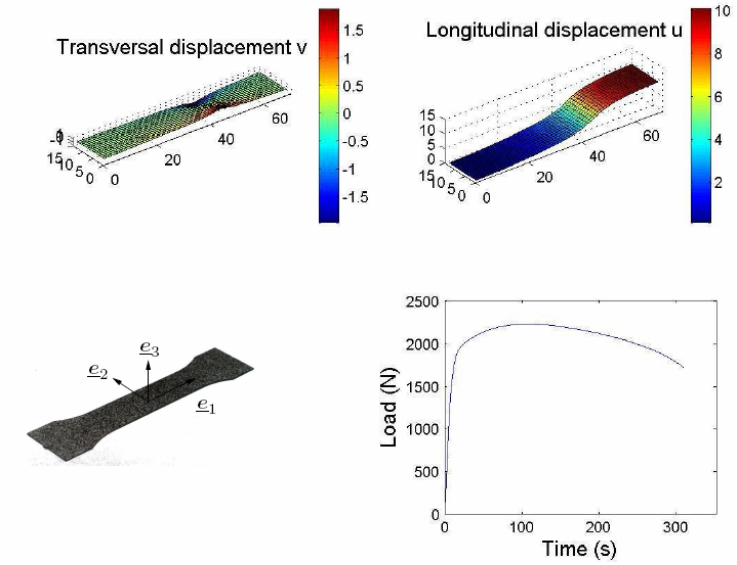

Fig. 3. Results of a tensile test with full-field measurements (fields of longitudinal u and transversal v displacements before rupture; load versus time curve)

For this test, the grid of analysis consists of 69 × 14 quadrilaterals of 10 by 10 pixels, which corresponds to an area of analysis of approximately 405 mm^2. The extensometric base is a square of 10 by 10 pixels. The fields of displacement obtained by image processing highlight heterogeneous transverse displacements v where the necking occurs and almost constant longitudinal displacements u on each line of analysis.

The force F grows up to a maximum value of 2200 N. Then, sample deformations are accompanied by the phenomenon of necking. This phenomenon brings the decrease of force values down to 1700 N corresponding to the rupture of the sample.

2.3. Stress-strain relation

In the case of a Lagrangian description, strain measurements are generally expressed from the gradient $\underline{\underline{F}}$ of the transformation according to the relation $\underline{\underline{\varepsilon}} = \frac{1}{2}\ln \underline{\underline{C}}$ with $\underline{\underline{C}} = \underline{\underline{F}}^t \underline{\underline{F}}$ where $\underline{\underline{C}}$ is the elongation tensor and $\underline{\underline{\varepsilon}}$ represents the logarithmic or Hencky strain tensor. Insofar, as displacements are calculated only on the surface of the sample (i.e. in the plane $(\vec{e}_1, \vec{e}_2)$), only the components ε_1 and ε_2 of the logarithmic strain tensor are available. If the hypothesis of isochoric deformation of metallic materials is admitted ($\varepsilon_v = \ln(V/V_0) = 0$), the component ε_3 can be calculated according to the relation: $\varepsilon_3 = -(\varepsilon_1 + \varepsilon_2)$. The suitable definition of stresses associated with Hencky strains is given by the Cauchy stress tensor. In the case of a tensile test performed according to direction $\vec{e}_1$, the component σ_1 is expressed as: $\sigma_1 = F/S$ where F is the applied load and S the current section of the sample. It is then easy to determine this last component since width l and thickness e of the sample can be calculated from the deformations ε_2 and ε_3 according to the formulas: $l = l_0 \times \exp(\varepsilon_2)$ and $e = e_0 \times \exp(\varepsilon_3) = e_0 \times \exp(-\varepsilon_1 - \varepsilon_2)$ where l_0 and e_0 are respectively the initial width and thickness of the sample. Although corrections can be made (Bridgman correction for example), we consider that the effective stress is appreciably of the same order of magnitude as the component σ_1.

3. Experimental results

3.1. Necking localization

The procedure presented above was first applied to a CP titanium specimen following a direction at 0º, i.e. parallel to the rolling direction. The grid of image processing of the deformed sample as well as some numbers of the lines around the necking area are presented in the Figure 4b.

The line numbers correspond to equidistant sections of a value equal to the step of the grid, i.e. 10 pixels that is to say approximately 0.65 mm. Figure 4a highlights the corresponding true stress-logarithmic strain curves. The material response is not the same in all the sections. The curves leading to a maximum value of strain and where the work hardening is always positive are those where the necking is the most important (sections nº25 and 26). The further we move away from this zone, the less important the deformations are. The stress-strain curves have a similar shape to the curve representating the evolution of the force (Figure 3). In the following study, as the in-

trinsic material behaviour is obtained around necking, the behaviour for CP titanium will be represented by the stress strain curve nº26 in Figure 4.

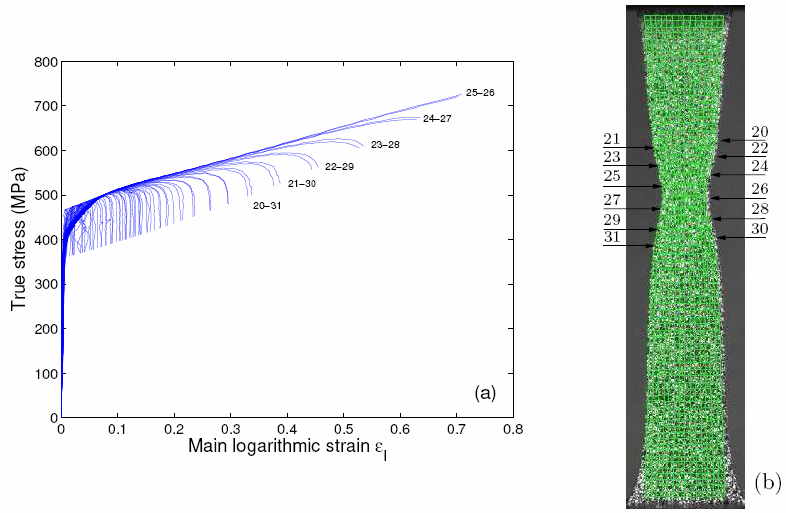

Fig. 4. Mechanical response of CP titanium for a monotonic tensile loading:
(a) true stress versus main logarithmic strain curves for different lines of analysis,
(b) position of these lines on the grid of analysis before rupture

3.2. Anisotropy

The anisotropy of materials in the form of sheets is generally characterized by anisotropic coefficients also called Lankford coefficients. They are defined by the ratio of plastic strain rates transversal ($\dot{\varepsilon}_{22}^{p}$) and normal ($\dot{\varepsilon}_{33}^{p}$) to sheet plan:

$$r(\theta) = \frac{\dot{\varepsilon}_{22}^{p}}{\dot{\varepsilon}_{33}^{p}}. \tag{2}$$

For many metal alloys, this coefficient remains constant according to the deformation. From an experimental point of view, these coefficients are given from the slope of the straight line of the representation of ε_{22}^{p} according to ε_{33}^{p} measured during a tensile test. Figure 5 presents these curves for three tests carried out on samples cut into the titanium sheet at 0º, 45º and 90º following the rolling direction.

The values of the coefficients r_0, r_{45} et r_{90} are identified by fitting a linear law of regression on experimental data. These values shown in Table 2 lead to an average coefficient $r = (r_0 + 2\ r_{45} + r_{90})/4 = 4.59$. This value higher than the unit is significant of a material having a good formability.

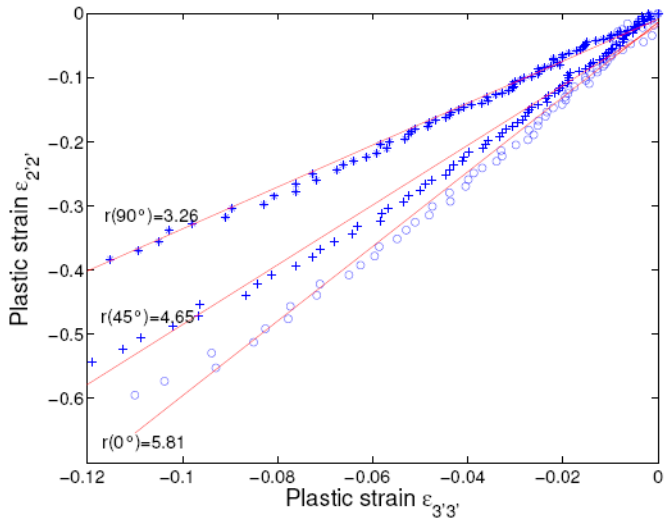

Fig. 5. Lankford coefficients

Table 2. Lankford coefficients for a CP titanium sheet of 0.5 mm thick

Material	r_0	r_{45}	r_{90}	$\bar{r}$
CP titanium	5.81	4.65	3.26	4.59

4. Modelling and parameter identification

4.1. Constitutive equations

From the experimental results presented above, we present in this section the constitutive equations to model the behaviour of commercially pure titanium. Our model is composed of i) a linear isotropic elastic behaviour law (Young's modulus, Poisson's ratio), ii) a plastic behaviour defined by a plastic criterion with an associated flow rule identified by an initial yield surface and a work hardening law. It has been previously shown that the commercially pure titanium used in a metal sheet is a material which, because of its crystallographic structure and forming operations undergone during its elaboration, in particular rolling, presents an anisotropic behaviour. This anisotropic behaviour can be modelled from a plastic point of view by Hill's criterion [16] whose expression is given by the following equation:

$$\sigma_{eq} = f(\underline{\underline{\sigma}}) = \left(\frac{1}{2}\left(F(\sigma_{22}-\sigma_{33})^2 + G(\sigma_{33}-\sigma_{11})^2 + H(\sigma_{11}-\sigma_{22})^2 + 2L\sigma_{23}{}^2 + 2M\sigma_{31}{}^2 + 2N\sigma_{12}{}^2\right)\right)^{\frac{1}{2}},$$

where F, G, H, L,M, N are material parameters characterizing the anisotropy. In the case of a material in the form of metal sheet for which the assumption of plane stress

is acceptable, this criterion amounts to an expression having only 4 parameters F, G, H and N since $\sigma_{i3} = 0$. In addition to that yield surface, various work hardening laws for analysing, simulation and design processes of metallic material are commonly used [17]. Here, the Ludwick law whose equation is given by:

$$\sigma_p = \sigma_e + K\varepsilon_p^n, \tag{4}$$

where σ_e is the initial yield stress and K, n are material parameters, is used because this relation between the plastic yield stress σ_p and the equivalent plastic strain ε_p gives the best fit.

4.2. Material parameters

In the constitutive equations introduced into the previous section, nine material parameters are involved, i.e. Young's modulus E, Poisson's ratio ν, parameters K, n and the elastic limit σ_e of the power law as well as 4 coefficients F, G, H and N of the Hill criterion. The different parameter values are reported in Table 3.

Table 3. Material parameters of CP titanium relative to the constitutive equations

Parameters	E (MPa)	ν	σ_e (MPa)	K (MPa)	n	**F**	**G**	**H**	**N**
Value	111819	0.34	368	375	0.44	0.52	0.29	1.70	4.20

Young's modulus of material is identified from a tensile test with conventional strain measurement (i.e. axial extensometer INSTRON 2620-601). In the literature, the commonly encountered value of Young's modulus is equal to about 110000 MPa, which corresponds to a relative error of approximately 1.5% in regard to the measured value. A value of ν = 0.34 for Poisson's ratio is kept without experimental checking. The parameters of the Ludwik law are fitted to the experimental measures. To ensure the agreement between the theoretical law and experimental results, the evolution of the equivalent plastic stress versus the equivalent strain is depicted in Figure 6. The full line and the crosses correspond respectively to the law and the experimental results. A rather satisfactory agreement is obtained between the law and the experiment. The determination of Hill's coefficients is based on a method which was presented by Rees [18, 19]. By considering the assumption of generalized normality and a sample submitted to a uniaxial tensile loading following an angle θ compared to the unit vector $\vec{e}_1$, a generalized anisotropic coefficient depending only on the coefficients of Hill is given by the relation:

$$r(\theta) = \frac{H + (2N - F - G - 4H)\cos^2\theta \sin^2\theta}{F\sin^2\theta + G\cos^2\theta}. \tag{5}$$

In addition to Equation (10), the yield stress of plastic flow resulting from a uniaxial tensile test according to a direction θ is written as:

$$\frac{\sigma_{eq}}{\sigma'} = \left[\frac{1}{2}\left(F\sin^2\theta + G\cos^2\theta + H + (2N - F - G - 4H)\cos^2\theta\sin^2\theta\right)\right]^{\frac{1}{2}}. \tag{6}$$

Since three tensile tests are carried out with $\theta = 0$, 45 and 90º and if the yield stress of plastic flow following the rolling direction σ_0 is considered as reference, the identification of Hill's coefficients consists in the resolution of the following system of equations:

$$\begin{cases} \frac{1}{2}(G+H) - \frac{\sigma_{eq}}{\sigma_0} = 1 \\ Gr_0 - H = 0 \\ Fr_{90} - H = 0 \\ (F+G)(2r_{45}+1) - 2N = 0 \end{cases}. \tag{7}$$

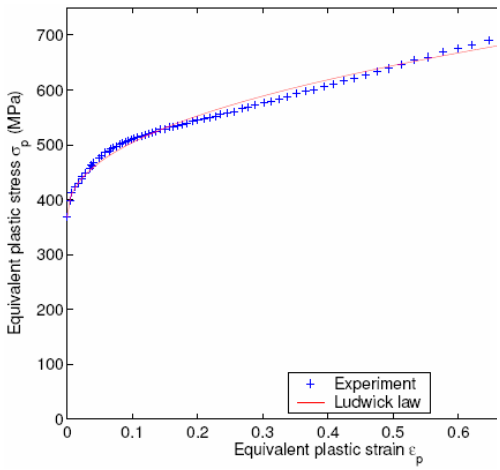

Fig. 6. Comparaison between experimental results and the prediction of the Ludwick law

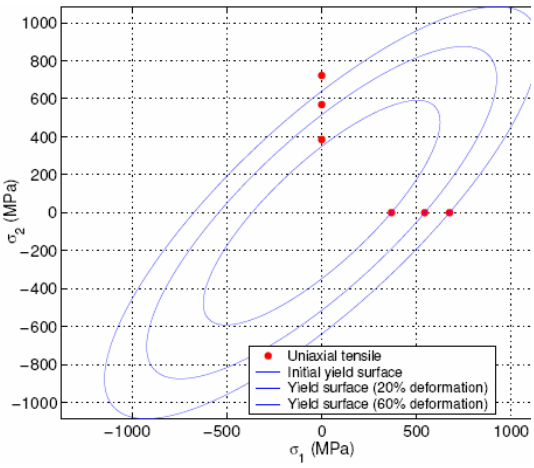

Fig. 7. Hill's yield surface for a CP titanium

Figure 7 shows the results of this identification. The points correspond to the experimental yield stresses for the tensile tests carried out with $\theta = 0$º and 90º. Corresponding surfaces are plotted in full feature. A small difference between theoretical surfaces and the experimental points coming from the tensile test at $\theta = 90$º can be noticed. The error made on the value of stress is equal to about 10%.

5. Numerical simulation

5.1. Simulation of tensile tests

This section shows the ability of the present approach to simulate the anisotropic elastic-plastic behaviour of a CP titanium. The numerical simulations are performed within the commercial finite element code ABAQUS. The meshing of the sample and the boundary conditions of the test are presented in Figure 8. The meshing of the central area of the tensile sample consists of 884 S4R shell elements 0.5 mm thick. It is performed so that the number of nodes is the same as the number of measurements from the experimental grid of image processing, i.e. 966 measurements. Nodes at the right end of the sample are blocked along the axis of traction, those at the left end are subjected to an imposed displacement of 10.6 mm. The material parameters for the simulation are those given in Table 3 of Section 4.2. Calculations are carried out in quasi-static conditions insofar as the kinetic energy of the sample is lower than internal energy (approximately 20 times lower).

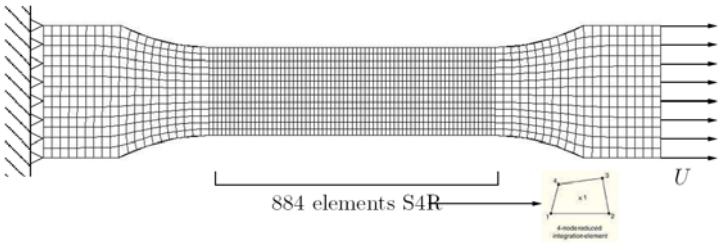

Fig. 8. Meshing and boundary conditions of the tensile test sample

5.2. Numerical results and comparison

The deformed shape of the sample obtained at the end of the simulation and the image taken during the tensile test at 0º for the same value of displacement are presented in Figure 9 to give a qualitative comparison between FEM analysis and experiments.

Figure 10 presents numerical and experimental longitudinal displacement fields resulting from the same test. A quite satisfactory agreement between numerical and experimental results is noted either if the numerical strain field is more diffuse than the experimental one. In order to quantify the real ability of the numerical tool to predict the behaviour of CP titanium and in particular the necking phenomenon, experimental and simulated evolution of necking width for the three tests are depicted in Figure 11.

The necking width is calculated as the ratio of the current width of the sample at the necking on the initial width. The starting value is also equal to one. A quite satisfactory agreement can be noted since for the tests with 0 and 90° the made relative error remains lower than 2% while for the test with 45° this value is a little bit higher (12%).

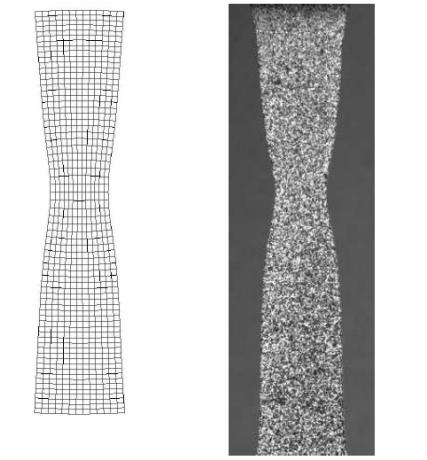

Fig. 9. Qualitative comparison between FEM deformed mesh and experimental deformed part

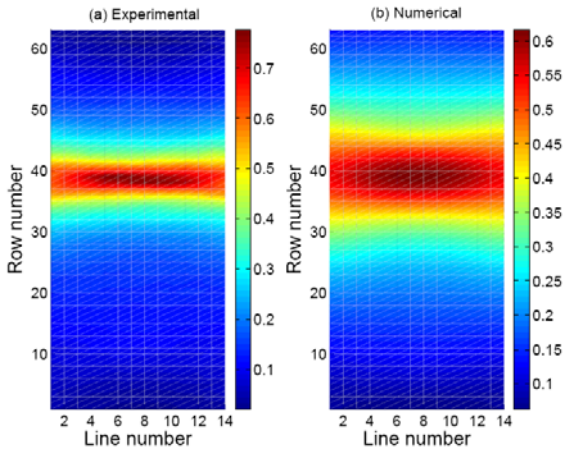

Fig. 10. Comparison between numerical and experimental strain fields

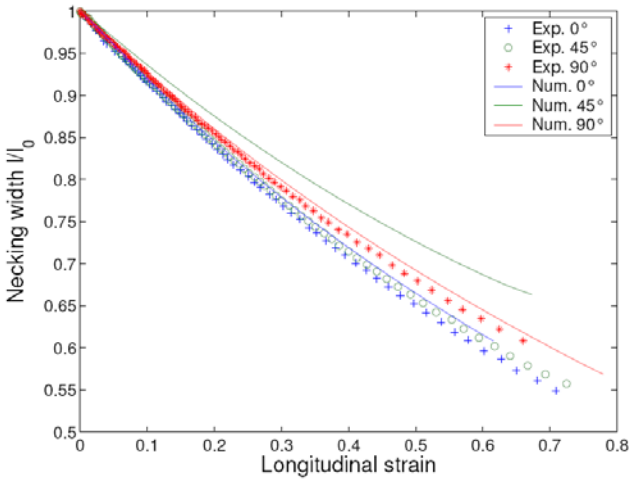

Fig. 11. Experimental and predicted evolution of necking width during a tensile test for three different samples (0º, 45° and 90º)

6. Conclusion

In order to model and simulate the anisotropic elastoplastic behaviour of a commercially pure titanium, a full-field strain measurement was used during various tensile tests. The strain fields calculated with this method highlight a heterogeneity of

strains increasing during tests. A fine analysis of the results makes it possible to determine the intrinsic stress-strain relation of the material. The anisotropic behaviour of titanium sheets due to their crystallographic structure and to the post-forming rolling operation was characterised in terms of anisotropic coefficients. The elastic-plastic model proposed and used to simulate the anisotropic behaviour of titanium gives, in comparison with measurements coming from image processing, satisfactory results. This approach provides an interesting simulation tool to design and optimise biomedical implants restricted to sheet metal formability [20].

References

[1] Nagasekhar A., Chakkingal U., Venugopal P.: *Candidature of equal channel angular pressing for processing of tubular commercial purity-titanium*, Journal of Materials Processing Technology, 173, 2006, pp. 53–60.
[2] Simbi D., Scully J.: *The effect of residual interstitial elements and iron on mechanical properties of commercially pure titanium*, Materials Letters, 26, 1996, pp. 35–39.
[3] Cheng X., Roscoe S.: *Corrosion behavior of titanium in the presence of calcium phosphate and serum proteins*, Biomaterials, 26, 2005, pp. 7350–7356.
[4] Koike M., Cai Z., Fujii H., Brezner M., Okabe T.: *Corrosion behavior of cast titanium with reduced surface reaction layer made by a face-coating method*, Biomaterials, 24, 2003, pp. 4541–4549.
[5] Gonzalez J., Mirza-Rosca J.: *Study of the corrosion behavior of titanium and some of its alloys for biomedical and dental implant applications*, Journal of Electroanalytical Chemistry, 471, 1999, pp. 109–115.
[6] Stolyarov V., Shuster L., Migranov M., Valiev R., Zhub Y.: *Reduction of friction coefficient of ultrafine-grained cp titanium*, Materials Science and Engineering, A 371, 2004, pp. 313–317.
[7] Grenier M., Dubé D., Adnot A., Fiset M.: *Microstructure and wear resistance of CP titanium laser alloyed with a mixture of reactive gases*, Wear, 210, 1997, pp. 127–135.
[8] Salem A., Kalidindi S., Semiatin S.: *Strain hardening due to deformation twinning in α-titanium: Constitutive relations and crystal-plasticity modeling*, Acta mater., 53, 2005, pp. 3495–3502.
[9] Nemat-Nasser S., Guo W., Cheng J.: *Mechanical properties and deformation mechanisms of a commercially pure titanium*, Acta mater., 47, 1999, pp. 3705–3720.
[10] Fundenbergert J., Philippe M., Wagner F., Esling C.: *Modelling and prediction of mechanical properties for materials with hexagonal symmetry (zinc, titanium and zirconium alloys)*, Acta mater. 45, 1997, pp. 4041–4055.
[11] Reed-Hill R., Iswaran C., Kaufman M.: *A power law model for the flow stress and strain-rate sensitivity in CP titanium*, Scripta Metallurgica and Materialia, 33, 1995, pp. 157–162.
[12] Shen H., Oppenheimer S., Dunand D., Brinson L.: *Numerical modelling of pore size and distribution in foamed titanium*, Mechanics of Materials, 38, 2006, pp. 933–944.
[13] Fuh-Kuo C., Kuan-Hua C.: *Stamping formability of pure titanium sheets*, Journal of Materials Processing Technology, 170, 2005, pp. 181–186.

[14] Dumoulin S., Tabourot L., Chappuis C., Vacher P., Arrieux R.: *Determination of the equivalent stress-equivalent strain relationship of a copper sample under tensile loading*, Journal of Materials Processing Technology, 133, 2003, pp. 79–83.
[15] Vacher P., Dumoulin S., Morestin F., Mguil-Touchal S.: *Bidimensional strain measurement using digital images*, Proc. Inst. Mech. Eng., 213, 1999, pp. 811–817.
[16] Hill R.: *A theory of the yielding and plastic flow of anisotropic metals*, Proc. Roy. Soc. Lond., A193, 1948, pp. 281–297.
[17] Gronostajski Z.: *The constitutive equations for FEM analysis*, Journal of Materials Processing Technology, 106, 2000, pp. 40–44.
[18] Rees D.: *Plastic flow in the elliptical bulge test*, Int. J. Mech. Sci. 37, 1995, pp. 373–389.
[19] Rees D.: *Sheet orientation and forming limits under diffuse necking*, Appl. Math. Modelling., 20, 1996, pp. 624–635.
[20] Toussaint F., Tabourot L., Ducher F.: *Experimental and numerical analysis of the forming process of a CP titanium scoliotic instrumentation*, Journal of Materials Processing Technology, In Press, Accepted Manuscript, 2007.

Doświadczalne badania w zakresie sprężysto-plastycznym handlowo czystego tytanu za pomocą metody korelacji obrazu cyfrowego oraz symulacji numerycznej

Podczas prób rozciągania blachy z handlowo czystego tytanu badano rozkład odkształceń za pomocą analizy obrazu i identyfikacji położenia przez korelację kontrastu. Metoda pozwoliła na wyznaczenie odkształceń podczas rozciągania na całej powierzchni próbki, łącznie ze strefą przewężenia, dla trzech kierunków rozciągania. Na podstawie pomiarów wyznaczono krzywe umocnienia, współczynniki anizotropii oraz przedstawiono równania konstytutywne badanego materiału, obejmujące izotropowy zakres sprężysty oraz anizotropowy zakres plastyczny. Do opisu właściwości anizotropowych zastosowano warunek Hilla z 1948 r. Poprawność modelu oceniono na podstawie modelowania MES próby rozciągania.

ARCHIVES OF CIVIL AND MECHANICAL ENGINEERING

Vol. VIII 2008 No. 3

Analysis of the perforation process of steel strips used in automotive industry

K. ŻABA, W. MUZYKIEWICZ, S. NOWAK
AGH University of Science and Technology, Al. Mickiewicza 30, 30-059 Kraków, Poland

The paper shows the results of the study of manufacturing and processing of perforated steel strips used in automotive industry. Published results include examination of the strips after perforation, taking into account the influence of process parameters and wearing of the tools, on quality of received products. Strip compliance for further processing was assessed.

Keywords: *perforation process, perforated steel strips, automotive industry, elements of the exhaust system*

1. Introduction

For the manufacturing of various stamped and bent components in automotive industry, smooth and perforated strips of steel and non-ferrous metals are applied. For instance, perforated strips of alloy steel (12%Cr) and low-alloy steel with siluminium coating are applied as elements of exhaust systems (Figure 1).

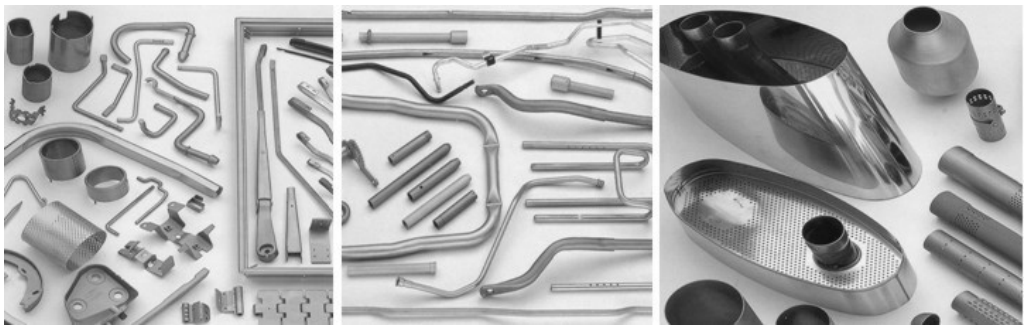

Fig. 1. Examples of smooth and perforated products

Various techniques of cutting, depending on the grade of material, its shape and dimensions, are applied: mechanical (with cutting dies), by laser, gas stream (oxygen, plasma), electric arc and water jet (water leaving the nozzle at high pressure) [1–3].

In automotive industry, in conditions of mass production, perforated strips are produced by classical method of mechanical cutting, providing high efficiency whilst maintaining good quality. The process bases on multi-tact cutting on automatic presses

of special construction. Tools are made of materials providing minimal wearing as well as repeatability of shape and dimensions of products.

The hereby work presents the results of studies on the process of manufacturing and processing of such perforated strips provided for welded tubes, applied mostly as elements of exhaust systems. Tests concerned both the strip and the cutting tools. They were conducted for perforation of steel strip, grade DX52D, of double-side hot dip Al-Si coat, of requirements accordable with norm [4]. The following measuring equipment was applied for the test:

- Hitachi scanning electron microscope (SEM) S3500N,
- NORAN EDS (Energy Dispersive Spectroscopy) analyzer,
- Neophot optic microscope,
- facility for micro-geometry research Form Talysurf.

2. Mechanic strip perforation process

The process was exampled by a production line for welded steel pipes, provided for exhaust systems. The application determines the types of material and dimensions of the strip.

The production line covers the following basic elements: slitting a wide strip into strips of width adjusted to tube diameter, perforating of the strips, forming of open-joint tubes, welding, calibrating, removing of flash, cutting-to-length and packing. Perforation line consists of five sub-systems (Figure 2a–2e): pay-off reel, straighter, fast perforation press, facility with rolls for straitening and running of the strip, strip coiler together with pinch roll.

Fig. 2a. Pay-off reel

Fig. 2b. Straighter

Fig. 2c. Fast perforation press

Fig. 2d. Facility with rolls for straitening and running of the strip

Fig. 2e. Strip coiler together with pinch roll

Fig. 3. Tools for perforation

Due to high number of types of exhaust systems (nearly 2000), the process and the press are controlled by a computer. The average efficiency of the process is ca. 2.5 km/week (ca. 300 m/h). Perforation speed varies between 5–18 m/min. and depends on the kind of perforation (type of pattern). Other parameters of the press: weight 7.9 t, height 3.5 m, maximal number of stamps per minute 230, press force 80 t, three tool stations – two with 3.5 mm diameter of perforators and one with 8 mm of diameter perforators. The tools (stamps and cutting dies) are made of chromium-molybdenum-wolfram-vanadium steel of high wear resistance. Examples of the tools are shown in Figure 3.

3. Results of the studies

3.1. Tools' examinations

New stamps were examined as well as those after a given time of exploitation. Chemical composition and geometry of cutting surface were assessed.

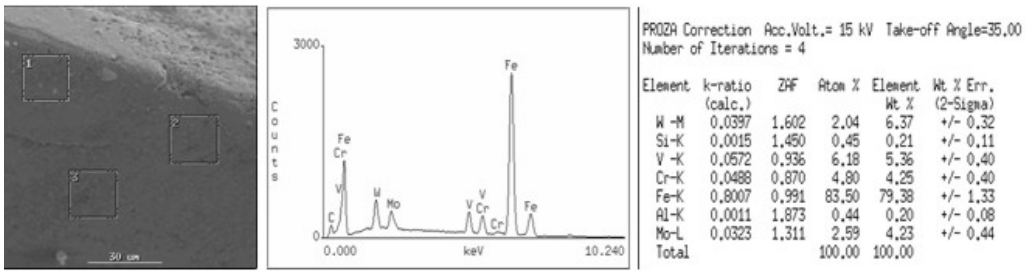

PROZA Correction Acc.Volt.= 15 kV Take-off Angle=35.00
Number of Iterations = 4

Element	k-ratio (calc.)	ZAF	Atom %	Element Wt %	Wt % Err. (2-Sigma)
W -M	0.0397	1.602	2.04	6.37	+/- 0.32
Si-K	0.0015	1.450	0.45	0.21	+/- 0.11
V -K	0.0572	0.936	6.18	5.36	+/- 0.40
Cr-K	0.0488	0.870	4.80	4.25	+/- 0.40
Fe-K	0.8007	0.991	83.50	79.38	+/- 1.33
Al-K	0.0011	1.873	0.44	0.20	+/- 0.08
Mo-L	0.0323	1.311	2.59	4.23	+/- 0.44
Total			100.00	100.00	

Fig. 4. Microphotography of a new stamp on the shearing edge and chemical composition EDS in point 1

Figure 4 presents a photo of a part of a new stamp on its shearing edge with indicated measuring points as well as analysis of chemical composition in point 1 (results in other points are similar). As shown on photos from Figure 5, front and side surfaces of the new stamp are smooth, free of scars, declines or scales, while the shearing edges, except few lesser declines, are sharp.

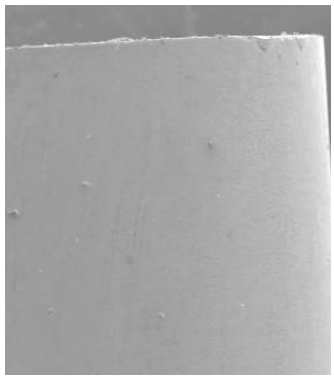

Fig. 5. Part of front and side surface of a new stamp (enlarged 35×)

Results of observation of the stamps after utilization (few dozens of thousands of cuttings) are presented on Figure 6. The shearing edge is rounded, of radius varying from few dozens to few hundred micrometers, depending on number of cuttings, with characteristic, lengthwise scars, while the side surface is characterized by visible declines and decreases of material, as well as lengthwise scars. Stamps are subjected to regeneration by grinding of the front and the side surface.

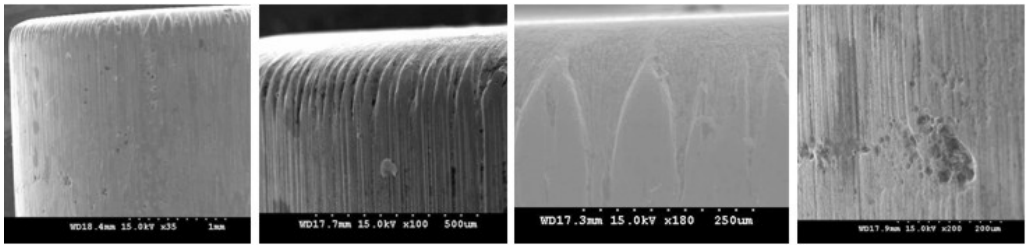

Fig. 6. Fragments of front and side surface of utilized stamps

Microgeometry of the stamps was also examined. The average value of lengthwise microgeometry R_a measured on the side surface is ca. 3.5 times bigger for utilized stamps (R_a = 0.6 μm) in relation to new ones (R_a = 0.16 μm) and regenerated ones (R_a = 0.18 μm). Detailed analysis of tools' wearing in various conditions was presented in the paper [5].

3.2. Strips quality research after perforation

Tests were conducted on steel strips with Al-Si coating. Quality of the achieved products was assessed by measuring the geometry of the holes and the condition and chemical composition of the surface. Results of testing were presented in Figures 7 and 8.

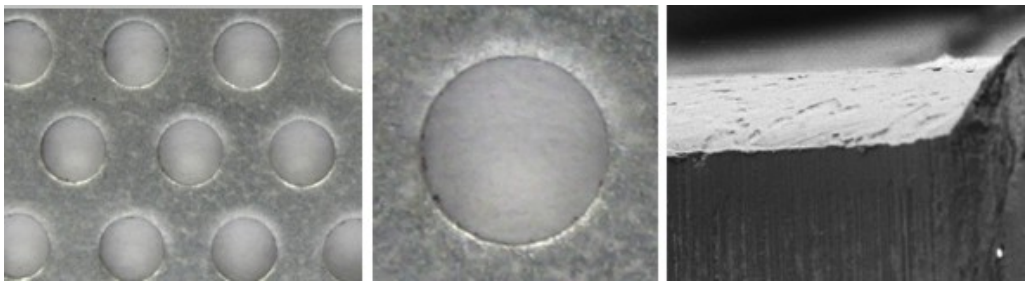

Fig. 7. Surface of the strip with visible bending area

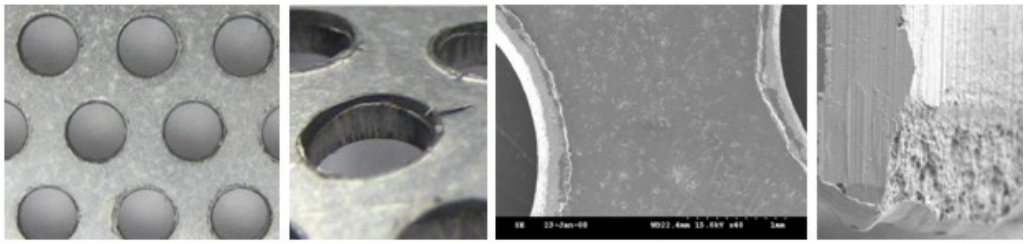

Fig. 8. Surface of the strip with a rolled-up spike

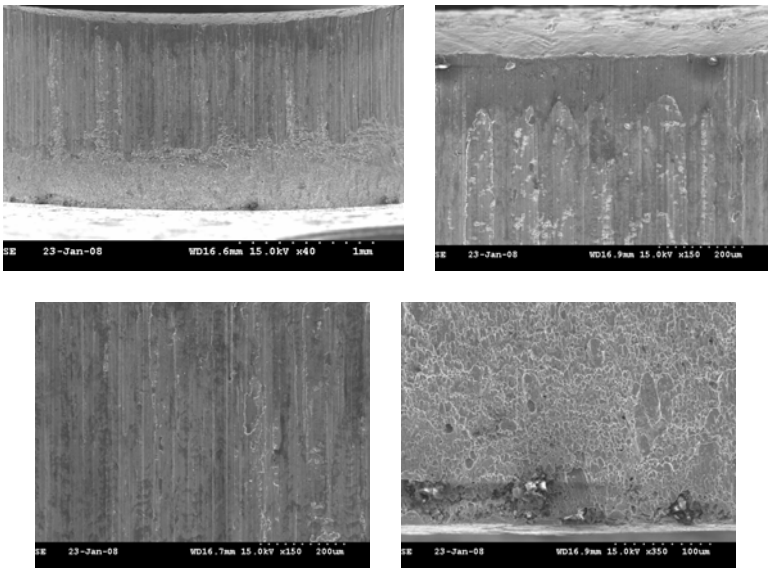

Fig. 9. Hole's section after perforation

On the surface of the hole one can distinguish following areas characteristic for cutting (Figure 9):

- rounding of the upper surface of the strip in the vicinity of the cutting point,
- glancing and smooth rolled surface with scars parallel to the axis of the hole,
- cracking surface (matt and grind), inclined towards the hole,
- a burr – a sharp jag, running along the edge of the hole.

The presence of a burr indicates a blunt shearing surface, it can also appear as a result of too big gap between the stamp and the die (for instance, due to wearing of their side working surfaces).

Results of chemical composition test of material on the surface of the hole, presented in Figure 10, prove catching of Al-Si coat while shearing. This coat is present on the bending area, and on a part of plastic flow area.

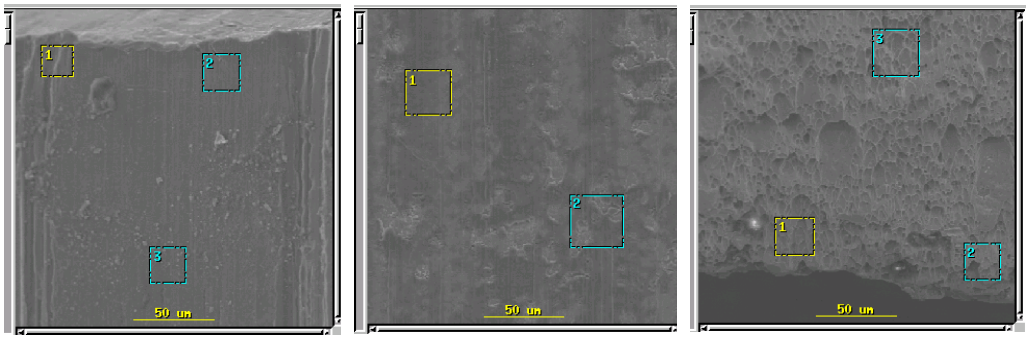

	P1	P2	P3
Fe	13.3	13.1	15.2
Al	83.3	82.5	79.6
Si	3.2	4.4	5.2

a.) upper part of the hole

	P1	P2
Fe	39.2	39.7
Al	54.9	55.1
Si	5.9	5.2

b.) middle part of the hole

	P1	P2	P3
Fe	86.9	88.7	91.3
Al	11.7	9.9	7.7
Si	1.4	1.4	1

c.) lower part of the hole

Fig. 10. Observation of the surface and analysis of hole's chemical composition

3.3. Analysis of perforated strips' susceptibility for processing

The complex results of broad researches on perforated strips deformability can be found in the paper [6–8] and in many other works of the same author. In this case, the only aim was to present the performance of a perforated strip when forming at different loading. For that reason, Erichsen's test as well as cup-forming test was carried out.

Strip bulging in Erichsen's test was executed with application of a spherical stamp of 20 mm diameter. Tests were carried out in two variants – the stamp was pressed into the strip from the side of rounded edges of perforation holes and from the side with burrs. Results of the researches are presented in Figures 11 and 12. Erichsen's index IE made, respectively, 8.4 mm and 7.9 mm, indicating a limited susceptibility for plastic forming of the tested strip subject to flat stretching, independently from localization of the burrs around the perforation.

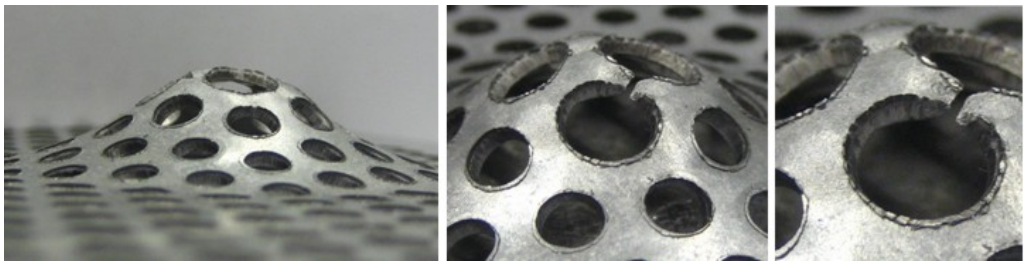

Fig. 11. Observation of the strip after Erichsen's test – stamp pressed from the smooth side of the strip

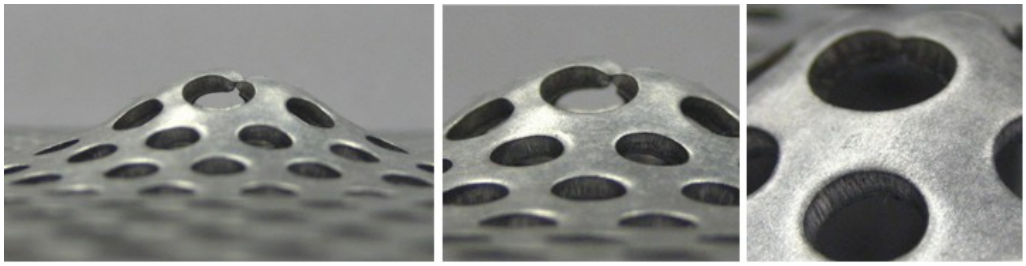

Fig. 12. Observation of the strip after Erichsen's test – stamp pressed from the side with burrs

The cup-forming test was conducted on 60 mm diameter blanks, using a 30 mm diameter stamp and a 34.5 mm diameter die. Drawing coefficient made ca. 0.538. Also in this case, drawing was conducted in two, previously described variants. Results of the tests are presented in Figures 13 and 14.

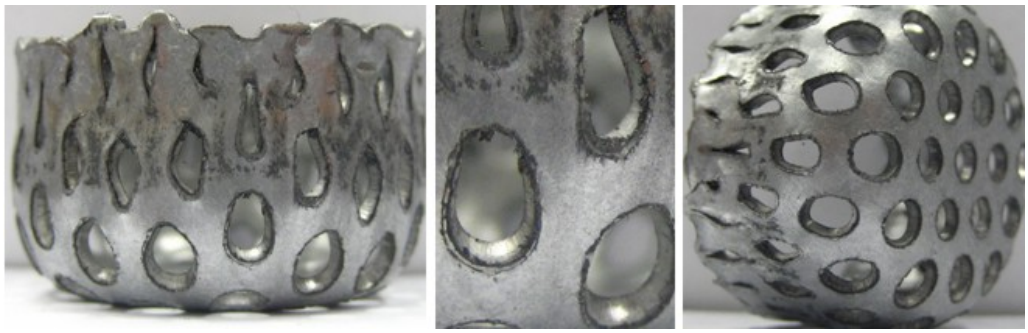

Fig. 13. Observation of strip after cup-forming test – stamp pressed from the side with rounded edges of the holes

Here, it is worth to notice that cracks of material have not been noticed in any case, what – concerning the rate of deformation – proves good susceptibility of perforated strip for drawing.

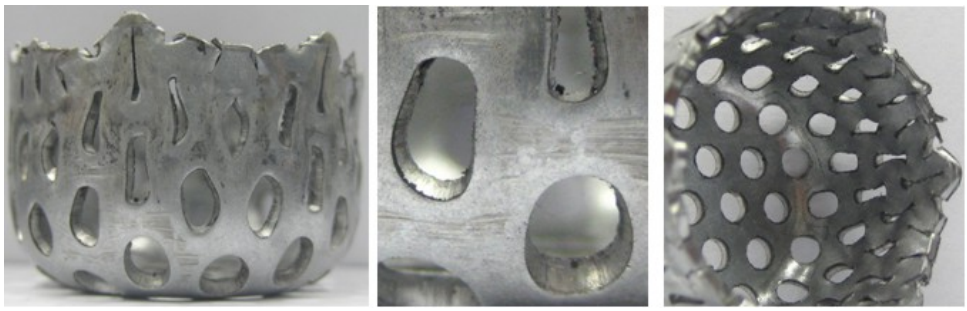

Fig. 14. Observation of strip after cup-forming test – stamp pressed from the side with burrs

4. Summary

The exemplary results presented in the hereby work, concerning perforation process, were achieved during execution of a project, covering developing and implementation of technology of producing tubes for the needs of automotive industry. The object of research and implementation were processing high-alloy, corrosion-resistant strips of ferritic steel and steel with Al-Si coatings. In relation to perforation process, particular attention was put on problems of tools' durability as well as condition of the surface after cutting holes. Exemplary products are presented in Figure 15.

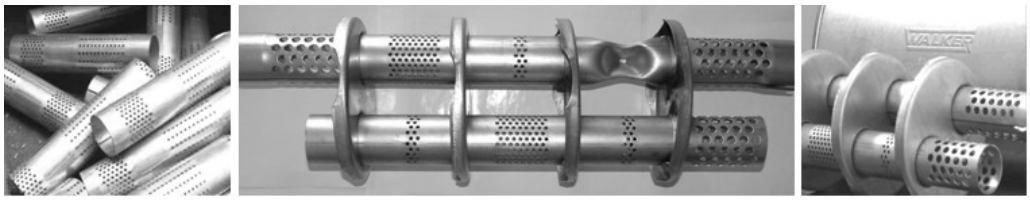

Fig. 15. Examples of perforated tubes and their application as elements of exhaust systems

References

[1] Marciniak Z.: *Construction of press tools*, Ośrodek Techniczny A. Marciniak Sp. z o.o., Warszawa, 2002.
[2] Muzykiewicz W., Łach A.: *Analysis of the possibility to make dense perforations in sheet metal using unconventional high-energy techniques*, Obróbka Plastyczna Metali, Vol. XVIII, No. 1, 2007, pp. 3–11.
[3] Muzykiewicz W., Łach A.: *Analysis of the influence of the sheet metal perforation technique on the quality and the properties of the product*, Obróbka Plastyczna Metali, Vol. XVIII, No. 3, 2007, pp. 13–21.
[4] PN-EN 10327:2006: *Continuously hot-dip coated strip and sheet of low carbon steels for cold forming – Technical delivery conditions.*

[5] Żaba K., Nowak S., Kąc S., Starzykowski S.: *Analysis of tools wearing in of Al-Si coated steel strips perforating process to be used as elements of exhaust systems*, Rudy i Metale Nieżelazne, R–51, No. 2, 2006, pp. 71–78.
[6] Muzykiewicz W., Świątkowski K., Domagała P.: *Formability of Perforated Sheet Metal,* Proc. of the First Australasian Congress on Applied Mechanics ACAM'96, Melbourne, Australia, 1996, Vol. 2, 907–912.
[7] Muzykiewicz W.: *Spatial formation of perforated sheet metal*, In B. Shirvani, M. Geiger, H.J.J. Kals & U.P. Singh (eds), Proc. of the 8th International Conference on Sheet Metal – SheMet 2000, Birmingham, United Kingdom, 2000, pp. 185–194.
[8] Muzykiewicz W.: *Non-uniformity of plastic deformation of perforated sheet metal,* Proc. of the 8th International Conference on Metal Forming – Metal Forming 2000, Edited by M. Pietrzyk, J. Kusiak, J. Majta, P. Hartley, I. Pillinger, Wydawnictwo: BALKEMA, Rotterdam, Brookfield, Kraków, Poland, 2000, 397–404.

Analiza procesu perforacji taśm stalowych stosowanych w przemyśle motoryzacyjnym

W referacie przedstawiono wyniki badań procesu wytwarzania i przetwarzania stalowych taśm perforowanych, stosowanych w przemyśle motoryzacyjnym, głównie na elementy układów wydechowych. Zamieszczono wyniki badań taśmy po perforacji, z uwzględnieniem wpływu parametrów procesu i zużycia narzędzi na jakość otrzymanych wyrobów. Oceniono podatność taśmy do dalszego przetwarzania.

Information for Authors

Send to: *Archives of Civil and Mechanical Engineering*
Polish Academy of Sciences, Wrocław Branch
Podwale 75, 50-449 Wrocław, Poland

Archives of Civil and Mechanical Engineering (ACME) publishes both theoretical and experimental papers which explore or exploit new ideas and techniques in the following areas: structural engineering (structures, machines and mechanical systems), mechanics of materials (elasticity, plasticity, rheology, fatigue, fracture mechanics), materials science (metals, composites, ceramics, plastics, wood, concrete, etc., their structures and properties, methods of evaluation), manufacturing engineering (process design, simulation, diagnostics, maintenance, durability, reliability). In addition to research papers, the Editorial Board welcome: state-of-the-art reviews of specialized topics, letters to the Editor for quick publication, brief work-in-progress reports, brief accounts of completed doctoral thesis (one page is maximum), and bibliographical note on habilitation theses (maximum 250 words). All papers are subject to a referee procedure, except for letters, work-in-progress reports and doctoral and habilitation theses, which are briefly reviewed by the Editorial Board.

The papers submitted have to be unpublished works and should not be considered for publication elsewhere.

The Editorial Board would be grateful for all comments on the idea of the journal.

Detailed information about the Journal on web:
http://www.pan.wroc.pl
www.ib.pwr.wroc.pl/wydzial/czasopismoACME.html
http://www.acme.pwr.wroc.pl
http://www.wmech.pwr.wroc.pl

The papers should be submitted through the webside
http://www.acme.pwr.wroc.pl

Price 15 zł
(0% VAT)

Subscription orders should be addressed to:

Oficyna Wydawnicza Politechniki Wrocławskiej
Wybrzeże Wyspiańskiego 27
50-370 Wrocław